NANOCALORIMETRIC SENSOR FOR ULTRA-LOW-VOLUME BIOLOGICAL MEASUREMENTS AND CALIBRATION BY CHEMICAL METHOD

By

Junkai Xu

Dissertation

Submitted to the Faculty of the

Graduate School of Vanderbilt University

in partial fulfillment of the requirements

for the degree of

DOCTOR OF PHILOSOPHY

in

Physics

December, 2007

Nashville, Tennessee

Approved:

Professor John P. Wikswo

Professor Franz J. Baudenbacher

Professor Joel Tellinghuisen

Professor Hassane Mchaourab

Professor M. Shane Hutson

To my beloved wife, Tingting, infinitely supportive

and

To my great parents, Wangsong and Lizhen, ultimately guiding

ACKNOWLEDGEMENTS

This work would not have been possible without the financial support of the Vanderbilt Institute of Integrative Biosystems Research and Education (VIIBRE) or the Vanderbilt University Department of Physics and Astronomy. I am especially indebted to Dr. John P. Wikswo, Director of VIIBRE, and Dr. Franz Baudenbacher, Deputy Director of VIIBRE, who have been supportive of my career goals and who worked actively to provide me with the protected academic time to pursue those goals.

I am grateful to all those with whom I have had the pleasure to work during this and related projects. Each of the members of my Dissertation Committee has provided me extensive personal and professional guidance and taught me a great deal about scientific research. I would especially like to thank Mr. Ron Reiserer and Dr. Eduardo Lima, who helped me extensively on the techniques and methods on which this research is based.

Nobody has been more important to me in the pursuit of this project than the members of my family. I would like to thank my parents, whose love and guidance are with me in whatever I pursue. Most importantly, I wish to thank my loving and supportive wife, Tingting Chen, for providing me all the confidence and inspiration.

TABLE OF CONTENTS

LIST OF TABLES

LIST OF FIGURES

CHAPTER I

INTRODUCTION

Microcalorimetry is an established technique in the biological sciences for determining energy generation and consumption.[1-3] Many different designs of calorimeters have been described often with specific purposes and applications in mind.[4] Most such techniques are based on isothermal calorimeters, which usually refer to the devices that are operating under essentially isothermal conditions.[5] The microcalorimetric techniques have been much improved during the past decades and as the microfabrication technology advances, sensor could be made to measure signals down to nanowatt scale[6-8] or even lower.[9] Such detection capability is adequate for measuring chemical reactions or ligand-protein binding reactions down to picomole concentrations. Nevertheless, it is an extremely difficult task to measure thermal signals from small numbers of living cells both because of their low thermal activity level (usually in the order of tens of picowatts)[2] and because of the challenge to maintain the viability of the cells while preserving the sensitivity of the sensor.

Objects of the project

The overall research objective of this project is to develop miniaturized nanocalorimetric sensors, calibration methods, and measurement techniques suitable for high-throughput screening (HTS) for drug discovery, metabolic screening using living cells, multianalyte detection and identification of chemical and biological

warfare (CBW) agents. The small size of the reaction chamber, highly sensitive calorimeter and precise delivery method will allow us to do bioanalysis using nanoliter or even picoliter volumes of reagents or a small number of cells. The small volume of the sample reduces reagent costs, conserves valuable and difficult-to-obtain biomolecules, and provides a measurement bandwidth that cannot be achieved with microcalorimeters with larger thermal mass.

There are five specific goals of this project:

1. To build an integrative setup including a nanocalorimetric sensor with evaporation and temperature control and cell/solution delivery system.
2. To calibrate the sensor using well-known chemical reactions.
3. To establish an appropriate computational model to simulate the corresponding measurements.
4. To measure biological signals from living cells.
5. To incorporate microfluidic design with nanocalorimetric sensors for cell based experiments.

General methods and procedures

In this research, we have used a commercially available infrared (IR) sensor to build our nanocalorimeter to achieve the above goals. An integrated system was built for several purposes: maintain the necessary conditions required for cell viability – proper temperature and physiological environment; deliver cell solutions or other media/toxins into the reaction chamber; prevent evaporation from the sample;and record thermal data utilizing a computer for further analysis. This

commercial sensor, as it has no heater built into it, was calibrated using chemical reactions. The detail of the sensor, including its specifications and noise performance will be introduced in Chapter II, Thermal Sensor Performance (HYPRES, Dexter). The details of the integrative delivery/shielding system will be introduced in Chapter III, Equipment and Methods.

Using the above-mentioned methods, we have achieved measurements with a noise level of 7.6 $nW/Hz^{1/2}$ in power noise and 136 $\mu K/Hz^{1/2}$ in temperature noise. These are on the same level as the published data to date. We have calibrated our sensors using chemical methods which closely resemble the biological experimental environment and pattern of heat production. Biological experiments were performed on cardiomyocytes which are stimulated to contract with potassium chloride (KCl). The heat generated during these contractions was measured utilizing the nanocalorimeter.

Thermodynamics of Calorimeters

Essentially, all physics and chemical processes and reactions are accompanied by the absorption or release of heat, and calorimeters are therefore used in a broad range of applications. However, as calorimetric measurements are nonspecific, this property can make calorimetric results subject to systematic errors from evaporation, condensation, adsorption, corrosion, friction, and various spurious chemical or biological reactions. Another important source of systematic error comes from the calibration itself. As may be expected, the smaller the measured heat or

thermal power, the more systematic errors there will be and the more difficult it will be to control these errors.

According to the first law of thermodynamics, the change in thermodynamic energy for a closed system undergoing a change in volume at pressure p is given by equation (1). We assume only 'p·V' work is involved here, as any other work done within the sample (electrochemical, surface, etc.) will finally turn into heat which is observable to the sensor. Using q to measure the heat passing from the surroundings into the system,[10]

$$\mathrm{d}U = q - \underline{p}\cdot\mathrm{d}V \tag{1}$$

where U is the internal energy of the system. By definition, enthalpy is given by

$$H = U + p\cdot V \tag{2}$$

$$\mathrm{d}H = \mathrm{d}U + p\cdot\mathrm{d}V + V\cdot\mathrm{d}p \tag{3}$$

Then under isobaric conditions,

$$\mathrm{d}H = q \tag{4}$$

Equation (4) shows that under isobaric conditions, the calorimeter will measure the enthalpy change, dH, of the process.

When a calorimeter is calibrated, the calorimetric signal is standardized by release of an accurately known heat, q, or thermal power, P=dq/dt. The result of a calibration experiment is usually expressed in terms of a calibration constant, ε, valid for the instrument under some specified conditions. The physical meaning of the calibration constant depends on the measurement principle employed. The next section will briefly review the main calorimetric principles: the adiabatic, the heat conduction, and the power compensation principle. Most isothermal

microcalorimeters are designed as twin instruments, and it is thus a differential signal that is measured.

Calorimetric Principles

There are three major types of calorimeter:[5] adiabatic calorimeter, heat conduction calorimeter and power compensation calorimeter.

In an ideal adiabatic calorimeter, there is no heat exchange between the calorimeter vessel and the surroundings. This implies that the temperature of the calorimetric vessel, which is the measured quantity, will increase (exothermic reactions) or decrease (endothermic reactions) during the measurement. Calorimeters used to study reactions of short duration are usually of the semi-adiabatic (quasi-adiabatic) type. When such calorimeters are used in accurate work, a correction should be made to compensate the heat exchange between the calorimeter and the surroundings.

The quantity of heat evolved or absorbed in an adiabatic calorimetric experiment is, in the ideal case, equal to the product between the temperature change, ΔT, and the heat capacity of the calorimeter vessel (including its contents), C,

$$q = C\Delta T \tag{5}$$

In practice, there will normally be some heat transfer between the vessel and the surroundings, and a “practical” heat capacity value, the calibration constant, is determined in a calibration experiment,

$$q = \varepsilon_a \Delta T \tag{6}$$

where ε_a is the calibration constant (sometimes referred to as the "energy equivalent"). A change in the heat capacity of the content of the calorimetric vessel (following, for example, injection of a sample) will thus lead to a change in the calibration value. The thermal power is

$$P = \varepsilon_a \mathrm{d}T/\mathrm{d}t \tag{7}$$

In a strict sense, experiments with adiabatic calorimeters cannot be conducted isothermally, but the temperature change in a microcalorimetric experiment is usually small, typically in the miliKelvin (mK, 10^{-3} K) range, and the reaction can practically be considered isothermal. However, a microcalorimeter may be used as a "macrocalorimeter," in which case ΔT may be in the order of 0.5 K or larger and cannot be neglected for accurate measurements.

Most microcalorimeters in current use are primarily of the heat conduction type (which is also the case for our nanocalorimeter). In such instruments, heat is allowed to flow between the reaction vessel and a surrounding body (usually a comparatively large metal block) serving as a heat sink. The temperature of the heat sink is kept essentially constant. For an exothermic reaction, heat will flow from the reaction vessel to the heat sink; for an endothermic reaction, heat will flow in the opposite direction. The heat transfer normally takes place through a thermopile that is located between the vessel and the heat sink. If no significant thermal gradients exist in the vessel, the Tian equation[11-14] will hold:

$$P = \varepsilon_c [\Phi + \tau(\mathrm{d}\Phi/\mathrm{d}t)] \tag{8}$$

where ε_c is the calibration constant, Φ the measured voltage difference across the thermopile, and τ is the time constant. Under steady-state conditions, for example,

during the release of a constant electric power during a calibration experiment, equation (8) reduces to

$$P = \varepsilon_c \Phi \tag{9}$$

The time constant is in the ideal case equal to the quotient between the heat capacity of the system (usually the reaction chamber and its contents) and the heat conductance of the thermopile. The heat capacity of the system is therefore a key parameter for heat conduction calorimeters used in kinetic measurements. Ideally, the calibration constant ε_c is equal to the ratio between the thermal conductance associated with the thermopile and the Seeback coefficient for the thermocouple material and will thus not be influenced by heat capacity changes caused by injections of small samples into the reaction vessel and is the same for calibrations carried out before and after the reaction has taken place. This is a real advantage in that a calibration experiment does not have to be performed for each experiment.

In a power compensation calorimeter, the thermal power from an exothermic process is balanced by a cooling power, typically by using the Peltier effect. For endothermic reactions, compensation is achieved by reversing the Peltier effect current or by release of electrical energy in a calibration heater. Thus, measurements in a power compensation calorimeter are conducted under essentially isothermal conditions.

In a special kind of power compensation microcalorimeter,[15] the temperature is allowed to increase at a constant rate, as in a DSC (differential scanning calorimeter, where the temperature of the sample and calorimeter is scanned over a

range during a measurement) but very slowly. The thermal power from a measured process is, in that case, compensated for by a change of the electrical heating power.

Isothermal Microcalorimeter and Nanocalorimeter

The term “isothermal microcalorimeter” is commonly used for calorimeters designed for use in the microwatt range, under essentially isothermal conditions. The word “isothermal” is in this connection normally not used in a strict sense, but is merely an indication that the temperature of the calorimeter is constant or very nearly so within narrow tolerances.[5]

Isothermal microcalorimetric techniques have been much improved during the past decades, and several types of instruments are commercially available. Application areas include, for example, ligand binding studies, dissolution and sorption measurements, estimation of the stability of chemical substances and technical products, and measurements of metabolic reactions in living cellular systems.[5-8,15,18]

Such calorimeters are usually of the heat conduction type, like the sensor we are using, except our sensor has a lower limit of detection in the nanowatt range. We refer to our sensor as nanocalorimeter because of its nanowatt detection sensitivity and its miniature structure. Isothermal microcalorimeters are used in many types of thermodynamic investigations measuring thermodynamic constants of materials and compounds. The most important property is, in this connection, the enthalpy change, ΔH. When the enthalpy change is determined as a function of temperature the change in heat capacity can be derived, i.e., $\Delta Cp = \mathrm{d}\Delta H/\mathrm{d}T$.

Titration Calorimetry and Calibration Using Chemical Methods

Titration calorimetry, an important technique in isothermal microcalorimetry, can lead to the simultaneous determination of both the molar enthalpy change and the equilibrium constant, and thus also to values for the standard molar Gibbs energy change and the standard molar entropy change.[15-17] Isothermal microcalorimeters are often suitable for the direct determination of thermal power or the rate of heat evolution, including the determination of rate constants and reaction orders for moderately fast to very slow reactions.[18, 19] The biological measurements we are proposing here (living cells under the influence of drugs or other chemicals) fall perfectly into that category of reactions.

Calorimeters are usually calibrated electrically. This is a convenient method which is also very accurate in the sense that electric power or energy can be precisely controlled and measured with better accuracy than the calorimetric signal it will be compared with. But sometimes the comparison between the heat released in the electrical calibration experiment and that evolved in the process studied is not very close. For example, the heat source in the experiment could be within the sample (which is exactly the case for our biological measurements here) while the electrical heater is usually integrated in the sensor together with the thermopile. In such situations, it is then necessary to have other calibration methods which can closely simulate the true conditions of the experiment so that the calibration heat is released in exactly the same pattern or a very similar way as in the experiment. Based on our purpose of using the sensor in biological measurements where a bulk of watery sample is present, it is then preferred that chemical calibration be used

here. The idea is that by injecting chemicals into the bulk sample and measuring the heat production (or consumption) from the chemical reactions, we can calibrate the sensor more accurately than by using a heater buried under the sensor membrane. This is because our biological experiments require the same type of water-based sample and the heat is produced from virtually everywhere in the sample, which is closely imitated by the chemical reactions happening throughout the sample after injection. There are many chemical reactions we could use for the proposed method of calibration. In general, these reactions are simple, single step, and nonhazardous, and the materials are easy to acquire and store, such as the neutralization reaction and dilution of salt. This obviously would avoid any undesirable complications. More details of the chemical calibration will be reviewed in Chapter V, Calibration of the Sensor Using Chemical Methods.

Terminology for Nanocalorimeters

Many terms and parameters must be specified for a nanocalorimeter. First of all, the calorimetric type (usually heat conduction type, isothermal type) should be mentioned. The physical dimension and the general environment of the reaction chamber should be explained. This information includes the material used for the reaction chamber (most importantly the membrane) and the materials used for the thermopile, the general structure of the membrane, thermopile and their link to the heat sink, etc. Some technical specifications are especially important here:

1. Seebeck coefficient. This is the property of the thermopile. Our sensor measures a voltage signal which is proportional (for use within small

temperature range, which is true most of the time since nanocalorimeters are usually isothermal) to the temperature difference (ΔT) between the measuring junction and the reference junction coupled to the heat sink. The Seebeck coefficient is then the constant of the proportionality between that ΔT and the measured voltage. The thermal sensor's output is a voltage which is related to a temperature change through the Seebeck coefficient. All subsequent properties such as the power sensitivity or time constant are dependent on the Seebeck coefficient of the sensor.

2. Limit of detection. In calorimetry, the term limit of detection is sometimes referred to as sensitivity and it is basically the detection limit of a specific quantity being measured, whether it is temperature or power. This is closely related to the sensor's (and also the amplifier's) noise level. Because of the existence of noise, the measured signal will be fluctuating around the "true" value. The fluctuation becomes the limitation of the detection because you cannot differentiate a power level or a temperature level which corresponds to a voltage level smaller than that fluctuation. That lowest level of power or temperature we can detect is thus our power or temperature sensitivity. More details on the noise level and temperature/power sensitivity will be discussed in the Chapter II, Thermal Sensor Performance (HYPRES, Dexter).
3. Baseline. The baseline of the calorimeter is defined as the value recorded for the calorimetric signal when no thermal power is evolved in the reaction chamber, or in other words, the signal when the sensor is

completely “blank”. This value could change based on the specific status of the reaction chamber. The general issues that will influence that value include: temperature of the surroundings (background temperature), sensor’s intrinsic properties, the sample on the sensor membrane, and the pressure (which affects the shape of the membrane) on the membrane, etc. Since the baseline voltage is subject to so many influences, its value is very likely to change during one experiment, such as after you have injected the sample or added some solution to the sample. However, a shift in the baseline could also be understood as an increase or decrease in power. Because of this, we must carefully monitor the baseline’s change during the experiment and design specific control experiments to avoid misunderstanding the true reason causing a baseline shift. Aside from the quick shift caused by the action or power increase, the baseline could also drift over a long time, sometimes due to slow process such as evaporation or condensation over a long time. Such a drift should be avoided, or fixed on the data by doing a linear fit to the baseline to determine where the baseline should be at a certain time.

Calorimeters Microfabricated by Other Groups

Recently, three research groups have developed micromachined Si-chip-based microscale calorimetric devices. Torra et al. reported micromachined Si-chip-based calorimetric microphysiometer based on 666 Al/p+-polysilicon thermocouples with power and temperature sensitivity of 23 V/W and 130 mV/K. for 50 μl of water.[20]

The relatively large chamber volume of 10 – 600 µL, which can house up to 10^6 eukaryotic cells, requires a very long thermal equilibration time of 45 min and long response time (> 70 s) after hormone addition. They estimated the metabolic heat production of 330 pW/cell for cultured kidney cells, which increases by 106 pW/cell after oxytocin hormone addition.

Baier et al. constructed a 30 µm thick Si-membrane thermopile chip with a heat power sensitivity of 2.4 V/W[21-23]. They used a different design of liquid delivery interface and achieved 2 µg detection of urease enzyme by hydrolysis of 7 mmol/L urea. Their reaction chamber is about 90 µl. Because of the insufficient sealing between the syringe and the cover, evaporation occurs during the experiment at all times. They used a circular piece of moisturized filter paper to reduce the time to reach equilibrium from 30 minutes to 15 minutes. However, since evaporation is not completely stopped leads to the result that part of the offset is due to the evaporation, undermineing the reproducibility of their experiments. They have made more sensitive flow-through calorimeters recently by combining microfluidics with a differential thermopile chip calorimetry technique. Their first version of this calorimeter[24] consists of a reaction chamber of 20 µL volume where an inlet and an outlet are installed. A double layer thermostat provided them the ambient temperature stability up to 4.3 µK. However, because the chip is not directly coupled to the temperature control element, the temperature fluctuation in there is actually more than 1 mK. This calorimeter has a detection limit to approximately 50nW under optimized conditions. However, since its differential setup did not fully compensate for the temperature fluctuation caused by environmental noise. So they developed a

second version of differential flow-through calorimeter.[25,26] (see **Figure 1**) This calorimeter is equipped with 4 sets of differential thermopiles, each of which consists

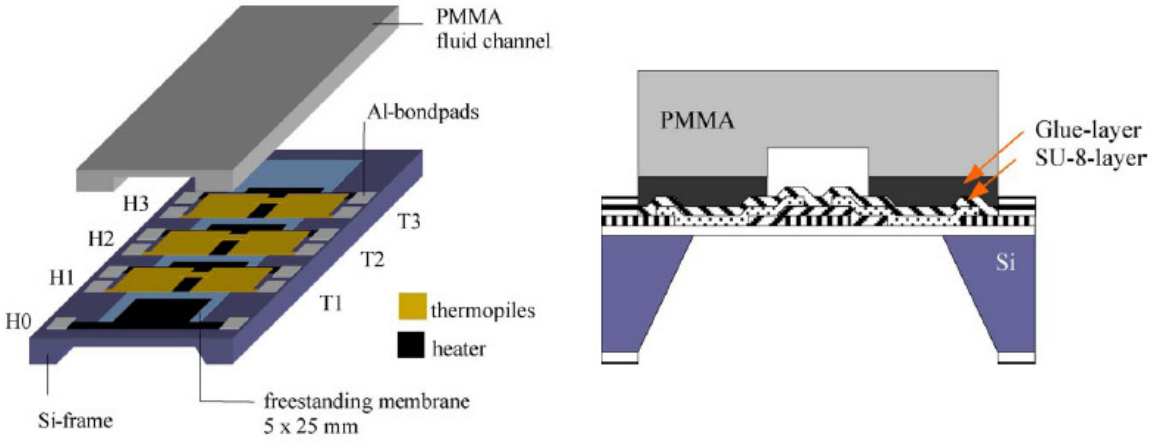

Figure 1. Flow-through device schematics by Baier et al[25]. Flow channel is 20 mm x 1 mm x 0.4—1.2 mm, typical volume with 0.5 mm height is 10 µL. Assays done with E. coli. achieved a measurement accurate up to µW is achieved. (From Baier, et al.)

of 118 Bi/Sb thin film thermocouples. With built in heaters, the limit of detection of this type of sensor was determined to be 100 nW and 4 uJ. This type of calorimeter was used to monitor aerobic growth of suspended and immobilized *Escherichia coli* DH5α DSM 6897 and anaerobic growth of suspended *Halomonas Halodenitrificans* CCM 286^{T}. Qualitative correct results were obtained for microwatt range signals. The flow-through structure worked very well for suspension and biofilm deposition into the reaction chamber.

Johannessen et al. presented a more delicate experimental design and obtained results with enzyme catalyzed reactions and cell metabolisms. They designed and produced a ten-junction gold and nickel thermopile nanocalorimeteric

sensor with a temperature resolution of 125 μK and 12 ms response time.[27-30] On top of that reaction chamber, they used paraffin oil as a seal to prevent evaporation. They measured the thermogenic response of 16 nW for ten brown adipocytes following noradrenaline stimulation. The heat output of five cardiomyocytes challenged with a mitochondrial decoupler was found to be on the order of 1.7 nW per cell. Catalase activity of a single mouse hepatocyte was estimated by hydrolysis of 10 pmol H_2O_2 and corresponded to 1350 nJ production.

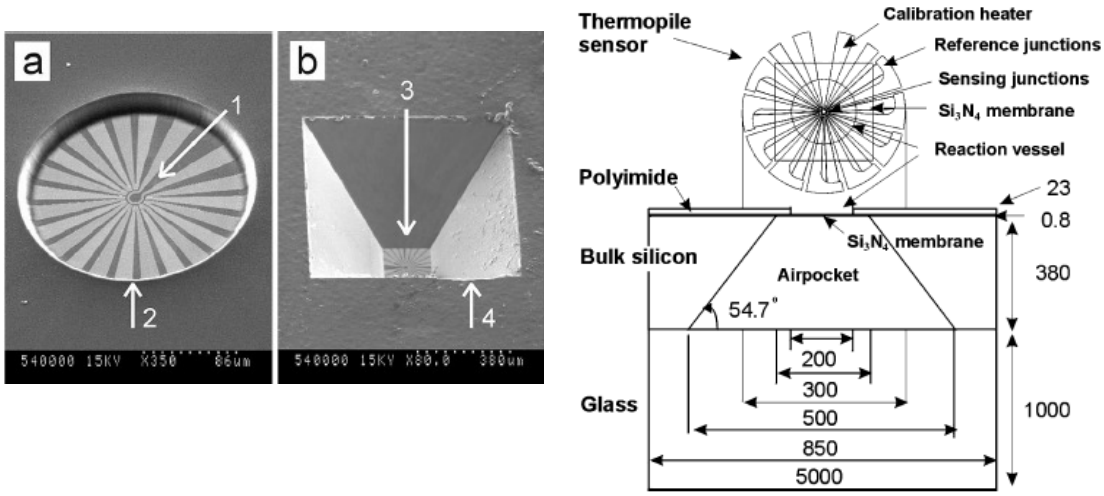

Figure 2. Chip design and reaction chamber schematics by Johannessen et al[27]. On the left: a) top view of the reaction chamber, b) back of the sensor. On the right: the mechanical dimensions of the reaction chamber and the thermopile. (From Johannessen et al.)

The major advantage of their calorimeter is the extremely small built-in reaction chamber (see **Figure 2**), which easily accommodates the liquid in experiment and has a polymer thermal insulator to ensure the thermal insulation of the reaction chamber from the environment so that performance of the calorimeter will not be greatly affected by the paraffin oil added for evaporation prevention.

Although it is not equipped with microfluidics, it actually has a better temperature/power resolution than the other sensors currently being used for biochemical processes. The major limitation to their sensor, however, is the oil cover which limits power sensitivity. This is because their oil cover, while serving as a thermal shield and evaporation stopper, also provides a large addition to the thermal conductance of the sensor between sensing junctions and heat sink. In fact, it is the dominant heat conductor between the sensing junctions and the heat sink. We will give details of how our sensor excels in this specific aspect in Chapter II, Thermal Sensor Performance (HYPRES, Dexter).

Calorimetric Measurements on Cell Metabolism

Energy requirements of human and animal cells are met by oxidation of macronutrients in association with distinct biochemical reactions.[2] In each of these reactions about one third of the chemically bound energy is conserved in energy-rich phosphate bonds (mainly ATP), the remainder being converted into heat. All energy-dependent processes utilized about one third of the energy released by ATP hydrolysis, the remainder again being converted into heat. Ultimately, the energy released by nutrient oxidation is completely transformed into heat. This interrelation between metabolic rate, substrate utilization and heat production (thermogenesis) facilitates the assessment of total energy turnover in the cell under normal and pathological conditions and how it is influenced by various hormones and drugs, by direct physical determination of cellular heat energy production per unit of time.

For heat production of a specific metabolic process, investigations were done previously by analyzing the individual reaction steps through equilibrium or network thermodynamics. This is unnecessary, however, as the law of constant heat summation formulated by Hess states that the decrease in enthalpy of a reaction sequence (the heat evolved at a constant pressure) depends only on the initial reactants and final products of the sequence and is independent of the intervening reaction steps. Or in other words, any process that does not produce intermediates, without performing useful work or concentrating ions can be said to have 100% thermogenesis.

The typical processes in cell activities involving thermogenesis include glycolysis, the TCA cycle, the nerve action potential and muscle contraction, etc. Such activities are usually subject to the influence of certain toxins which may inhibit or promote the process. **Figure 3** shows a few metabolic pathways and sites of action for known toxins.

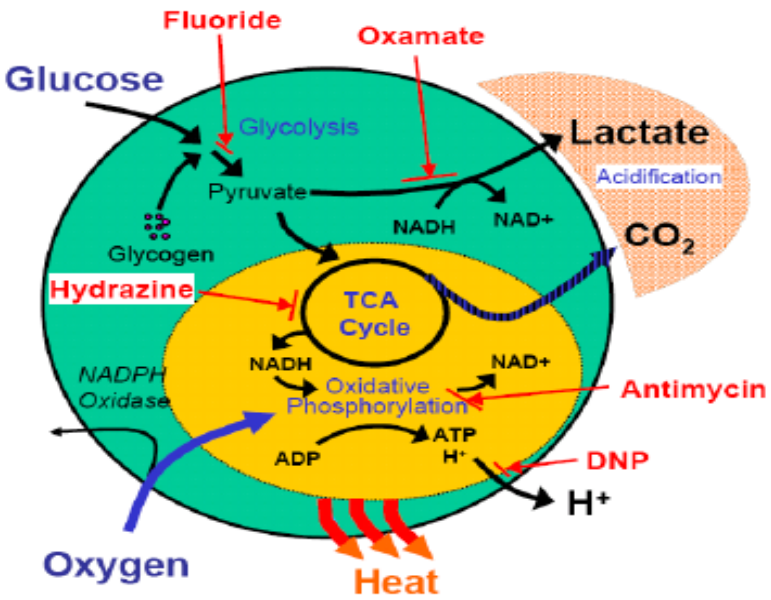

Figure 3. A simplified representation of metabolic pathways and sites of action for known toxins. Simultaneous measurements of the dynamics of glucose, lactate, CO_2, O_2 and pH can discern which pathway is affected by a drug. Heat generations would be an additional metabolic parameter that would aid in determination of the dynamic metabolic fluxes in such a model. (Courtesy of VIIBRE)

The heat power per cell ranges from 2 pW to 1.7 nW as measured for different cells under different conditions and under influence of various drugs and hormones[2,31-44]. See **Table 1** for a specific list of cell heat production under certain experimental conditions. From the table, we can see there is a lot of variation in cellular heat production. This is normal as different cells have different sizes and functions. Those that are highly metabolically active include cardiomyocytes which will contract upon stimulation, the brown adipocytes which are designed to generate body heat, and hepatocytes which have very active physiological functions. Such cells with high metabolic rate and heat production are therefore ideal for our cell metabolic measurements. As we will introduce in Chapter VI, tens of cardiomyocytes

is enough to generate tens of micro joules (μJ) during the experiment period and thus give us a highly measurable signal. Another advantage of the cardiomyocytes is that they do not require culture and will be relatively active metabolically once placed into the reaction chamber.

Table 1. Metabolic heat production per cell measured by microcalorimetry, sorted from low to high

Type of cells	Cellular heat production level
T-Lymphoma cells[32]	6.1pW
Human lung fibroblast[41]	20-48pW
Human skin fibroblast[40]	51pW
Rat hepatocytes[43]	0.327nW
Brown adipocytes[45]	1.63nW
Cardiomyocytes[27]	1.7nW

In microcalorimetric measurements on living cellular materials it is normally the rate of heat production as a function of time which is measured. This could be done in flow-through systems or closed systems where the cells settle down to the surface. Microorganisms or animal cells could be used. For microbial systems – bacteria, yeast and mycoplasma – the measurements are usually conducted in flow instruments. Flow calorimetric experiments with microorganisms are in most cases easy to perform, as the heat production rate is high; and except for yeasts, there is usually no problem with the flow of cell suspension. Animal cells, on the other hand are more fragile and stickier; and calorimetric measurements on animal cells are usually done with tissue pieces, with cells in suspension or attached to a surface. A

static reaction vessel equipped with an injection device for reagents (drugs) is preferred. Our evaporation-proof liquid delivery system together with the reaction chamber it forms on the sensor is just a miniaturized setup for such a static reaction vessel. In fact, most reports on animal cells and tissue have so far been conducted by use of static vessels where the cellular materials usually will sediment during the experiment. The physiological conditions are then poorly defined. Aerobic and anaerobic conditions are different in heat production in the same amount of consumption of nutrients.[34] Glucose, for example, has a 470 kJ/mol heat production under aerobic conditions while it has only 80 kJ/mol under anaerobic conditions. Thus, caution must be taken to ensure the cell viability and to avoid oxygen starvation in the calorimetric vessel[45] if the experiment is intended to take place under aerobic conditions. The other factors that affect the cellular heat production include pH variation, cell concentration/cell confluency (for cultured cells) and influence of drugs/toxins. Cell concentration or cell confluency may not be purely positively related to the total heat production as cells could starve of nutrients or intoxicated by their own wastes when they are highly concentrated in a small volume. This is especially true for non-flow-through devices (such as our sensor), as there will be no supply and recycling once the cells are placed in the reaction chamber.

Experiments are usually not conducted under sterile conditions (except for long-term measurements with cultured tissue cells) and media are therefore often supplied with antibiotics in order to suppress microbial growth during the measurements. Calorimetric control experiments with some antibiotics show marginal or no effect on the metabolism of a few cell types.[46]

The true difficulty of calorimetric measurements on cell metabolism, however, is to fabricate a sensor (and also the peripheral system) that is capable of accommodating the cells in the reaction chamber and at the same time still possesses a high sensitivity for both power and temperature measurement. This is because the cells require an aqueous environment to survive while any such environment basically reduces the sensitivity of the sensor by both contributing a large thermal mass to the system and greatly increasing the sensor's thermal conductance from the thermopile to the heat sink. This will greatly affect the time constant of the sensor and most importantly, decrease the power sensitivity of the sensor. We will discuss in more detail how we solved this problem in Chapter II, Thermal Sensor Performance (HYPRES, Dexter), and Chapter VI, Biological Measurements Using Cardiac Cells.

CHAPTER II

THERMAL SENSOR PERFORMANCE (HYPRES, DEXTER)

The thermal sensor and the peripheral apparatus are the key to the success of our goal – to measure biological thermal signal at high precision. At the beginning stage of the project, HYPRES Inc. (Elmsford, NY) was the major provider of the calorimeter chips, called PicoCalorimeters. Their chips provide an excellent power resolution of 2.2 nW and temperature resolution of 21 μK. Their chips were microfabricated in batch and Eric Chancellor experimented with them.[9] However, due to the high fabrication cost and the lack of microfluidic channels on their chips to accommodate the sample, we later switched to the S25 sensors from Dexter Research Center Inc. (Dexter, MI). The S25 sensor is a type of infrared (IR) sensor based on silicon membrane and thermopiles. It has great power sensitivity but less temperature sensitivity than the HYPRES chips. The major advantages of the S25 sensor are they are relatively inexpensive, readily available, and possess a circular well of 2 mm diameter and 0.5 mm in depth. This well is then modified to form our reaction chamber. In the following paragraphs, we will introduce the general specifications of these two types of sensors and describe how I applied them to my experiments.

Basics of Thermocouple and Thermopile

When two different metals form a closed circuit, there exists a voltage difference between the two junctions if they are at different temperatures. This is the Seebeck effect first discovered by Thomas Johann Seebeck in 1821. Such a two metal device is a thermocouple. Thermocouples connected in series form thermopiles, which are commonly used in calorimeters with high precision (see **Figure 4**). By measuring the voltage difference between junctions, one can determine the temperature difference.

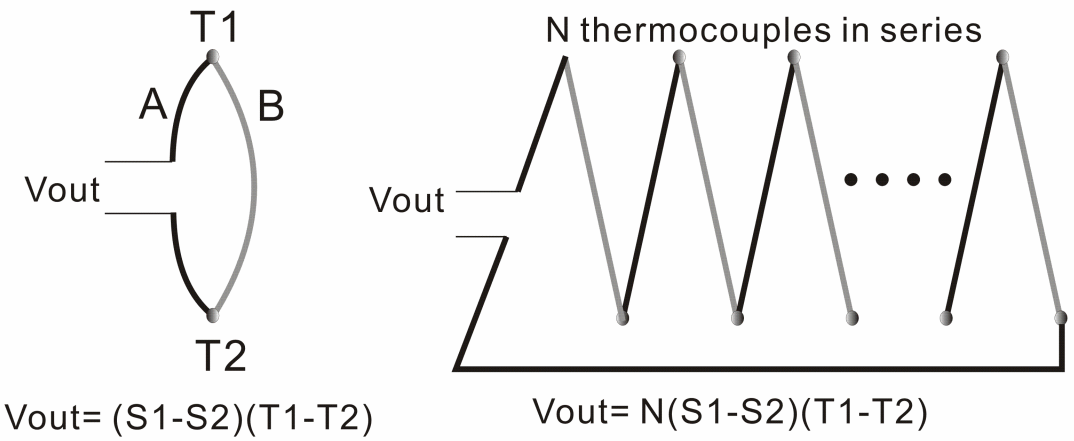

Figure 4. Thermocouple and Thermopile. On the left is a thermocouple with S2 and S1 being the Seebeck coefficient of the two metals. T2 and T1 are temperatures at two junctions. In the thermopile, there are N hot and N cold junctions.

The Seebeck effect can be explained by considering the electro-chemical potentials of the metals. The energy distribution of the electrons in the metals is governed by the Fermi-Dirac distribution function

$$f_0(E) = \frac{1}{1 + \exp(\frac{E - \mu}{kT})} \tag{10}$$

where μ is the chemical potential and is equal to the Fermi energy E_F at absolute zero. Thus μ could be expressed in terms of E_F and T as such:

$$\mu = E_F - \frac{\pi^2 k^2 T^2}{12 E_F} \tag{11}$$

At temperature above zero, μ is slightly lower than E_F but at room temperature they are practically the same. When metal conductor is involved in the circuit, the chemical potential μ and an electrostatic potential energy -|*e*|V may be combined to form the electrochemical potential $\bar{\mu}$ given by

$$\bar{\mu} = \mu - |e|V \tag{12}$$

Thus electrons move in a conductor when a gradient in the electro-chemical potential exists.

We now define thermopower S as such, when there is no current,

$$|e|S = \nabla\bar{\mu} / \nabla T \tag{13}$$

which for a homogeneous conductor could be written as

$$|e|S = d\bar{\mu} / dT \tag{14}$$

and thus

$$\bar{\mu} = |e| \int S dT \tag{15}$$

This last equation shows that the change in $\bar{\mu}$ between two points could be obtained from integration of *S*. For a thermocouple as described in Figure 1, as *S* is a function of temperature *T* and has different values for different metals, we could perform an

integration for conductor 1 and conductor 2 from junction to junction to find the relation between total voltage difference and the thermal power S of each metal. Such a calculation will turn out to show that

$$dV_{12} / dT = S_{12} = S_2 - S_1 \tag{16}$$

where V_{12} is the voltage difference or Seebeck electromotive force (e.m.f.) and S_1, S_2 are corresponding thermopower for each metal. Within a small temperature range where we could treat the *S*'s as nearly constants, equation 14 will be in the form we are familiar with,

$$\Delta V = S_{12}\Delta T \tag{17}$$

It turned out that the absolute thermal power we defined above is the Seebeck coefficient of the individual metal, and S_{12} is merely the difference of the Seebeck coefficient of the two metals, also the Seebeck coefficient of this thermocouple.

HYPRES PicoCalorimeter

The PicoCalorimeter concept developed by HYPRES is illustrated in **Figure 5**, along with a photograph of a prototype device designed and fabricated at HYPRES for a separate application.

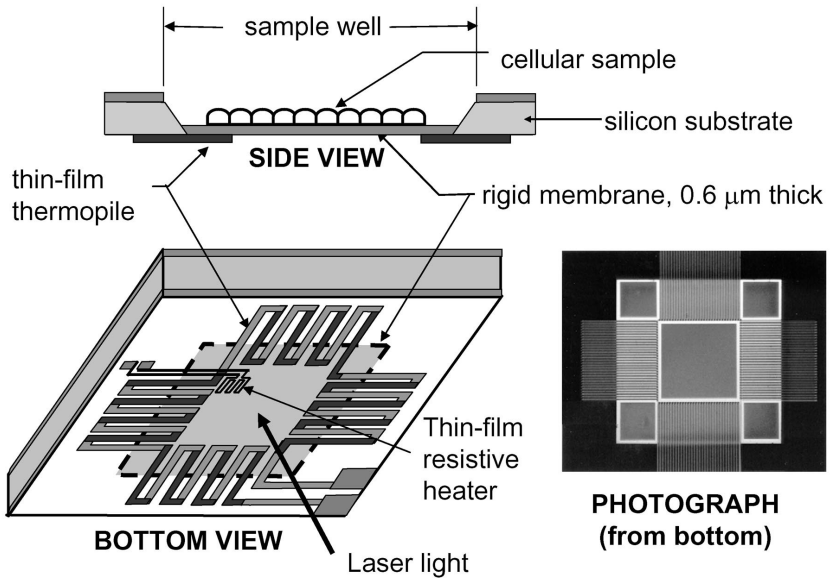

Figure 5. A prototype HYPRES micromachined PicoCalorimeter. The drawings are simplified and not to scale; the actual device in the photograph has a thermopile with 124 thermocouples in series. The membrane is 1 mm X 1 mm in area, and 0.6 um thick. Calibration is accomplished with either a laser or a thin-film resistive heater on the rigid membrane. (Courtesy of HYPRES)

Design of PicoCalorimeter

The PicoCalorimeter structure is based on an opening in a silicon substrate that is spanned by a rigid membrane. The membrane forms the bottom of a "well" with sloping sides that can confine liquid or solid samples. A thin-film thermopile measures the temperature rise of the membrane relative to the reference junctions on the side. This is the same idea as any other isothermal heat conduction calorimeter. However, since the membrane is so thin here, the heat conductance of the sensor from the sensing junctions to the reference junctions is greatly reduced, which gives the PicoCalorimeter good power sensitivity.

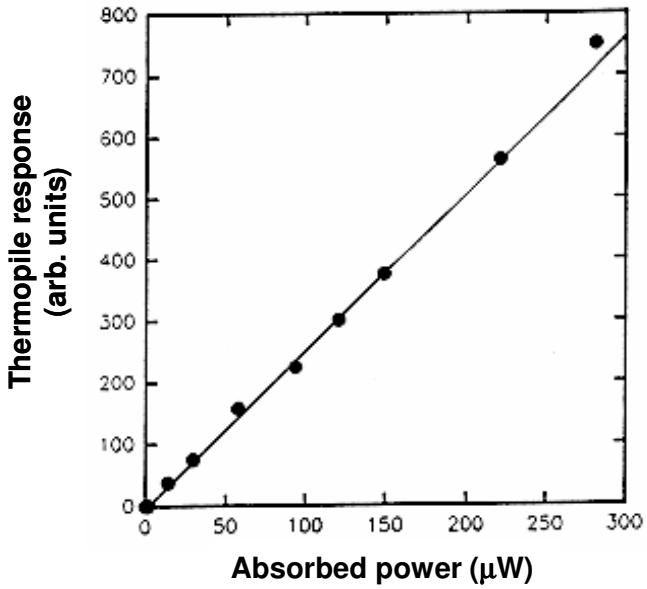

Figure 6. The linearity of a prototype HYPRES PicoCalorimeter (Courtesy of HYPRES)

The material of the rigid membrane, amorphous silicon nitride, is harder than stainless steel and silicon carbide.[47] Even at a thickness of 0.6 μm, the freestanding membrane can sustain the pressure from small liquid drops without damage. The linearity of the PicoCalorimeter was measured over two orders of magnitude in heat power. The results demonstrate high linearity (see **Figure 6**). Another measurement indicates that the change in the PicoCalorimeter's gain[48] with temperature is 0.14%/^{o}C.

Noise Performance, Sensitivity and Time Response

The noise level is very important for any micromachined calorimeter. The PicoCalorimeter has an excellent performance in noise aspect. The measured noise voltage density is only 14 nV/Hz$^{1/2}$ and there is no noticeable 1/f noise present (see

Figure 7). Being free of 1/*f* noise is a great advantage of thermopile thermometers because they are not voltage biased.

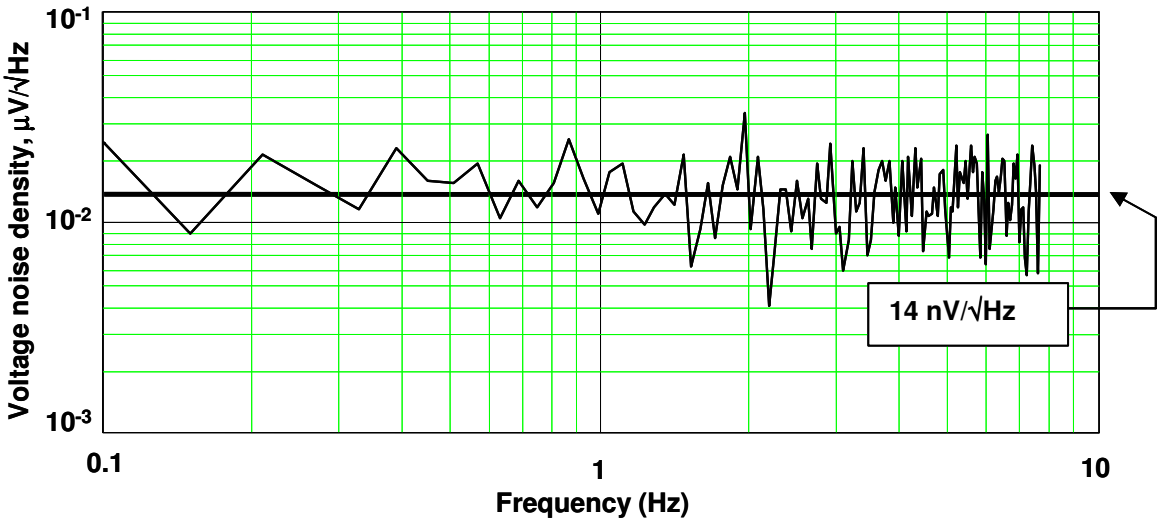

Figure 7. A measurement of the noise in a HYPRES thermopile thermometer, showing no detectable 1/*f* component down to the lowest frequency of the measurement, 0.1 Hz. The device and measurement were made in Ref. 48.

Based on the PicoCalorimeter's noise level of 14 nV/Hz$^{1/2}$ and its Seebeck coefficient of 82 μV/K per junction, I calculated the temperature sensitivity for an 8-junction PicoCalorimeter (which is one of those we used at the beginning of this project, see **Figure 8b**). The temperature sensitivity is estimated to be 21 μK/Hz$^{1/2}$. For the 7-junction type, which has the built-in heater (see **Figure 8a**), the temperature sensitivity is slightly higher at 24 μK/Hz$^{1/2}$.

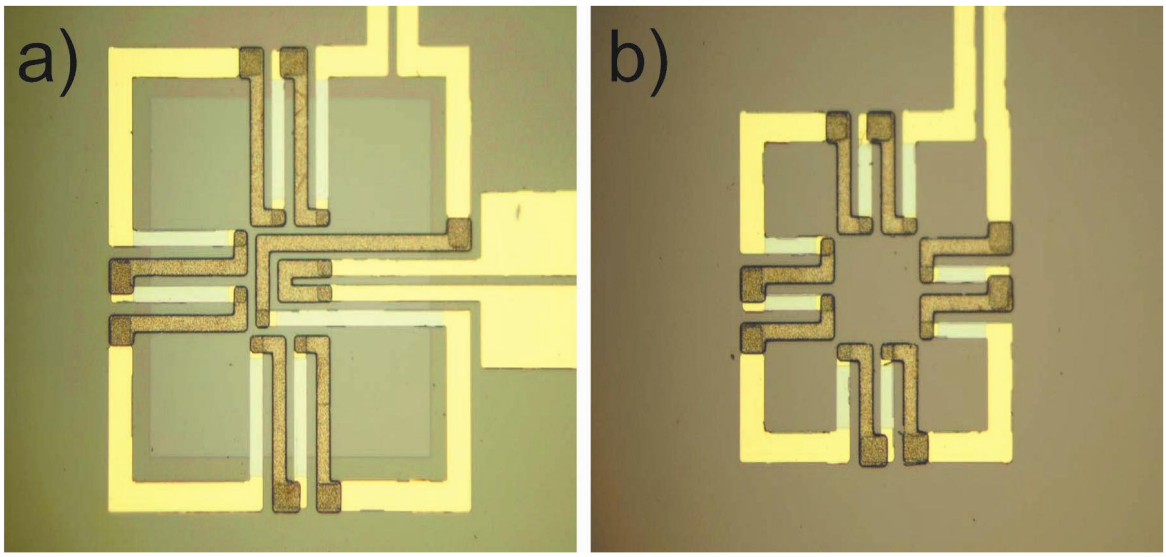

Figure 8. Photographs of PicoCalorimeters fabricated at HYPRES using Ti/Bi/Au materials. The thermopile line widths (central structures) are all 10 μm. a) A device with seven thermocouples in series, and a resistive heater built onto it. b) A PicoCalorimeter with eight thermocouples in series. (Courtesy of HYPRES)

The power sensitivity, on the other hand, will depend on the real experimental conditions, including how the sample is placed on the calorimeter. The lower the thermal conductance from the junctions to the heat sink, the higher the power sensitivity. The NEP (noise equivalent power) of 176 $pW/Hz^{1/2}$ as specified by HYPRES was obtained using a laser, which does not reflect the true performance of the PicoCalorimeter if there are liquid samples placed on it. Since the PicoCalorimeter is never calibrated under experimental conditions, there are no accurate power sensitivity data available. The estimated power sensitivity however, could be acquired from the droplet evaporation experiment (see next subsection) and it is estimated to be 2.2 $nW/Hz^{1/2}$.

The time response of the sensor is 50 ms as mentioned in HYPRES's measurements on prototype PicoCalorimeter. The measurements conducted at

VIIBRE, however, gave a time response of 80 ms (see **Figure 9**). Again, neither of these is a true representation of the actual time response when the PicoCalorimeter contains samples, because the time response of the device is greatly reduced due to the extra heat capacity of the liquid.

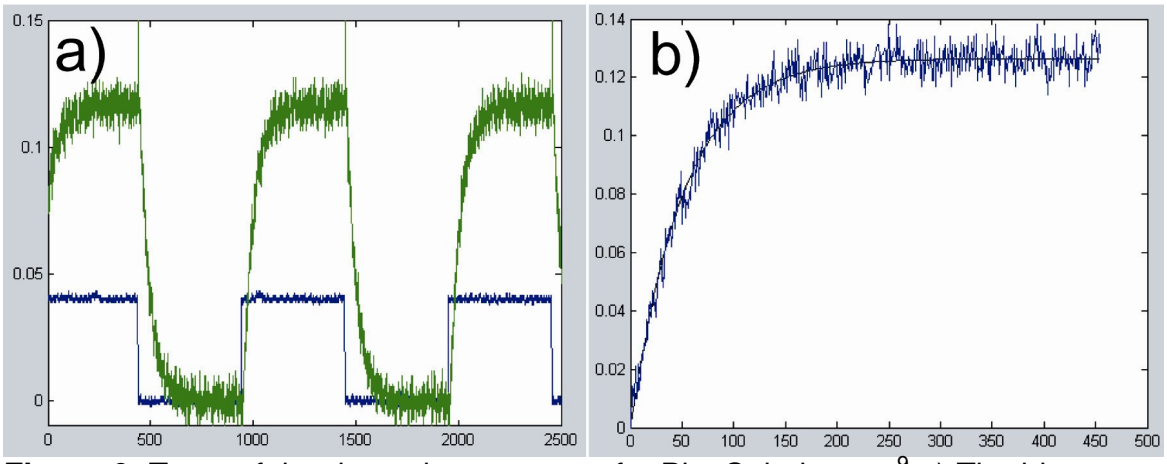

Figure 9. Tests of the dynamic response of a PicoCalorimeter.[9] a) The blue trace is the voltage applied to the on-chip heater, and the green trace is the resultant signal from the PicoCalorimeter. b) Temporal response of the PicoCalorimeter (blue) and a fit to a single exponential (black), from which we determined a time constant of 80 ms. (Courtesy of Chancellor et al.)

Droplet Evaporation Measurements

Eric Chancellor conducted experiments using HYPRES PicoCalorimeters at the beginning stage of this project.[9] He acquired very good data by delivering a droplet of picoliter (pL) size onto the PicoCalorimeter membrane and measuring the latent heat of evaporation of that water droplet as it evaporates away. An evaporation model of the droplet showed good agreement with the experiment data. The latent heat of evaporation was also calculated for different sizes of droplets. The details of this work are given in Figure 10.

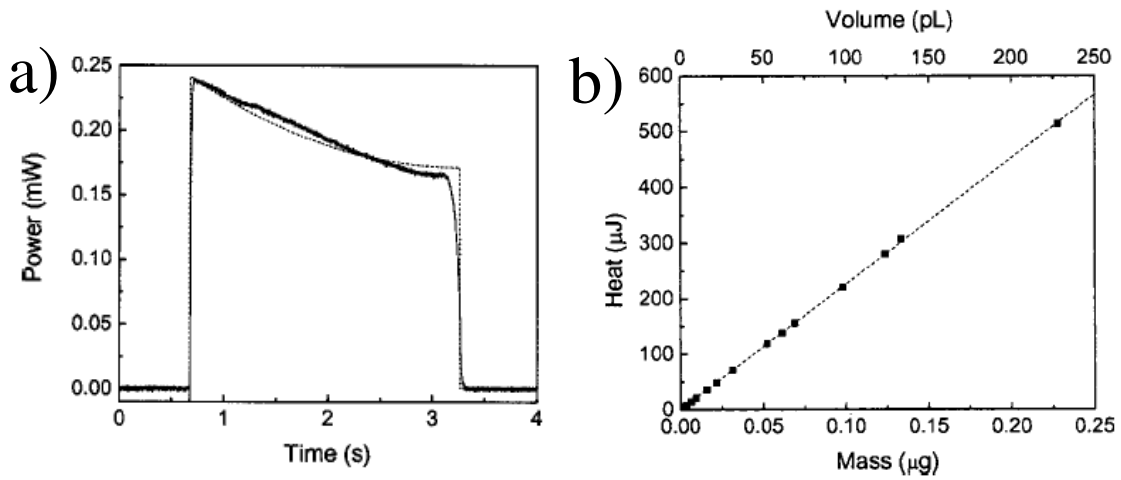

Figure 10. Chancellor's measurements of water droplet evaporation using PicoCalorimeters.[9] a). Power consumption as a 100 pL droplet evaporates (solid line), along with the modeled response of the PicoCalorimeter (dashed line) b). The experimentally determined heat of evaporation versus mass (lower *x*-axis) and volume (upper *x*-axis) for sixteen 1 to 500 pL water drops recorded by our calorimeter (j) and a least-squares fit to the data (dashed line). The slope of the fit represents the latent heat of water at room temperature. (Courtesy of Chancellor et al.)

Dexter S25 Sensor

Although the HYPRES PicoCalorimeter presents very good noise performance and very high temperature sensitivity, several factors made us decide not to use it in our experiments. First, the fabrication cost is very high so that HYPRES was not able to manufacture additional PicoCalorimeters customized for us. Second, this HYPRES PicoCalorimeter does not have a microfluidic design or a convenient mechanical design that we could easily modify for our sample delivery process. The third reason is the power sensitivity of the PicoCalorimeter, however, is not yet optimal compared to some other commercial sensors. We decided to use the S25 sensor made by Dexter Research Center Inc. (Dexter, MI). In the following paragraphs, we will introduce in detail the performance and specifications of the S25

sensor including the mechanical design that facilitated our experiments, together with some droplet evaporation data collected using S25 sensors.

Design of S25 Sensor

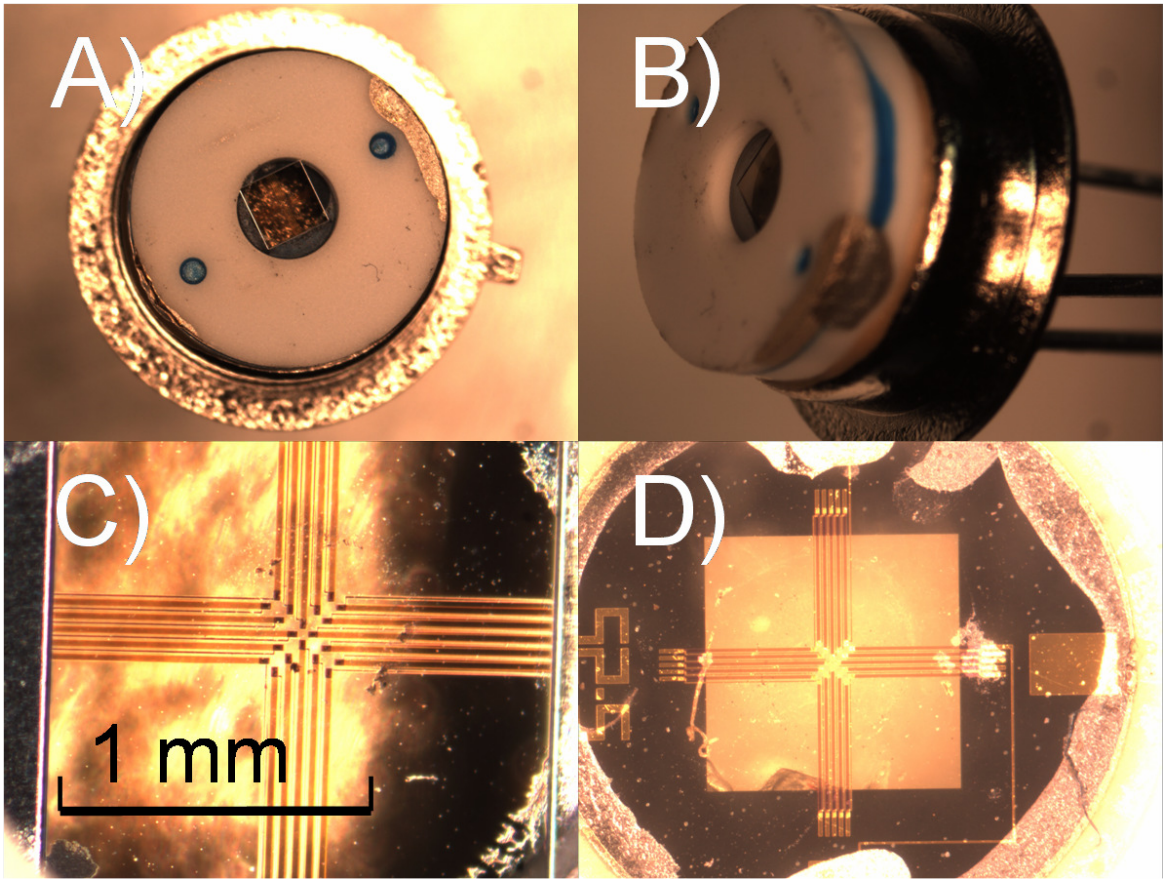

Figure 11. Photos of Dexter S25 thermopile sensor. A) Top view. The membrane is located inside a well in the center. B) Tilted view showing the 0.5 mm deep well. C) Close-up of the sensor's membrane. The black dots in the center of the membrane are the thermopile junctions. The center junction area is about 0.25 mm X 0.25 mm. D) View of the backside of the sensor membrane. The membrane is attached to the aluminum heat sink (the dark background with a square hole). The clear square is the free standing region of the membrane. The metal tracks of the thermopile run across the freestanding membrane with the sensing junctions in the middle and reference junctions located just outside the free standing region of the membrane closely coupled to the aluminum heat sink.

The Dexter S25 sensor, very similar to the HYPRES PicoCalorimeter, is a silicon-based thermopile detector. It contains 20 thermocouples in series, each of which has a Seebeck coefficient of 24 μV/K. It has a manufacturer-specified noise voltage of 19.4 $nV/Hz^{1/2}$ and a noise equivalent power of 0.1 $nW/Hz^{1/2}$. The power sensitivity of S25 is 111.5 V/W typically and the time constant is 12 ms. Of course, the power sensitivity will be greatly reduced and the time constant will be greatly increased in the experiment due to the added sample. See **Figure 11** for pictures of the S25 sensor. Please refer to Appendix A for more details of the specifications of the S25 sensor.

The membrane of the S25 sensor sits inside a well that is 0.5 mm deep and 2 mm in diameter. The well can be clearly seen in **Figure 11 b).** It is from this well that we built our reaction chamber and the sample is delivered to the center of the membrane for measurements. The membrane is about 1.5 mm X 1.5 mm square while the sensing junctions in the middle occupy a 250 μm X 250 μm space that is the sensitive area of S25 sensor. The thermopile is built on the back side so the front side of the membrane (silicon dioxide) is purely flat. **Figure 12** shows the thickness of the membrane and the dimension of the thermopile tracks via a profilometer scan. These data will later on become very important for our modeling of the sensor.

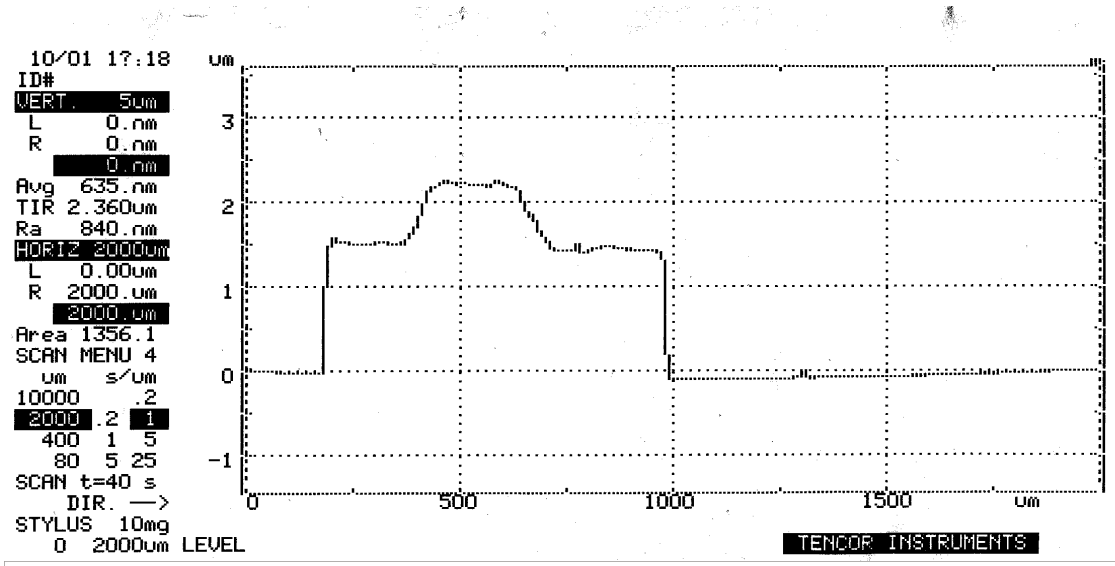

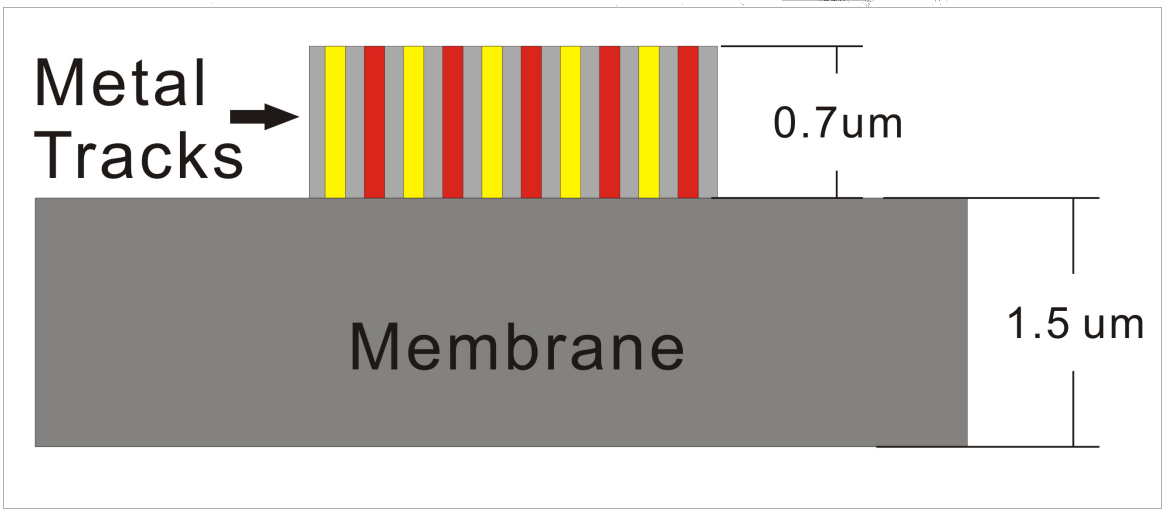

Figure 12. Profilometer scan of the back of the S25 sensor membrane. Top) The original profilometer scan recorded over a 800 μm wide broken membrane. The hump in the middle is the thermopile tracks. Bottom) The schematics of the profilometer data above. The membrane was measured as 1.5 μm thick and the height of the thermopile tracks is 0.7 μm.

Noise Performance, Sensitivity and Time Response

Figure 13 gives the result of our noise voltage measurement on the S25 sensor using our custom-built amplifier developed for our experiments. Due to the use of an amplifier, obviously we are not completely free of 1/*f* noise. The influence of 1/*f* noise is minor though, as the variation of noise voltage density from 0.1 Hz to

10Hz is only from 15-30 $nV/Hz^{1/2}$. With the bandwidth of our amplifier set at 1 Hz during the experiment, we determined that the average noise density for our sensor is 21.7 $nV/Hz^{1/2}$, or in other words, our sensor (plus amplifier) has a total noise voltage level of 21.7 nV over the 1 Hz bandwidth.

Based on the above noise voltage level, as well as the Seebeck coefficient of S25 – 480 μV/K, the temperature sensitivity of the S25 sensor was calculated to be 136 $\mu K/Hz^{1/2}$. The power sensitivity, however, is dependent on the specific environment of the experiment. During our experiment, we usually put a 50 nL aqueous sample in the middle of the S25 sensor membrane. The power sensitivity calibrated under that condition is about 2.91 ± 0.27 V/W. This is done using chemical method since the S25 does not have a built-in heater. The details of the calibration will be introduced in Chapter V, Calibration of the Sensor Using Chemical Methods.

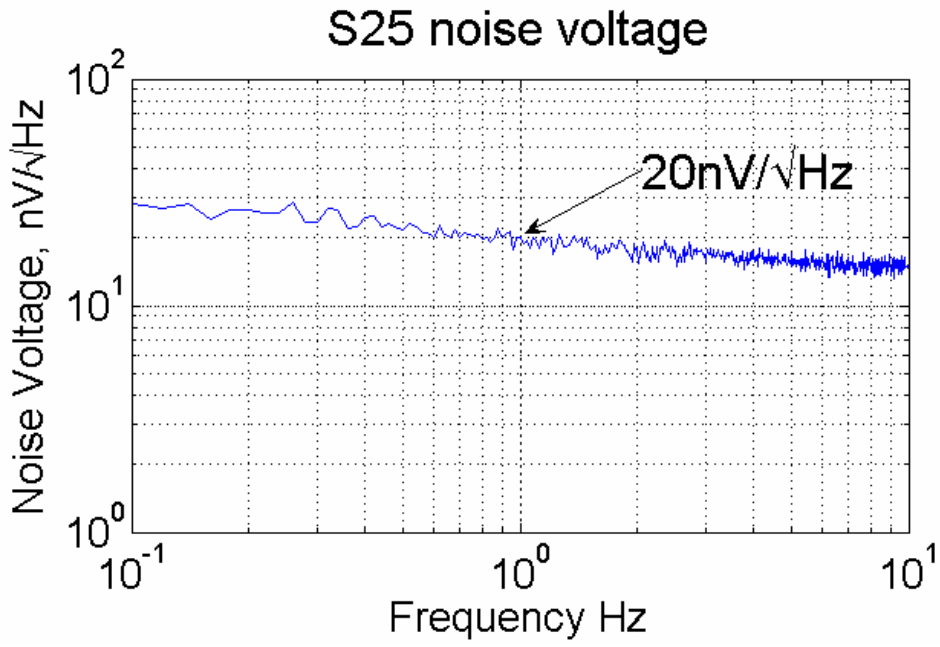

Figure 13. Measured calorimetric system noise voltage density. The 20 nV/√Hz is the noise voltage density at 1 Hz with a low pass cutoff of 10 Hz.

The time constant of the sensor is given by the company as 12 ms. This number is only for the situation of a free membrane, though, and will vary greatly by a lot if there is a bulk amount of sample on top of the membrane. The time constant for the impulse response was modeled and measured in experiment. The modeling result agrees with the experimental time constant at ~1.3 seconds. The modeling will be introduced in Chapter IV, Modeling of the Sensor and the chemical experiment for measurement of the time constant will be introduced in Chapter V, Chemical Methods of Calibration.

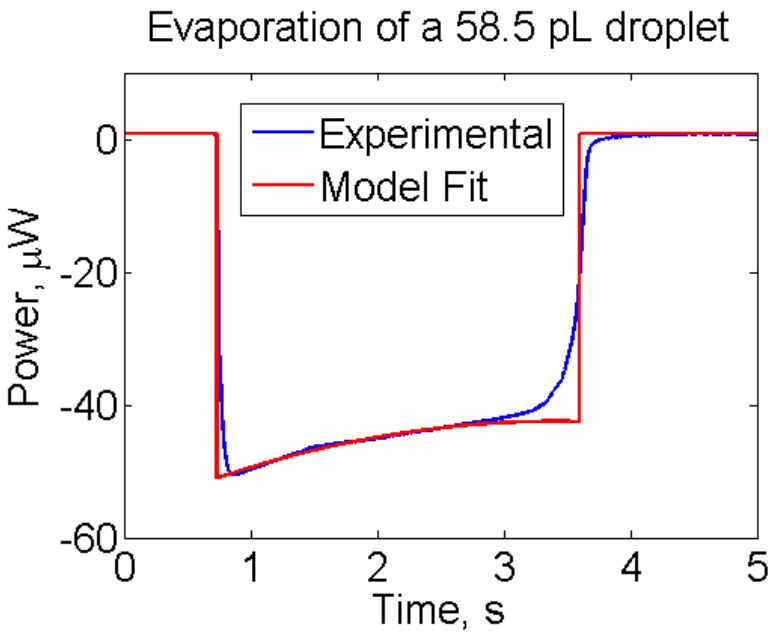

Figure 14. Measurement of the power consumption from the evaporation of a 58.5 pL water droplet (blue line), compared with the theoretical model of that (red line).

Droplet Evaporation Measurements

The same type of experiment Eric Chancellor conducted using the HYPRES PicoCalorimeter was done using the Dexter S25 sensor. The experimental data

were then compared to a theoretical model. The size of the droplet and the total power consumption were then estimated via the model using the factory given power sensitivity of 111.5 V/W. The experimental and modeling results are shown in **Figure 14**.

A series of evaporation experiments were done using the S25 for different droplet volumes and the total heat consumption of the evaporation of those droplets was calculated. We then could draw a graph of the droplets' heat consumption of evaporation versus their masses. The latent heat of evaporation was then calculated by doing a linear fit to these data. See **Figure 15** for the data and the deducted latent heat of evaporation.

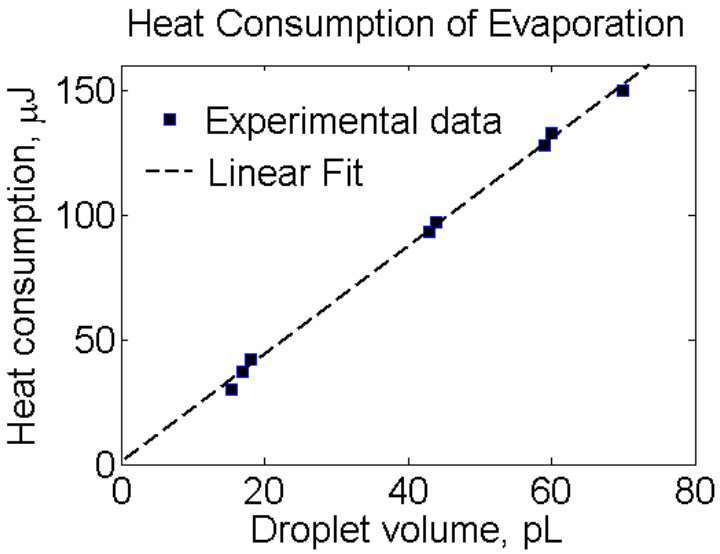

Figure 15. Heat consumption of evaporation for different sizes of droplets. Based on the linear fit of the data, the latent heat was calculated to be 2232±121 J/g, compared to a theoretical value of 2443 J/g.

From the linear fit of droplet evaporation heat consumption data, we calculated the latent heat of evaporation for water at room temperature to be 2232 J/g, slightly (~10%) lower than the theoretical value of 2443 J/g. The error is mostly because the power sensitivity provided by the factory is probably higher than the true power sensitivity of our sensor in the experiment. Also, thermal leakage may have contributed to the fact that our result of latent heat is lower than the theoretical value. However, these experiments demonstrated the sensor's sensitivity and its functionality when there are liquid samples on it.

Noise and Low Noise Amplifier Design

Noise is always a problem in experiments aiming at measurements of ultra-low signals. This is the case for our application. As our reaction chamber can hold from tens to hundreds of cells, the expected signal is in nanowatt range or even lower.

There are three main types of noise mechanisms: thermal noise, low-frequency noise and shot noise. Thermal noise is the most often encountered type and exists in all resistive components. The RMS noise voltage of a resistance R is[49]

$$E_t = (4kTR\Delta f)^{1/2} \quad (18)$$

where k is Boltzman constant, T is temperature and Δf the bandwidth.

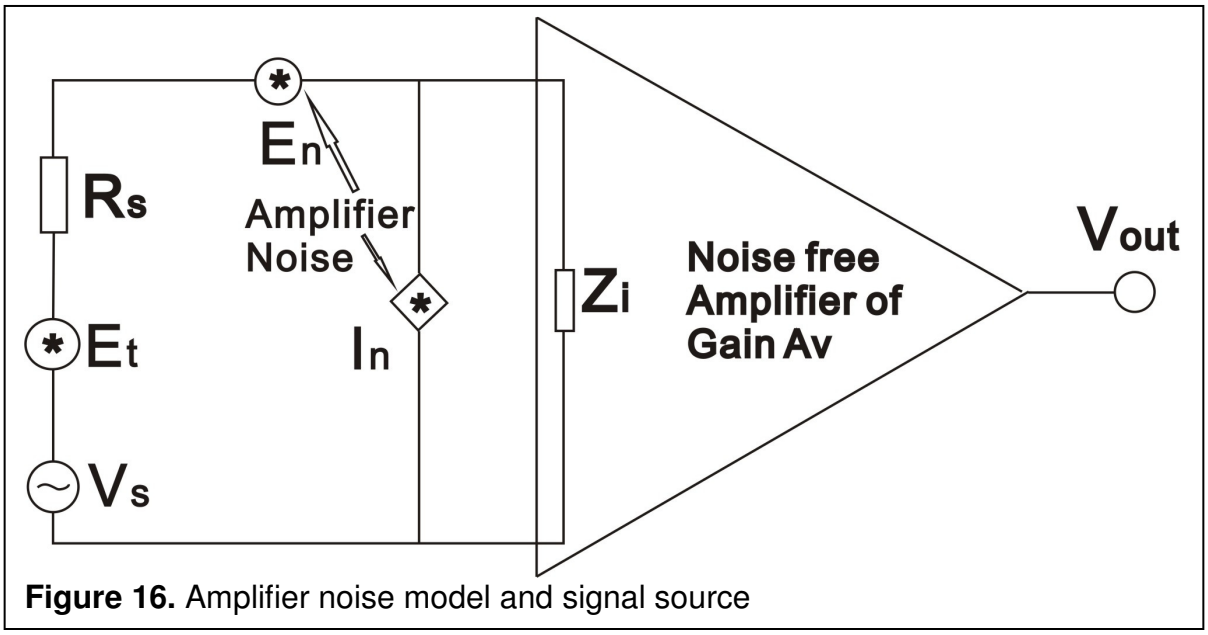

Figure 16. Amplifier noise model and signal source

As the sensor's output is a very small voltage, an amplifier is necessary for signal collection. A universal model for the sensor-amplifier[49] system is shown in Figure 16. The signal source is described by a noiseless resistor R_s, a noise voltage source E_t and a signal voltage source Vs. The amplifier noise (input end referred) is represented by a combination of noise voltage E_n and noise current I_n. The equivalent input noise can be expressed as:

$$E_{ni}^2 = E_t^2 + E_n^2 + I_n^2 R_s^2 \qquad (19)$$

Based on this equation, further discussions could be made using noise figure[50,51] and other methods which can help the engineer to build the circuit based on the sensor's property. Our amplifier consists of an instrumentation amplifier (INA128, Burr-Brown) and a second stage amplification using an op-amp (AD711JN, Analog Devices) in an inverting configuration. A low-pass filter (cut off frequency 1 Hz) is provided at the end to filter out high frequency noise. The noise performance of the

S25 was measured and compared to the PicoCalorimeter. Details will be given in the following section.

There are other considerations in the circuit design concerning the noise performance, such as the shielding of circuit and signal routes, and the printed circuit board (PCB) layout. Poor shielding and grounding problems are usually the reason for RF induction. Problems requiring care in PCB design include grounding, trace antennas, trace to trace capacitance and inductance, inductive vias, decoupling capacitors and overall component geometry.[52] These aspects have been taken into careful consideration during the design of the PCB for our amplifier and the overall electronic layout.

The above discussions on noise are mostly about the electronics, while the other important source of noise comes from the environment. As this thermal sensor is extremely sensitive, to achieve a reasonable signal to noise ratio down to nanowatt range signal, we must make a tremendous effort to reduce environmental noise. Any heat/IR source must be isolated from the sensor as clearly as possible. Possible sources include microscope illumination (thus it is desirable not to turn on the microscope light source for observation and adjustments during measurements) and the human body. Long-term fluctuation of ambient temperature is not as serious a problem as heat source, since our measurements usually last from minutes to within an hour and our setup includes a large incubator which can isolate the device from the room air. Constant radiation sources such as room lighting and computer monitors will change the baseline offset, which is acceptable but should be minimized wherever possible.

Comparison between HYPRES PicoCalorimeter and Dexter S25

Both the HYPRES PicoCalorimeter and the Dexter S25 have excellent performance on noise and sensitivity. The noise performance of the S25 sensor is measured using our current experimental setup and is then calculated using the FFT method. The results are compared with measurements done with an HP3526 spectrum analyzer and are confirmed to be the same (the HP3526 analyzer is an analog rather than a digital spectrum analyzer). The results are further compared with the HYPRES sensor and the nanocalorimetric sensor made by Johannessen et al. (this group possesses the most sensitive calorimetric sensor in the current publications working on the application of nanocalorimeter in biological measurements). The detailed comparisons are shown in Table 2.

Table 2. Comparison of the Johannessen (published), S25 and Hypres sensors

Device\Property	Noise, $nV/Hz^{1/2}$	Sensitivity		
		Voltage, $nV/Hz^{1/2}$	Temperature, $\mu K/Hz^{1/2}$	NEP $nW/Hz^{1/2}$
Johannessen	9.2	28	125	4.3
Dexter S25	21.7	65.1	136	7.6
HYPRES	14	42	21	2.2

Obviously, the HYPRES PicoCalorimeter exceeds both the S25 and the Johannessen nanocalorimeter in temperature sensitivity due to its high Seebeck coefficient and low noise voltage. However, the S25 sensor presents comparable power sensitivity despite its higher noise level due to its specific mechanical design of freestanding membrane. The Johannessen sensor is subject to a large disadvantage in power sensitivity due to the oil cover they used to prevent

evaporation (since that greatly increased the heat conductance of the sensor from sensing junctions to heat sinks). The HYPRES sensor suffers the same problem because it lacks a mature mechanical design to accommodate the liquid sample. The S25 used in our experiment, however, due to our innovative mechanical design, is able to sustain the liquid sample while still having a tiny heat conductance from its sensing junctions to heat sink. We will introduce our design in Chapter III, Equipment and Methods. It turned out that power sensitivity is the most important issue in nanocalorimeters for biological experiments since temperature change is relative and is subject to the sample volume, oil cover, etc, while the power generation is absolute and is only related to the sample's thermal characteristics (whether cells are metabolically active or thermally productive). Thus, our innovative mechanical design for thermal shielding, evaporation prevention and sample delivery enabled us to convert a commercial infrared sensor into a thermal sensor for measurements of biological thermal signals that could match the current best technology.

CHAPTER III

EQUIPMENT AND METHODS

This chapter will introduce all the equipment and methods used in our project. The ultimate goal is that after reading this chapter, one could reproduce the results we have obtained by using the same methods and equipment. The major methods and procedures involved are data acquisition, liquid sample delivery, thermal shielding, and evaporation prevention. A checklist of the critical equipment/materials and their purchase information is provided in Appendix B. We will discuss all the equipment and methods individually below.

Data Acquisition System

The data acquisition system includes the hardware for amplification of the signal and signal transmitting, and the software for signal processing and recording. We will discuss these two parts separately below.

Hardware

The hardware of the data acquisition system includes these major parts: PCI-6024 DAQ board, amplifier box, BNC-2120 connector box, and the computer. The schematic of the hardware involved in the signal flow is shown in **Figure 17**. The voltage produced by the sensor is first transmitted to the amplifier via a special mini connector that the sensor could be directly inserted into. This voltage, after being

amplified by the amplifier, is then transmitted from the output end of the amplifier to the BNC-2120 connector box via a BNC cable. The signal is then passed onto the PCI-6024E data acquisition (DAQ) board which is inside the computer and the data are acquired and shown on the LabVIEW interface.

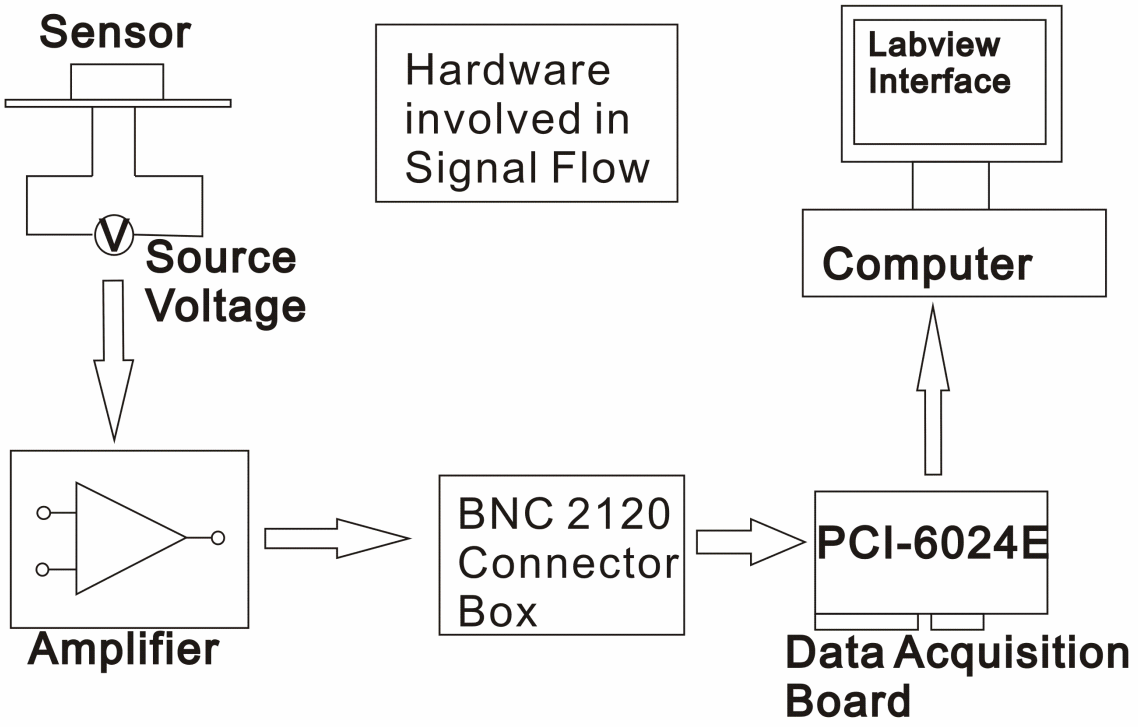

Figure 17. Hardware involved in signal transmission and data collection.

The BNC 2120 connector box is specifically designed to interface between the PCI-6024E DAQ board and the signal source coming from a BNC connector. It has various grounding schemes for different signal sources. For our experiment, we have a thermopile which provides a floating voltage signal. According to the user manual of the BNC 2120, the channel needs to be set to Floating Signal (FS) status

and the PCI-6024E board should be set to differential mode accordingly for appropriate signal transmission. The details of this scheme are shown in **Figure 18**.

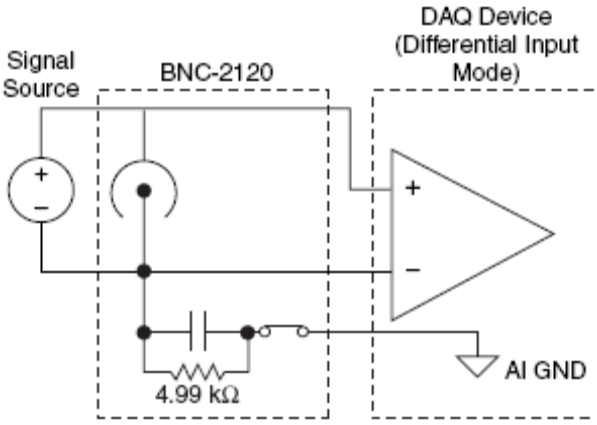

Figure 18. Grounding scheme of BNC-2120 connector box and the DAQ device's corresponding setup mode.

Both the BNC-2120 and PCI-6024E are made by National Instruments (NI). The 68-pin shielded connection wire which connects the BNC-2120 to the PCI-6024E is also made by NI. Detailed purchase information for these components can be found in Appendix B.

The amplifier box includes a custom printed circuit board (PCB) and the circuit components installed onto it. The schematic of the circuit is shown in **Figure 19**.

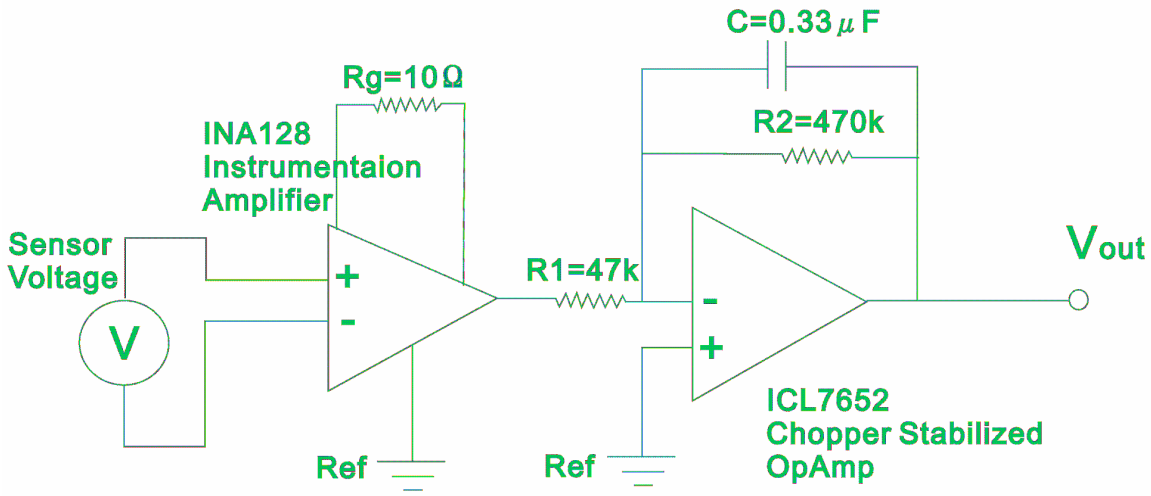

Figure 19. Circuit diagram of the amplifier circuit.

The circuit basically has two stages: the first is the INA 128 instrumentation amplifier which can provide a gain of up to 10k and the second is an inverted setup op-amp which gives an extra gain of 10 and a low-pass filter with cutoff frequency of 1 Hz. In practice, we used the sensing resistor of 10 Ω so that the gain of the instrumentation amplifier is about 5k. So together with the gain of the second stage, which is 10, the total gain is 50k during our measurements. That proved to be a high enough gain to measure the biological thermal signal produced by the cardiomyocytes or the heat production from chemical reactions. The capacitor in the second stage (0.33 μF) is used to filter out the high frequency noise and it provides a cutoff frequency of 1 Hz. It is with this 1Hz bandwidth that we achieved a total noise level of 65 nV. The ICL7652 chopper-stabilized operational amplifier (opamp) is used to reduce the 1/f noise in the circuit. This type of opamp possesses great ability in controlling the 1/f noise and it is critical for our noise reduction since our total bandwidth is only 1 Hz.

The circuit board was first designed using Altium design software Protel DXP and the design was then fabricated by Advanced Circuits (www.4pcb.com) into the PCB. The chips and other components were then soldered onto the PCB to complete the circuit. The PCB schematics and board layout of the circuit are provided in Appendix C.

Software

The software side of the data acquisition system is fairly simple compared to the hardware side. A LabVIEW program is used to perform the signal acquisition, real-time display and recording. LabVIEW 7.0 made by National Instruments is used here. The LabVIEW program's front panel (user interface) is shown in **Figure 20**.

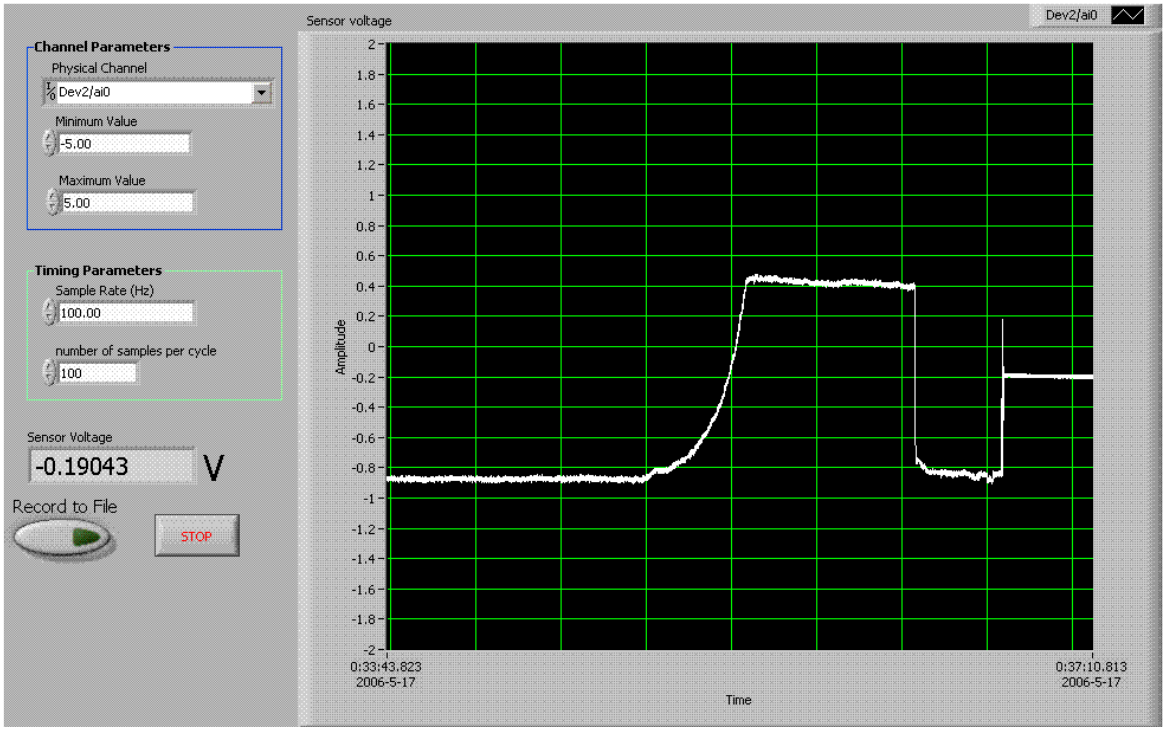

Figure 20. LabView front panel of the data acquisition program.

The range of signal input and the sample rate of the data collection are adjustable. There is also a record button so the user can determine, while monitoring the signal from the sensor, when to start recording data and when to stop. Due to the limited range of the PCI-6024E board, the range of data is usually set to -5 V to 5 V to compromise between the resolution of the DAQ and the range of input. It is good to set the sampling rate to 100 Hz during fast-paced experiments, such as the chemical reaction experiments. For biological signal measurements, where fast changing signals are less likely to happen and which requires about an hour to complete, a lower sampling rate such as 10 Hz is more desirable since it can reduce the file size and the difficulty of data processing greatly.

Sample Delivery System

For a miniature system like ours, it is always very important to ensure the delivery of the correct amount of sample onto the right place. In our experiments, we have two major pieces of equipment to complete that goal: one is an Eppendorf 5171 Micromanipulator which controls where the sample will be delivered; the other is Picospritzer II made by Parker Hannifin, which controls the amount of the sample to be delivered. Another important apparatus is the glass pipette to be used with the Picospritzer as the same setup of the Picospritzer could result in different sample volumes with different pipette tips. We will discuss further all three components in the following sections.

5171 Micromanipulator

The micromanipulator (Eppendorf 5171) can control the movement of the pipette tip in a precision up to 1 μm. Such a precision was critical in allowing us to deliver the cell solution directly onto the center of the sensor's membrane. See **Figure 21** for a picture of the micromanipulator and its control joystick.

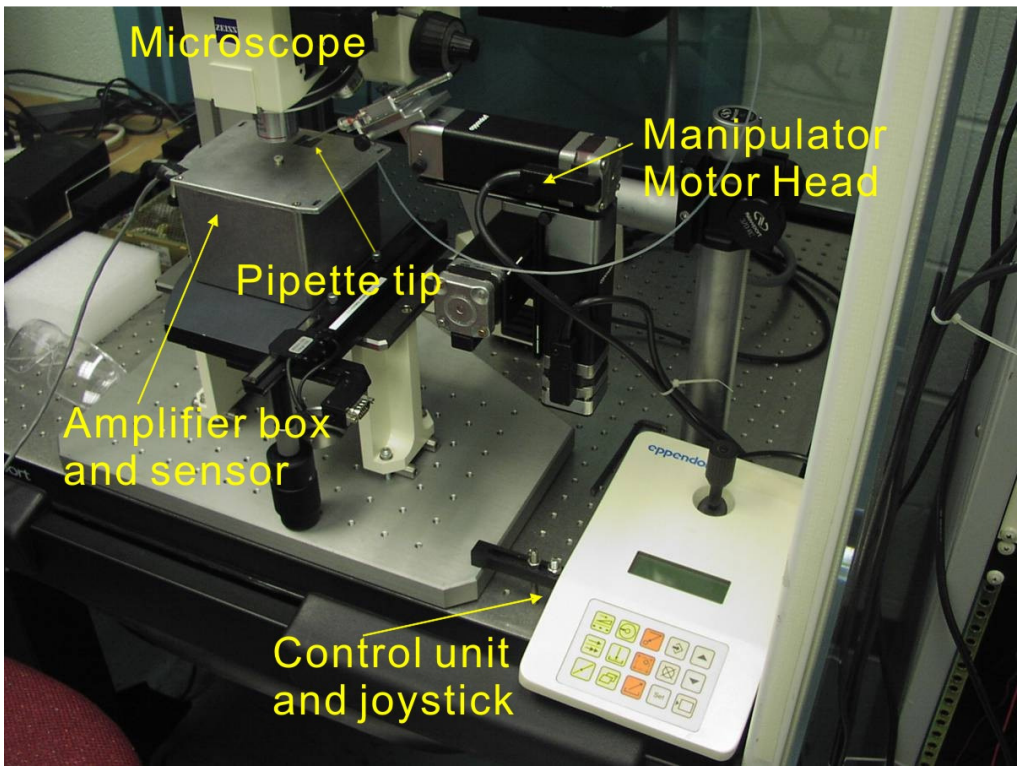

Figure 21. Picture of the micromanipulator as in experimental setup.

There is an injection/impale function on the micromanipulator so that a position for the pipette to reach can be preset. Then, after retraction of the pipette to a certain location, it can both reach that preset position and retreat to the original position when the injection button is pressed. This allows us to move the pipette tip back and forth between two preset positions, with one being the injection position

and the other being the resting position. Furthermore, this could be done without looking at the pipette tip and one would know that it will travel to the desired position once it has been set. This is especially important since we cannot turn on the microscope during the experiment because the microscope light source will introduce a great deal of noise to our sensor. With the help of the 5171 micromanipulator, we are able to move the pipette tip between the injection position and the resting position without turning on the microscope light source. This “no-look” movement is definitely one of the keys to the success of our project.

Pneumatic Drive Picospritzer II

The key of our sample delivery is to deliver droplets/solutions of volume in nL or even pL range with precision. This is achieved by using the Parker Hannifin Picospritzer II. See **Figure 22** for a picture of Picospritzer II front panel.

Figure 22. Front panel of Picospritzer II.

The Picospritzer is basically an electronic control unit that could control for how long the valve will be switched on. The valve is connected to a compressed air

source such as a gas cylinder and the pressure could be controlled by the regulator on the Picospritzer. So there are two factors we could control on the Picospritzer II: the pressure and the duration to apply such a pressure. It turns out that both factors have good linear relationships with the injected droplet volume. See **Figure 23** for the measurements of such characteristics. [53]

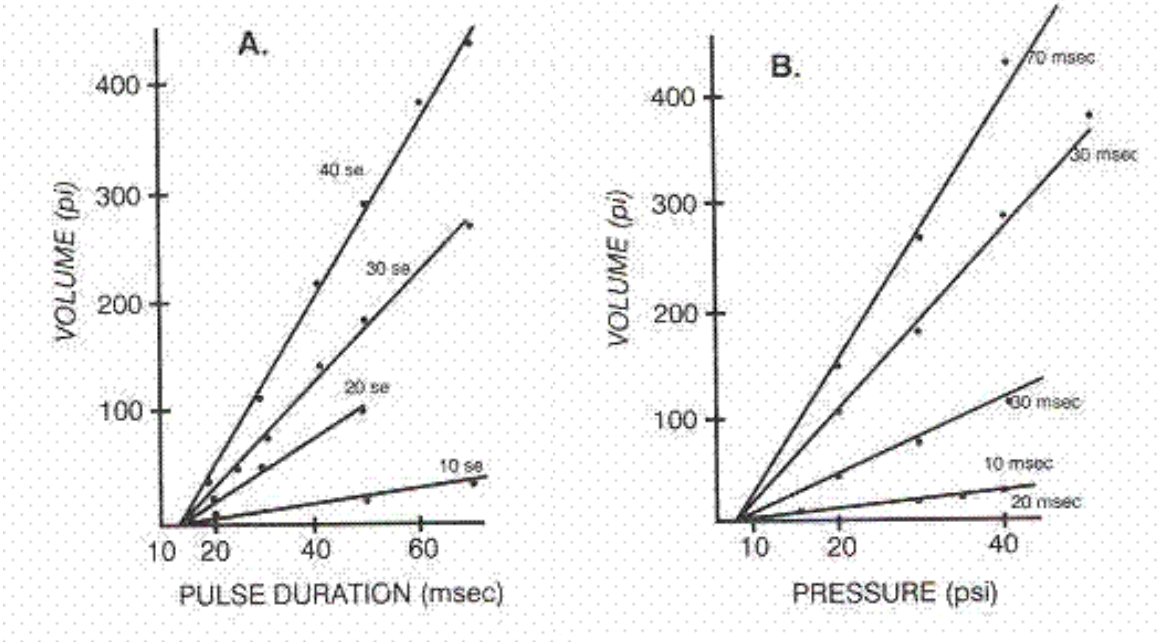

Figure 23. Linearity of injection volume to injection pressure and pulse duration. A) Linearity of volume ejected with varying pulse duration at constant pressure. The X-intercept represents the mechanical lag time of the particular valve. B). Linearity of volume ejected with varying pressure at constant pulse duration. The X-intercept represents the minimum pressure necessary for ejection and is a characteristic of a particular pipette. (from McCaman et al.)

We could see from the figures that at constant pressure, the ejected volume is linear with the pulse duration. However, there is a minimum pulse duration required to activate the valve and it was measured as 15 ms on the graph. We

determined that for our valve this minimum pulse duration is about 3 ms. During our experiments, we usually set the pressure to a constant 30 PSI and we would vary the pulse duration to control our injection volume. However, as the volume-versus-duration curve depends on specific pipette, one has to do a calibration on injection volume (as pulse duration changes) for the specific pipette in use. If the pipette is switched for some reason during the experiment, the volume calibration has to be done again for the new pipette. The calibration could be made by doing a number of injections (such as a thousand) and measuring the total volume dispensed to find the volume of an individual injection. The measurement of the total volume dispensed is done by marking the liquid's position inside the capillary before and after a number of injections, then measuring the total length of liquid being dispensed. The volume will then be this length multiplied by the inner area of the capillary. The variation in droplet injection of such size has been demonstrated to be less than 2.3% in measurements of the droplet sizes ejected with similar protocol.[54] We will talk more about the pipette in the next section. The details of control of injection droplet sizes will be given at the end of the pipette section.

Glass Pipette

The glass pipette was pulled using the pipette puller. Glass capillaries were purchased from World Precision Instruments (WPI). See Appendix B for purchase information on the glass capillaries.

Two processes are necessary to form the desired injection pipette. The first process is pulling. We use the Narishige PB-7 micropipette puller. See **Figure 24** for

pictures of Narishige PB-7 micropipette puller and four pulled pipettes to be used in experiments. We will discuss the details of the pulling protocol to make different pipette openings in the following paragraph. Aside from pulling, it is also necessary to make the pipette hydrophobic before putting them to use. The reason is that glass is usually hydrophilic and the pipette could “suck” the watery sample out if not processed to be hydrophobic.

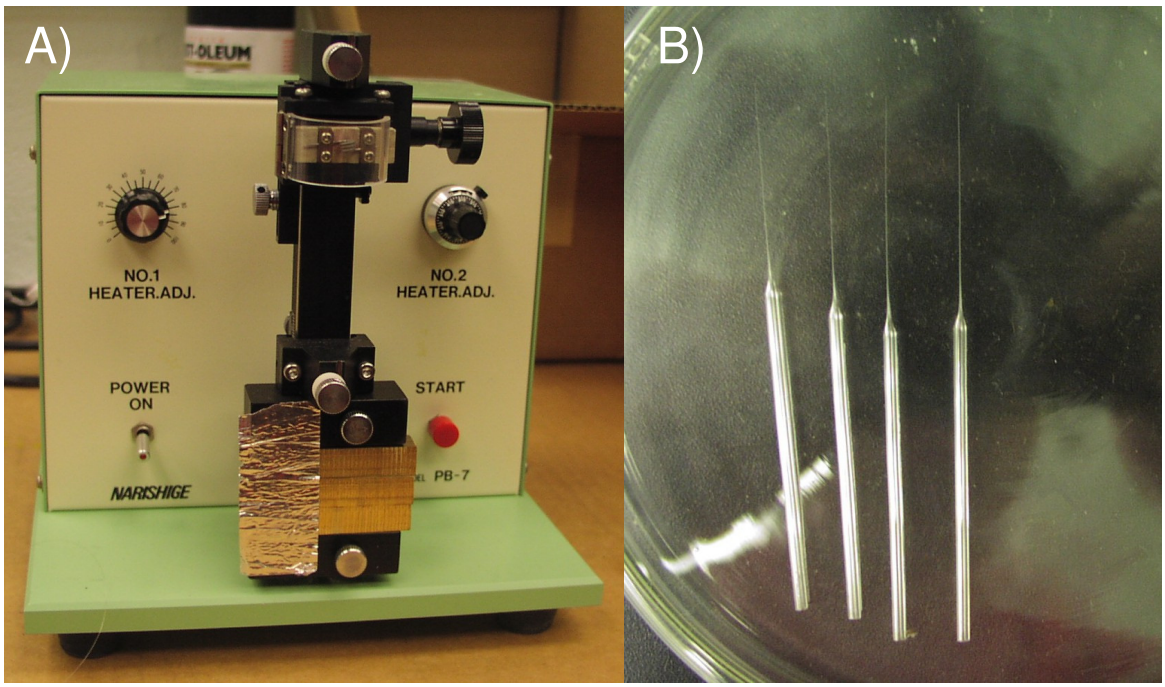

Figure 24. A) Narishige PB-7 pipette puller B) Four pulled pipettes

The ideal micropipettes we use in the experiments should have long and thin necks so they are flexible at the end. This is very important because if the pipette is too stiff, it will destroy the sensor membrane upon contact. We want the pipette to be able to touch the sensor without destroying it so we can move the pipette back and forth and up and down to find the best spot of injection. Also, a long neck is

necessary because the pipette needs to travel down to the sensor through a double hole with the inner hole's opening being only 100 μm in diameter. There are two factors we can adjust on the Narishige pipette puller – the weight and the heat. The weight is basically how much force is to be applied during the pulling process and the heat is a percentage of the heater current. It also has a two-stage pulling function. However, we found that one-stage pulling is enough to produce all the pipettes we want so we never used the two-stage pulling method. We turn the No.2 heater adjustment knob to adjust the heater current. We also always used two weight blocks (the Narishige puller can accommodate four). So the opening size of the pipette is now determined by the heater current. **Table 3** gives a general description of how much heat to use to produce a certain size pipette.

Table 3. How to produce a certain size micropipette

Heater current % (No.2 Heater)	Natural/manual breaking	Pipette opening size (μm)	Application
91-93%	Natural breaking	1-5	Fine injection of chemicals (<1 nL)
93-95%	Natural breaking	5-20	Injection of medium/solution
95-97%	Manual breaking	40-100	Injection of cell solution

We see from the table that the pipette size varies from 1 μm to 100 μm. Which size of pipette we choose to use depends on whether we need to inject just a trace amount of liquid or cell solution (cardiac cells are large, usually 10X100 μm, so they require a big pipette tip opening to be delivered). Sometimes the glass capillary will be broken into two halves (and thus two micropipettes) at the end of the pulling

process, which is called natural breaking, and sometimes the capillary is not broken at the end of the pulling process and has to be broken by applied force (i.e. using one's hand to pull it apart), which is called manual breaking. Whether or not the capillary will be naturally broken at the end of the pulling is somewhat haphazard, especially if the heater current is adjusted to around 94%. With the same heater current, a naturally broken micropipette will usually have a much smaller opening than a manually broken one. This is why it is important to point out whether the pipette is naturally broken or broken by hand in **Table 3**. However, below 93% heater current, it is almost always naturally broken, and above 95% heater current, it is almost never naturally broken.

So the general procedure to pull the right pipette is as follows:

1. Set the weight of the puller to two blocks.
2. Adjust the No. 2 heater current as necessary based on the data in **Table 3**.
3. Press the "start" button and let the puller finish. Make sure the pipette is naturally (or manually) broken as required in **Table 3**.

The pipettes made using this protocol usually have long necks and will possess the desired opening size. However, we noticed that there is a lot of variation in the pipette opening size for pipettes pulled with the same protocol (e.g., same heater current, same weight, and same breaking method), especially for those pipettes with an opening size around several microns. For this reason, all pipettes pulled have to be examined using the microscope to make sure they are in the correct range of sizes. When put to use, every single pipette must be calibrated for

the injection volume versus pulse duration of the Picospritzer (because this curve is dependent on the pipette opening size).

After the pulling, our micropipette should be in the right shape. However, one more thing we need to do is to make it hydrophobic. Since most of the samples we use in the experiments are water-based, if the pipette is hydrophilic, the water will climb up the pipette wall as long as the pipette is in contact with the sample. This could make our injection volume inaccurate or even drain our sample in the reaction chamber (but not in the desired way). To avoid this, we must silanize the pipette tip to make it hydrophobic. The protocol for silanizing the tip is as follows:

1. Always wear personal protection equipment, including nitrile gloves, goggles and lab coat when working with silane solution.
2. Use a large Petri dish. Spin a film of PDMS onto the inside of the Petri dish (so that the glass pipette would stick to it) and the inside of its cover (to ensure good sealing during baking). Let the PDMS cure.
3. Put the pipettes in the Petri dish. Place the Petri dish in the oven. Pre-bake for 10 minutes at 400 F to remove vapor that could interfere.
4. Transfer 60 µL of N,N-dimethyltrimethylsilylamine (TMSDMA) into a small vial, put it in the Petri dish cap-off, close the cover. Put the covered Petri dish back in the oven.
5. Bake for an hour (400 F).
6. Allow the pipettes and the Petri dish to cool down to room temperature. Store the pipettes in a closed Petri dish.

The silanized pipettes demonstrated good hydrophobicity. However, they would gradually lose this property during storage, so the pipettes used in experiments must be prepared fresh or no more than a couple of days before the experiment. Still, during the experiment, the pipette should be taken away from the sample once the injection is finished to ensure no loss of the sample during the experiment.

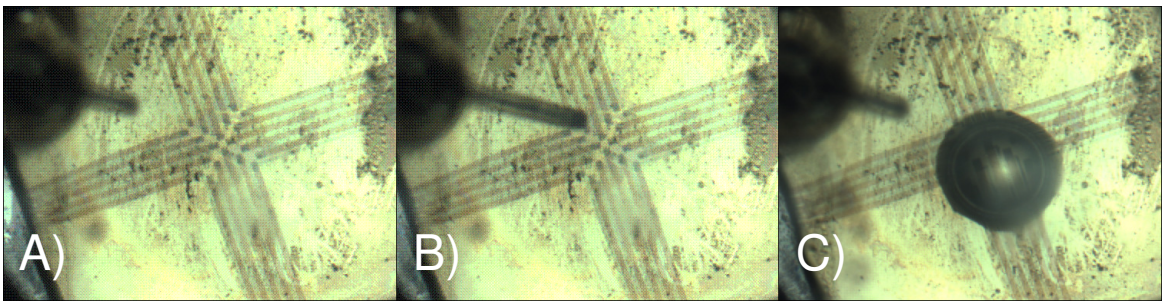

Figure 25. Demonstration of injection process – injection of a 20nL droplet onto the center of the nanocalorimeter membrane. A) Pipette at resting position before injection. B) Pipette reaching onto the membrane surface. C) Droplet injected and pipette retracted to resting position.

General Sample Delivery Protocol

With the pipette and Picospritzer ready, we now could deliver our droplet at the volume we want! A series of pictures demonstrating the sample delivery process is shown in **Figure 25**. There are some general rules for using the Picospritzer. First of all, since it takes at least 3 ms to activate the valve on the Picospritzer, we would like our pulse duration to be far above this time to reduce variations of delivered droplet sizes. On the other hand, we do not want the pulse duration to be too long as we want the injection to happen quickly and accurately. The ideal pulse duration should be between 20-100 ms. We could then select the pipette size based on this.

Secondly, the pressure should be moderate. As with the pulse duration, it takes some minimum pressure to actually inject something for a certain pipette. In experiments we found that even for pipettes below 5 μm, 30 PSI is good enough to accomplish a good delivery. Hence 30 PSI is what we used for all injections because we do not want the pressure to be too large either as that will make the pipette move during the injections. We have summarized the general selection of pipettes and possible pulse durations to use for certain volume injections in **Table 4**. This is by no means an accurate reference but is just a general guideline, because there are many other factors that could affect the injection volume even with the same pressure, same pulse duration and same pipette opening size. These factors include the detail of the pipette opening's shape, the pipette wall's property, and the liquid sample's composition, etc.

Table 4. Selection of pipette sizes and Picospritzer pulse durations for certain volume injections.

Pressure (PSI)	Pulse duration (ms)	Pipette opening (μm)	Injection volume (nL)
30	20-100	<5	<1
30	20-100	5-20	1-10
30	20-50	>20	10-100

Thermal Shielding and Evaporation Prevention

The thermal shielding of the system is critical to our experiment as the sensor is very sensitive to the slightest bit of thermal noise. It is also important to prevent any evaporation of the sample inside the reaction chamber since evaporation consumes a huge amount of heat and will become intolerable noise were it to occur.

The thermal shielding of the system and the prevention of evaporation are provide by the integrative nature of our experiment design. We will introduce the integrated system part by part in the following sections.

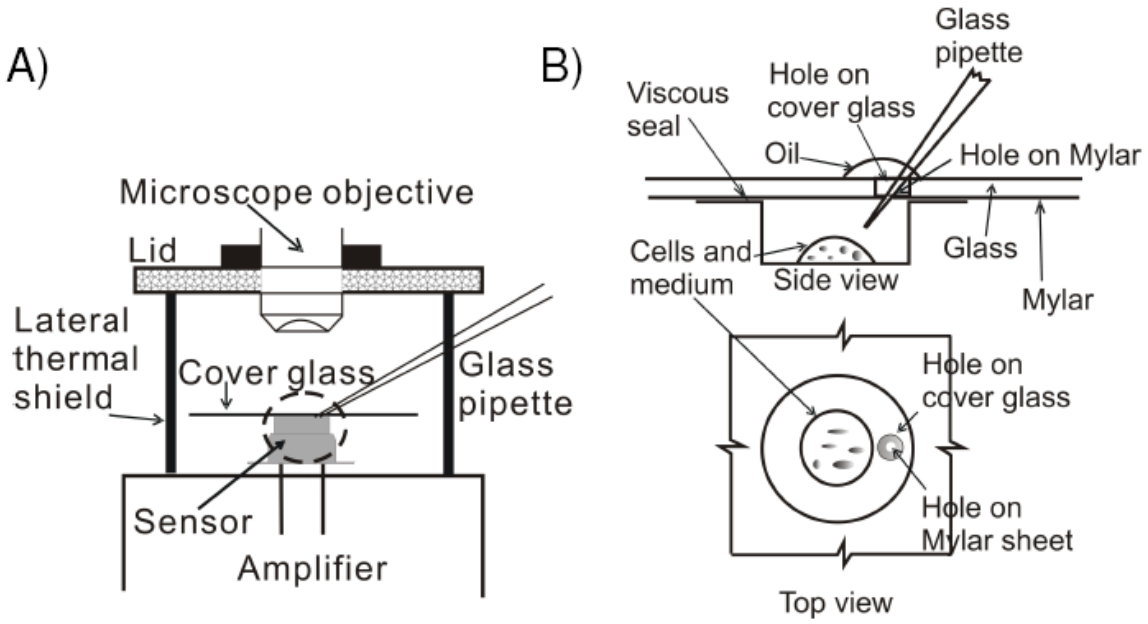

Figure 26. General setup of the integrative system for thermal shielding and evaporation prevention. A) Grand view of the system B) Detailed view around the sensor.

The General Picture

The general picture of the integrated system for thermal shielding and evaporation prevention is shown in **Figure 26**. The outer shield consists of a metal ring and a rubber gasket. There is a slot on the metal ring to allow the pipette to be inserted for injection. There is a hole in the center of the gasket so the microscope objective can enter to the right position for observation. Due to the slot in the metal ring, the outer shield does not completely seal the space inside. However, there is another layer of shield inside that outer shield that will ensure the sensor is shielded

from environmental noise. That inner shield is basically a combination of a cover glass and Mylar on top of the sensor. A double hole system on this shield has a special function of allowing the pipette to go in and out while mineral oil applied on the double holes can still seal the reaction chamber. We will talk about this in detail in a later section.

Double Holes and Evaporation Prevention

The evaporation of the sample has to be avoided to acquire useful experimental data since the sensor is very sensitive to the thermal drift associated with even a trace amount of evaporation. Our reaction chamber was defined by two things: 1) the well in the S25 sensor, as shown in **Figure 11**; 2) the cover on top of the sensor which is a piece of cover glass with Mylar sheet attached to its bottom. It is not enough yet just to stop the evaporation because our pipette will have to go inside the reaction chamber for injection. So we designed a double hole system on the cover glass-Mylar combination to allow the pipette to move in and out freely with the system still sealed. A thin layer of mineral oil (paraffin) is applied on that double hole to seal it. The hole on the cover glass is about 0.6 mm in diameter and the hole on the Mylar sheet is about 100 μm in diameter, which is small enough so that it could hold the oil there with surface tension. A single hole on the cover glass is not enough to do this. However, Mylar is thin and is not a good shield of IR source but glass proved to be a good shield. So this double hole system ensures good insulation of the sensor from the environmental noise and on the other hand still allows the injection to happen freely.

Drilling on the cover glass requires a 0.023 inch in diameter diamond drill bit (Technodiamant Company). The details of the purchase information are in Appendix B. Water must be applied to the drilling surface for both cooling and lubricating. When drilling on the cover glass, a piece of glass slide must be put under the cover glass. The drill bit must be raised up from the drilling surface after drilling to a certain depth (probably every 0.005 inch) to allow it to cool and to clean the waste. This is because the drilling on the cover glass is more like milling and will produce tiny glass tips which are destructive to the drilling process. Since we do not have a water swivel installed on the mini drill press, such waste has to be removed by raising the drill bit occasionally to ensure a clean and less fractured drilling on the cover glass. Once the hole drilled through, water will drain from the top of the cover glass being drilled to the glass slide under it. So drilling can be stopped once we see the water flowing underneath the cover glass.

Sealing of S25 Using Photoresist

As noted earlier, our reaction chamber consists of two parts. The cover glass and Mylar combination is the cover. The well in the S25 is the body. In between the cover glass-Mylar layers and the S25 sensor, we again use some mineral oil (paraffin) to seal the gap. However, we do not want any of the oil to leak inside the reaction chamber as that will greatly reduce the sensitivity of the device. It is somewhat tricky to apply just the right amount of oil but with some practice and experience, one will know how much is just enough.

Although everything seems to be sealed up, there is one thing that is still leaking -- the sensor's well itself. In **Figure 11D** we see the back of the sensor and that the membrane is actually attached to the top porcelain part which forms the well. This attachment, however, does not provide a gas tight seal. For this reason additional sealant has to be applied to the circular edge of the bottom of this well. We chose to use the S1813 (Shipley) photoresist to provide the needed seal. The protocol of the sealing is as follows:

1. All these procedures need to be operated in clean room.
2. Clean the sensor with acetone if there is any residue of photoresist on it.
3. Pre-bake the sensors at 80^{o}C for 10 minutes to remove any possible water or acetone on the sensor. Let the sensor cool down to room temperature.
4. Prepare the photoresist. Suck the photoresist into a syringe and install a 0.2 μm filter at the tip of the syringe so all photoresist coming out will have to pass through the filter. This will remove particles in the photoresist solution.
5. Apply a drop of photoresist onto the top edge of the sensor (the porcelain part).
6. Using a long and thin dispensing needle (also called blunt, 0.012"OD, 2" in length) installed onto a syringe, guide the photoresist into the reaction chamber. Control the amount of the photoresist entering into the chamber so that it will only form a thin layer around the edge and will not reach further onto the sensor membrane. Trying to guide the photoresist from different positions along the edge might help to achieve this. Observe the sensors under microscope after such treatment. If not satisfied, repeat from step 2.

7. Use Beta wipes to remove as much as possible the extra photoresist from the top edge of the S25.
8. Bake the sensor at 80 ^{o}C for 10 minutes to dry the photoresist.
9. Bake the sensor at 100 ^{o}C for 10 minutes.
10. Bake the sensor at 120 ^{o}C for 10 minutes to finish drying and partially crosslink the photoresist.
11. Let the sensor cool down to room temperature. Using acetone-moistened Beta wipes, carefully remove the remaining photoresist on the top edge of the sensor. The sensor should be clean on the top edge and the center of the sensor's membrane should be shiny clean. A nice and complete ring should be formed on the edge of the sensor's well.

Sensors after such treatment should be good for experimental use. Usually such treatment will sustain for only one use (sometimes they can be reused, but the cleaning after first use will usually break the seal). The safest method is to use the sensor once and clean it, and repeat the sealing treatment using photoresist before putting the same sensor to a second use.

General Procedure of Experiments

As we have finished with the details of our equipment and methods, we can now discuss the general procedures when we run an experiment.

First of all, we need to prepare all materials before the experiment. Sensors must be coated with photoresist. Glass pipettes should be pulled beforehand and silanized to acquire hydrophobicity. The syringes should be cleaned with DI water.

The data acquisition system should be ready for use. The pipettes must be calibrated before we start the experiment so we know how to do an injection of 50 nL cell solution or a 1 nL chemical solution.

The general procedures start with hooking up the data acquisition system. The sensor should be connected to the amplifier box. When we turn on the LabVIEW program we should be able to see the sensor's response when there is nothing on it. Once we make sure the data acquisition system is working we can start using a syringe with a long and thin dispensing needle to load the pipette that we use to do the base volume injection. In biological experiments that means loading the cell solution into the pipette for injections of cells and the solution that contains them. We then should prepare the cover glass-Mylar double layer and oil on the experimental stage. They should be put on the sensor to seal it once we have finished the base volume injection. The reason that we want to do the base volume injection before we seal the sensor is so we have a chance to redo the base volume injection if we find the sample is not in the ideal position after the injection. If we do not like the position of the sample, we could wash it off with DDI water without destroying the photoresist sealant in the sensor. No organic solvent, including isopropanol, should be used here for the protection of the photoresist sealant. Once we have a satisfactory base volume injection, we could then quickly put the cover glass-Mylar on top of the sensor and apply some oil to seal the assembly. As it will take some time for the liquid sample to evaporate and fill the whole reaction chamber with 100% moisture, the sensor's reading will be saturated for a while. If

the sealing is all good, the sensor's reading should return to the normal range within a couple minutes.

If we have a good reading on the sensor in the normal range (-5 V to 5 V on the LabVIEW program), we can then start inserting another pipette for injection of chemical/toxin. Load the pipette using a syringe with long/thin dispensing needle. Then guide the pipette tip through the double holes on the cover glass-Mylar cover by carefully operating the micromanipulator, while looking at it under the microscope. The pipette tip should go through the double holes and reach inside the reaction chamber. After the pipette tip is in the reaction chamber, put on the metal ring with slot (carefully let the pipette pass through the slot so the pipette's position is maintained). Put the rubber cover onto the microscope objective and lower the objective to the position where the sample can be clearly seen while the rubber is covering up the top of the metal ring.

Next move the pipette tip to a desired injection position (in touch with the base droplet but not too deep inside) and define that position as the "reach-in" position on micromanipulator controller. Then retract the pipette tip to a resting position (off the base droplet but inside the chamber). Test the one-button move on the micromanipulator to see if the pipette is moving between the desired positions. Please refer to the user manual of the Eppendorf Micromanipulator 5171 for detailed information on how to achieve these operations. Once this is set, we turn off the microscope light source, let the signal stabilize and start recording our data. When we need to do injections in the middle of the experiment, we just need to press one button on the micromanipulator to let the pipette tip move to the injection position,

then press Picospritzer to do the injection. Retract the pipette tip back to the resting position by pressing the button on micromanipulator controller again. This is necessary even though the pipette tips are silanized, it is still possible that they could cause some loss of liquid if they stay in contact with the droplet throughout the experiment, and they would also contribute to the heat leak from the sample.

The whole process of data recording can be monitored on LabVIEW's interface. Once we have finished recording the data, we close down the program and clean the sensor with both DDI water and isopropanol. The sensor most likely cannot be reused before coating with photoresist again. Dispose of the used pipette tips in the disposal for glass and sharp things. The data can then be processed using Matlab or another appropriate program.

CHAPTER IV

MODELING OF THE SENSOR

We have developed models for the S25 sensor to predict its performance under different situations, including experimental conditions. These models include a diffusion model to predict the diffusion of chemical substances in the droplet after injection, and a heat conduction model to predict the response of the sensor upon a heat generation or change of power. Both models use the finite element method and are implemented by computational programs written in Matlab. Now we will introduce these two models and their results with the details of the program scripts attached in Appendix D and E.

Chemical Diffusion Model

The purpose of the chemical diffusion model is to find out the time constant of the diffusion, *i.e.,* how much time does it take for the chemicals we injected to equilibrate in the base droplet. We can then compare this time to our sensor's response time, which is 12 ms given by the manufacturer and about 1.1 seconds under experimental conditions. This will give us an idea about how much time it takes for the chemical substance to dilute and diffuse to form an equal concentration throughout the droplet. If this time is significantly lower (or quicker) than our sensor's response time, it is then fair to consider the diffusion process as happening instantaneously so we only need to consider the thermal process of the reaction or

the biological thermal response. Otherwise, we will have to take into consideration the time for the substance to diffuse and our experimental results have to incorporate that aspect. The following two sections will introduce the model's methods and results.

Method of Diffusion Model

We start from the physical picture of the injection: a base volume droplet of about 50 nL sits on top of the senor membrane, then a droplet of 1nL chemical solution is injected to the center of this droplet. The base volume droplet is modeled in a hemispherical shape, which is not quite the case in reality, as water's contact angle on the membrane surface is ~77° based on our measurements. However, since our model's result later on has provided a time constant that is significantly (orders of magnitude) different from our sensor's time constant, the approximation here is totally acceptable. The hemispherical droplet is then modeled in a spherical coordinate system. The injection droplet is modeled as a small hemisphere showing up in the center of the base droplet. **Figure 27** shows how the base droplet and the injection droplet are modeled.

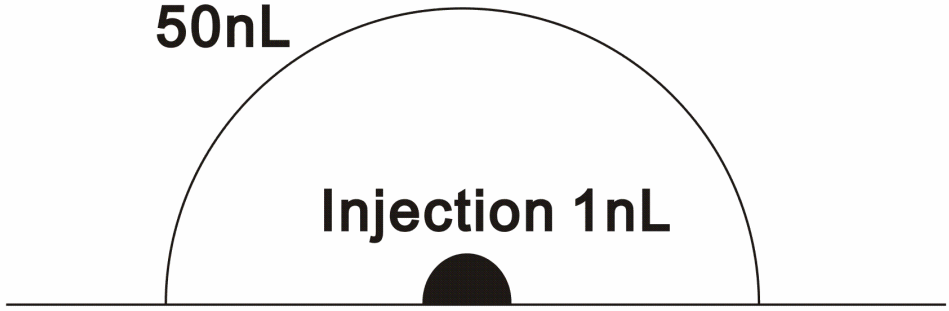

Figure 27. Illustration of the diffusion model.

In spherical coordinates, we apply the finite element method so the droplet (containing both volumes) is divided into 288 layers with each layer's thickness being 1 μm. This is because a 50 nL droplet's radius is 288 μm. The injection droplet contains a certain chemical with concentration *x*, which is the preset concentration of the injected liquid. In the program script in Appendix D, 0.01 mol/l is used because that is the concentration of the NaOH and H_2SO_4 solution injected in chemical calibration experiments. The program is based on Fick's law of diffusion:

$$\frac{\partial \phi}{\partial t} = D \frac{\partial^2 \phi}{\partial x^2} \tag{18}$$

In equation 10, *D* is the diffusion constant (or diffusion coefficient) and its unit is m^2/s. *D*'s value depends on the properties of the solution – the chemicals that are in the solution and the concentration of such chemicals. For our experiments, we used several types of chemicals, including 300 mM KCl, 0.01 M H_2SO_4, and 0.01 M NaOH. Their diffusion constants have similar values.[53] Their diffusion constants at the relative concentrations are shown in **Table 5**.

Table 5. Diffusion coefficients of some chemicals and ions at 25°C

Ion/substance	Diffusion Constant (at corresponding concentration)
KCl (300 mM)	$1.884X10^5 cm^2 sec^{-1}$
KCl (30 mM)	$1.863X10^5 cm^2 sec^{-1}$
Na^+ (Infinite dilution)	$1.35X10^5 cm^2 sec^{-1}$
OH^- (Infinite dilution)	$5.23X10^5 cm^2 sec^{-1}$
H^+ (Infinite dilution)	$9.34X10^5 cm^2 sec^{-1}$
SO_4^{2-} (Infinite dilution)	$1.08X10^5 cm^2 sec^{-1}$

We see in **Table 5** that the lowest diffusion coefficient is for SO_4^{2-}, which is about $1X10^5\ cm^2 sec^{-1}$. That is the value we used in our program so our diffusion time constant calculated from the program will be longer than any of the real diffusion constants for those chemical solutions. For NaOH and H_2SO_4, we used the diffusion coefficient of the individual ions. Due to the concentration we inject into the droplet (0.01 M), it is fair to say that the electrolytes are present in ionic form. For the infinitely dilute aqueous solution, the diffusion coefficient between that and the 0.01 M solution is usually very small. So it is also a fair approximation for us to use the diffusion coefficient of the infinitely dilute aqueous solution instead of the 0.01 M diffusion coefficient (we did not find the 0.01 M diffusion coefficient for the specific ions).

The concentration of each model element (which is a layer of the hemispherical droplet) is then calculated based on the diffusion equation for every time step. The program will progress until the concentration of the whole droplet is approximately identical everywhere. In our program, we chose the time step as $1x10^{-14}$ second and the whole computation was for 3 ns. These are the time steps required to obtain a converging result and the length of process necessary to be

computed. More annotations are made on the program script. The modeling results will be introduced below.

Results of Diffusion Model

Using the program and methods we introduced above, we found that the diffusion process for such an injection (1 nL droplet into the 50 nL base volume) and for such chemicals (0.3 M KCl, 0.01 M NaOH and 0.01 M H2SO4) is usually complete within 3 nanoseconds (ns) and the time constant of that diffusion in our small droplets is below 1 ns. **Figure 28** gives the results of our modeling by giving the concentration distribution of the chemical in the droplet at different times.

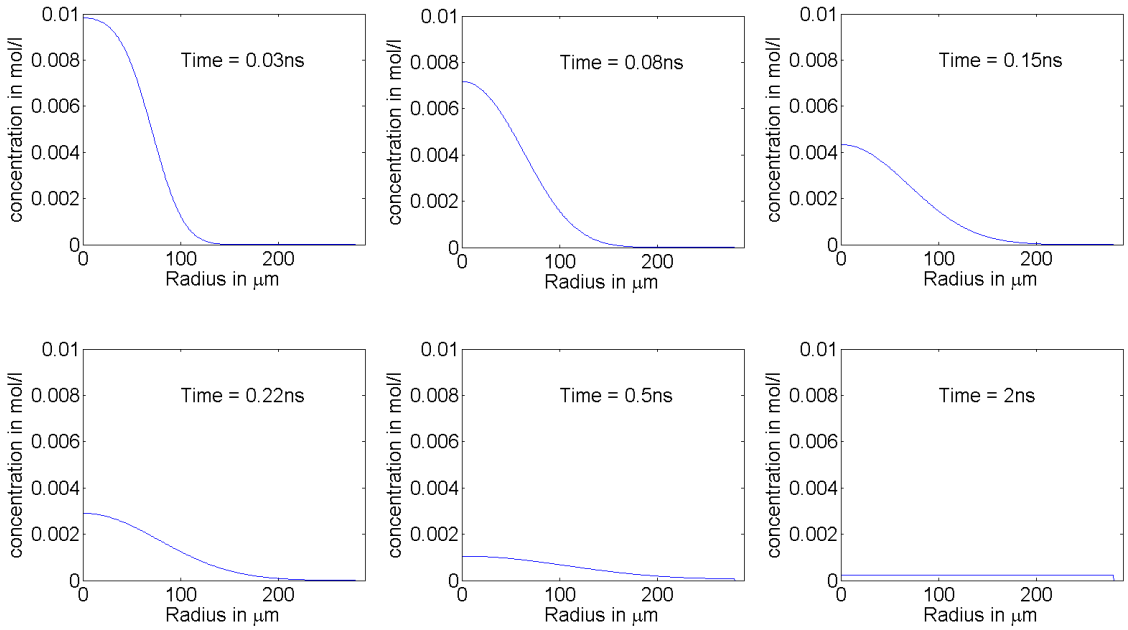

Figure 28. Diffusion model results. The six figures are showing the concentration distribution of the chemical at different locations of the hemispherical droplet (location marked in radius), in a time series from 0.03 ns up to 2 ns (where the concentration is almost even everywhere).

The time constant in diffusion is infinitesimal (<1 ns) compared to our sensor's response time, which is 12 ms as provided by the factory and about 1.1 s as measured in our experiments. So this takes virtually no time since our sensor will respond much slower than the time it takes for the chemical to diffuse and reach equilibrium. This is also significantly quicker than biological processes such as the response of a cell to a change in concentration.

The results of our diffusion model show that we could readily ignore the time it takes for the chemical to diffuse in the droplet. We could basically consider the droplet to contain the diluted solution right after the injection happens. We can now concentrate on the chemical and biological process happening after the injection.

Heat Conduction Model

We modeled our sensor's response to a thermal signal based on the fact that our sensor is a heat conduction calorimeter. Our S25 sensor consists of a thermopile which has 20 sensing junctions in the center of the membrane and 20 reference junctions buried under the heat sink. The purpose of the model is to model the actual situation on the sensor using the finite element method to see how much voltage the sensor will generate in response to a certain thermal signal. The model could deal with practically any kind of thermal signal. We actually modeled two situations: the response to a certain constant power, and the response to a sudden heat pulse (impulse response of the sensor). The power sensitivity could then be found out from the constant power modeling results and the impulse response could give us a time

constant to be compared with our experimental results. The method and the results of our model will be introduced separately below.

Method of Heat Conduction Model

The heat conduction model is purely based on the heat conduction equation:

$$\frac{\partial T}{\partial t} = \kappa \nabla^2 T \tag{19}$$

where T is the temperature, t is time and $\nabla^2 T$ is the Laplacian of the temperature distribution. This equation is in many ways similar to the diffusion equation, except that the diffusion constant D is switched to a thermal conductivity κ here. Now let's look at the physical picture of our model. See **Figure 29** for an illustration of the model.

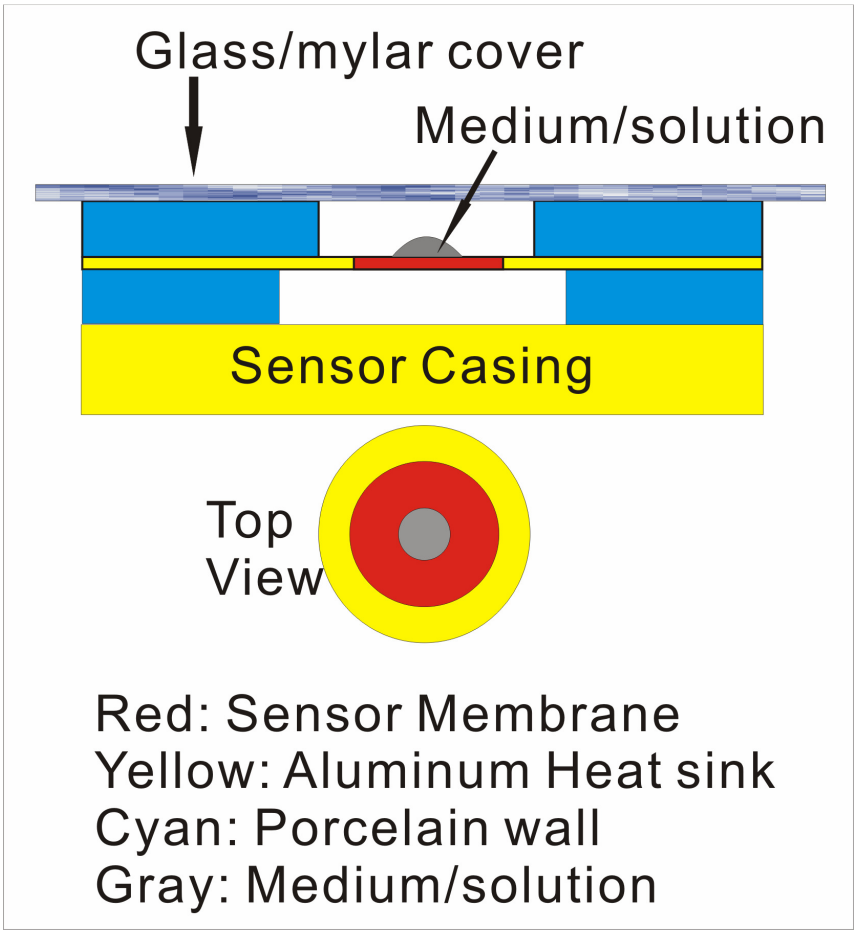

Figure 29. Illustration of the heat conduction model. The sensor's membrane is modeled as cylindrically symmetric, which is an approximation of the real membrane (the membrane stands alone in the square hole of the aluminum heat sink). All parts are deemed to be at constant temperature except the red part (silicon membrane) and the gray part (medium and solution).

We made an approximation in our model to make everything cylindrically symmetric. The membrane's silicon (silicon dioxide and silicon nitride) part is modeled as a round piece of membrane and the aluminum heat sink surrounding it has a round hole to accommodate the standing alone membrane. The true S25 sensor's aluminum heat sink has a square hole in the middle so that the membrane exposed is actually in a square shape. This approximation is necessary to make our

model computable within a reasonable amount of time. A real 3D model with the same accuracy will take months to compute a certain length of time at this precision that is useful for any conclusion. Even after our approximation here and the fact that our model is already a 2D (cylindrical symmetry applied) model, it still takes about 2 days to compute a 6 seconds long process with a 2.8 GHz CPU/1GB memory computer. On the other hand, the influence of such an approximation on the accuracy of our model is negligible. The heat flow pattern of the original sensor will of course be different from what we modeled here. But the modeled sensor's response will be very similar to reality since the exposed circular membrane's area in our model is about the same as the real S25's exposed square membrane. So this approximation greatly improved the efficiency of the computation of the model with little sacrifice in the accuracy of the computation.

We will be using more approximation and "guesses" in the model. One reason is that a lot of information on the sensor such as the exact composition of the membrane and the thickness of the membrane could not be acquired from the company who made it (Dexter deems this information as proprietary). The thickness of the membrane could be measured by the profilometer, as we have seen in **Figure 12**. The material of the membrane, however, could only be "guessed". We were told that the surface of the membrane is silicon dioxide (SiO_2). But based on the stiffness of the silicon dioxide, it is hard for us to believe the membrane is composed purely of that. As most of the current technology is using silicon nitride (Si_3N_4) as the membrane's supporting material, we could then fairly guess that beneath the silicon dioxide layer, there is a silicon nitride layer and the total thickness is 1.5 μm as

measured by the profilometer. In HYPRES's PicoCalorimeter, a 0.6 μm membrane was used. Here we made a guess that the 1.5 μm membrane consists of 0.5 μm silicon dioxide on top and 1.0 μm silicon nitride under it. The details of the dimension of our model are shown in **Figure 30**.

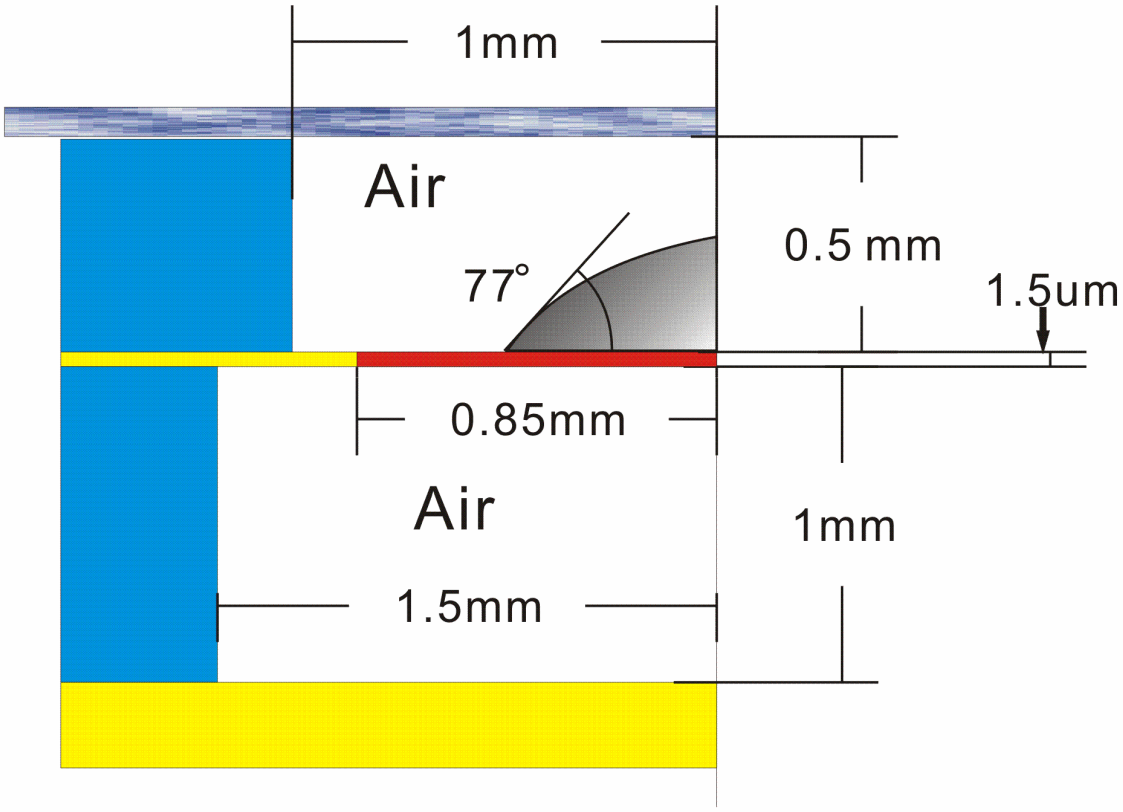

Figure 30. Details of the model's dimensions and geometric parameters. The membrane is 1.5 μm thick. The model includes both the air above the sensor's membrane and that below it. Cylindrical symmetry has been applied.

The model includes the membrane, droplet and the air above/below the membrane. All other parts, including the yellow colored heat sink, are maintained at constant temperature (environment temperature) in the model. A 2D finite element

model was implemented. The membrane itself is an 85X1 vector in the model. The air/medium above the membrane is a 100X50 matrix, while the air below the membrane is a 150X100 matrix. The medium's contact angle is defined as 77 degrees in the model. This comes from our measurement by injecting a certain volume of medium and observing the radius of the droplet to calculate the height and then deducting the contact angle of the medium on the glass. The literature[54,55] gives various contact angles for water on glass from 14 to 118 degrees.

A number of physical/thermal parameters must be specified in the model, including the thermal conductivity and thermal capacity of all materials used here. We list the physical/thermal parameters[56,57] used in the model in **Table 6**.

Table 6. Physical/thermal parameters of all materials involved in the model.

Material	Heat conductivity (W/m/K)	Heat Capacity (J/g/K)	Density (g/L)	Heat capacity by volume (J/L/K)
Si_3N_4	30	7.106	3290	2160
SiO_2	1.3	7.530	2200	3423
Water	0.61	4.184	1000	4184
Oil	0.13	1.966	830	1579
Membrane	20.4	N/A	N/A	2581
Air	0.025	1.030	1.29	1.33

The details of the membrane's composition, as we said before, is unknown for us. As we guessed the membrane contains 0.5 μm silicon dioxide on top of 1.0 μm of silicon nitride, we make the membrane's property a mixture of these two materials. So the heat conductivity and the heat capacity of the membrane are expressed as 2/3 of the silicon nitride's property plus 1/3 of the silicon dioxide's property, correspondingly.

The program is then run stepwise. The biggest time step for us to get converging results is 0.2 μs. This model could help us find out the difference between oil covering the sample and the sample is sitting alone in the reaction chamber. We will show this result together with other modeling results in the following section.

Results of Heat Conduction Model

We have run our modeling to solve for two situations. One is to have constant power injected onto the sensor and the other is to have a pulse of heat production onto the base droplet (to model impulse response, such as when we inject chemical solutions). The results of these two situations are discussed below.

The impulse response is investigated as follows: setting everything at rest to start with, and then raising the temperature of a 1nL region at the top of the 50 nL droplet (a 5X10 element block in our model) to 0.16 K (which is the temperature rise based on the experimental heat of reaction and the heat capacity of that element block). The response of the sensor will be predicted based on that input. See **Figure 31** for the result of impulse response.

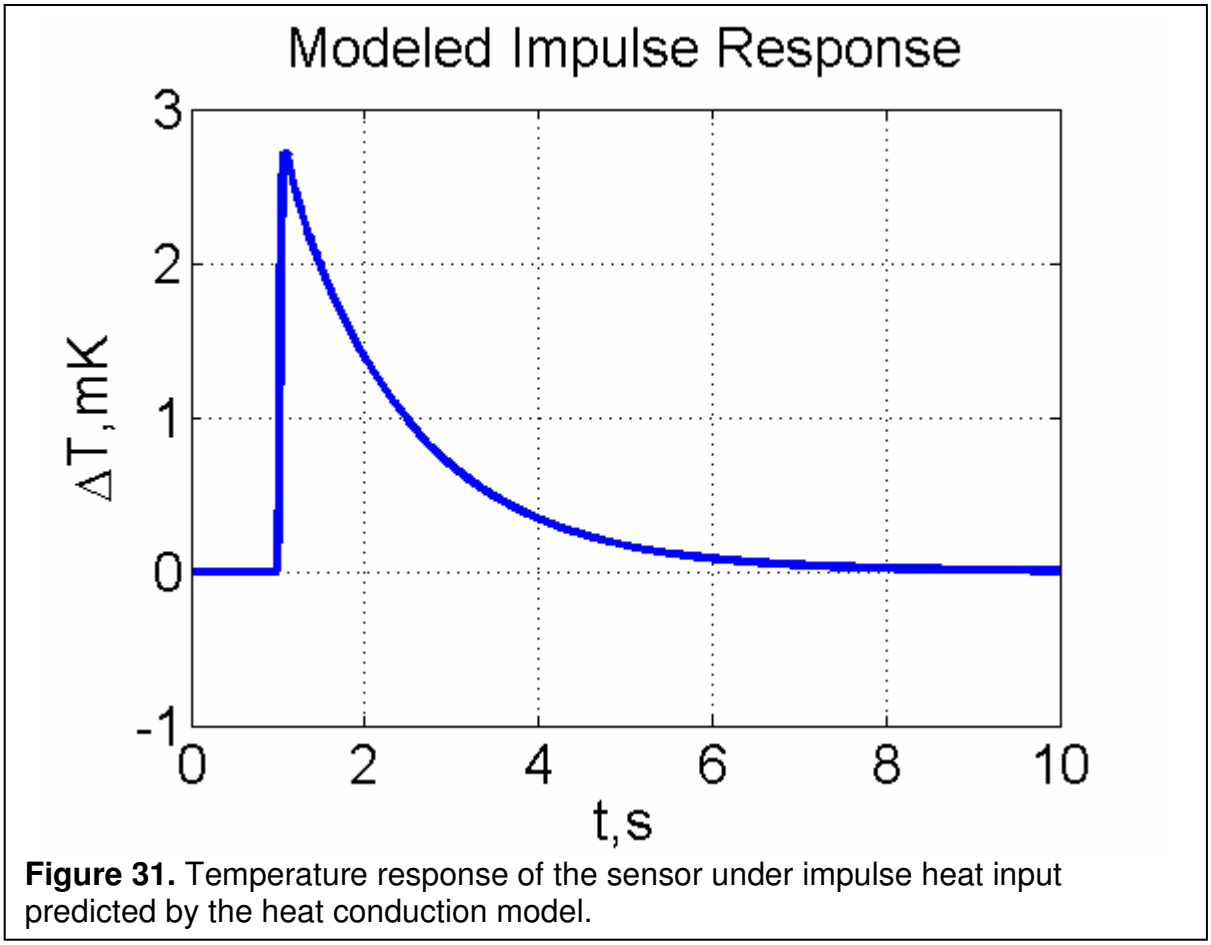

Figure 31. Temperature response of the sensor under impulse heat input predicted by the heat conduction model.

The impulse response given here would be compared to our experimental results in Chapter V, Calibration of the Sensor Using Chemical Methods. The time constant is not traditionally defined in such an impulse response. But let us just define the time constant here as the time it takes for the sensor's response level to drop from the peak point to 36.8% (1/e) of the peak response (~1mK in **Figure 31**). With this definition, our time constant of the impulse response is about 1.37 seconds. This result will prove to very close to our experimental result later in Chapter V.

The more important result we could get from our model is our sensor's response under constant power. Theoretically this should be an exponential rising curve in the form of

$$T = T_0 \cdot (1 - e^{-t/\tau}) \tag{20}$$

where τ is the time constant of the sensor. Under constant power, the temperature of the sensor's sensing junctions would rise up from zero and finally reach a fixed value (steady state), and so will the sensor's voltage response which is related to the temperature difference between the sensing junctions and the reference junctions (where the temperature is considered to be fixed) by the Seebeck coefficient of the sensor. This steady state voltage (or temperature difference) could then be used to predict the sensor's power sensitivity (in V/W). This sensitivity, however, as we mentioned before, is highly related to the experimental condition of the sensor, including whether there is sample on the membrane and how much sample is there. Time constant τ which could be calculated from the modeling results as the temperature difference, will be at 63.2% of the final steady state value when time is equal to τ. We have computed the model for several situations: when there is no sample on the sensor, free membrane; when there is a 5 nL sample on the sensor; when there is a 50 nL sample on the sensor; and when there is a 50 nL sample and the well in the sensor is covered fully by mineral oil. See **Figure 32** for our modeling results on constant power. The power is constant 1 μW for all situations. The modeled power sensitivities and the time constant of the sensor at different conditions are shown in **Table 7**.

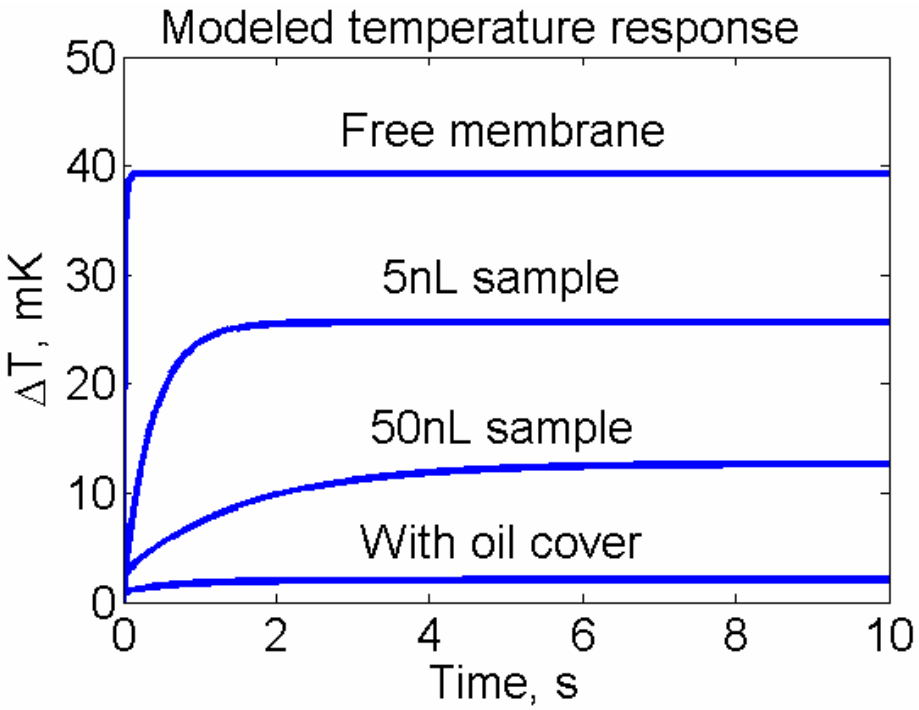

Figure 32. Temperature response of the sensor under constant power predicted by the model. Four situations were modeled here: when the sensor membrane is free of sample; when there is a 5 nL aqueous sample; when there is a 50 nL aqueous sample; when there is a 50 nL aqueous sample and the sample is covered by mineral oil.

Table 7. Power sensitivities and time constants predicted by the heat conduction model.

Situation	Power sensitivity (V/W)	Time constant (s)
Free Membrane	9.43	0.009
5nL Sample	6.15	0.37
50nL Sample	3.05	1.23
50nL Sample oil covered	0.48	0.26

The results have shown that the power sensitivity of the sensor will decrease greatly with samples added onto it, especially if there is an oil cover over the sample. That is why we shall avoid using an oil cover to achieve evaporation prevention – the sensor will have only 1/20 of the original sensitivity when an oil cover is present. The

time constant of the sensor also increases as sample volume increases. However, the oil cover has made the time constant much less because of the thermal conductivity it adds onto the sensor. The overall results have shown that oil cover should not be used and our sample volume should be as small as possible to achieve better sensitivity. Due to our injection system, it is very hard to accurately inject sample volume below 50 nL if cell solutions are to be injected, because the cells' size sets a limit on the pipette opening size. Thus, 50 nL is the standard we use in both our cell experiments and our calibration experiments. The model predicted the power sensitivity when a 50 nL sample is present as 3.05 V/W, which is within 5% of our experimental results of 2.91 V/W, as will be introduced in the following Chapter V, Ccalibration of the Sensor Using Chemical Methods.

CHAPTER V

CALIBRATION OF THE SENSOR USING CHEMICAL METHODS

Abstract

A new nanocalorimeter having nW sensitivity is achieved through modifications to a microfabricated commercial infrared sensor. Reactions are studied by placing a droplet (~50 nl) of one reagent directly on the sensor and injecting nl droplets of a second reagent through a micropipette by means of a pressure-driven droplet injector. Evaporation is prevented by positioning the micropipette through a tiny hole in a cover glass, sealed by a drop of oil. The device is calibrated using two acid-base reactions: H_2SO_4 + HEPES buffer, and NaOH + HCl. The measured power sensitivity is 2.91 ± 0.26 V/W, giving a detection limit of 22.1 nW. The 1/e time constant for a single injection is 1.1 s. A computational model of the sensor reproduces the power sensitivity within 10% and the time constant within 20%.

Introduction

Microcalorimetry is widely used to measure enthalpy changes in chemical reactions, biochemical processes, and phase transitions, with typical detection limits of μW or μJ.[1-4] In the last decade, micromachining techniques[5,6] have been used to produce calorimetric devices with greatly reduced sample volumes and nW sensitivity.[7-9] These nanocalorimeters possess such high sensitivity that they work at essentially constant temperature and hence qualify as isothermal calorimeters.[10]

Some of these devices are designed with microfluidic channels,[11] while others are flow-through types built on microfabricated silicon chips.[12-15] Electrical calibration is routinely used for both microcalorimeters and for this recent generation of nanocalorimeters,[16] primarily because it is convenient and more precise than the calorimetric signal with which it is compared.[17] Sometimes, however, the heat from an electrical heater is not representative of the heat involved in the process being studied, so it is desirable to use calibration procedures that more closely replicate the conditions of the experiments. For this purpose, a number of standardization processes have been employed.[10,17-19]

Here we describe a microfabricated commercial thermopile IR sensor (S25 from Dexter Research), which we have modified into a nanocalorimeter suitable for biological and chemical calorimetric measurements. The S25 is a thin membrane, silicon-based thermopile sensor, with sensing junctions at the center of the membrane. In our experimental configuration, a 50-nL droplet is placed at the center of the membrane (the sensitive area), and sub-nL droplets are injected into this droplet through a micropipette by a pressure-driven droplet injector (PicoSpritzer II, Parker Hannifin). The power sensitivity of the device is calibrated using two chemical reactions: 0.01 M H_2SO_4 with 0.2 M 7.5 pH Hepes buffer, and 0.01 M NaOH with 1M HCl. These experiments yield a calibrated power sensitivity of 2.91 ± 0.26 V/W. For its response time of ~1 s, the detection noise is 21 nV, which translates into a detection limit (three standard deviations above background) of 22.1 nW. This is on the same level as the previous best result of 13 nW.[9] A computational model designed to simulate the response of the sensor to chemical reactions in a 50-nL

drop predicts a sensitivity of 3.05 V/W, in good agreement with the experimental results.

Experimental Section

Implementation of the Calorimeter

The S25 silicon-based thermopile sensor (Dexter Research Center Inc., Dexter, MI) is shown in **Figure 11**. It has a 20-junction thermopile with a Seebeck coefficient of 24 μV/K per junction. The thermopile is built under a thin (~1.5 μm) membrane of SiO_2/Si_3N_4. The metal tracks for the thermopile are directly underneath the membrane, and the sensing junctions are clustered at the center. Surrounding the freestanding membrane (the square view in **Figure 11D**) is the aluminum heat sink that is attached to the porcelain body of the S25 sensor. The 0.5 mm well is formed by the membrane/heat sink at the bottom and the porcelain body of the sensor surrounding it. This well is modified to serve as our reaction chamber. At the S25's nanowatt sensitivity, the detected temperature changes are usually at the mK level, qualifying this device as a heat-conduction isothermal nanocalorimeter.[10]

The voltage generated by the S25 sensor is detected using an amplifier with 100K gain, then recorded by a PCI-6024E data acquisition board (National Instruments) in the computer. A LabVIEW interface is used to control the experiment and display the readings.

Electrical Noise Charactertization

The S25 has an intrinsic noise voltage of 19.4 nV/√Hz, and our amplifier adds noise to the output. We use a low-noise instrumentation amplifier and chopper-stabilized operational amplifier to minimize the Johnson and 1/*f* noise. In addition, the body of the amplifier box and the cables used for signal transmission are shielded to avoid interference from external electrical noise. The resulting output noise of the calorimetric system is shown in **Figure 13**. A low-pass filter with 10 Hz cutoff frequency was used in this measurement, so the noise voltage density towards the 10 Hz end is reduced even below the sensor's original noise voltage. At 1 Hz, the system produces 20 nV/√Hz noise voltage density, which is only slightly above the sensor's intrinsic noise. This is a direct result of our low-noise amplifier and the electrical shielding. In the experiments, however, a 1-Hz low-pass filter was used instead of the 10-Hz one, giving a slightly elevated total noise of 21.4 nV.

Thermal Shielding and Evaporation Prevention

All experiments were conducted at ambient room temperature (~23℃), without active temperature control. However, the system was isolated thermally from the environment by a double layer shielding system. Such insulation was important, because for the ~μJ reactions heat involved here, the measured temperature differences were ≲ 10 mK. The system also had to be evaporation-free, since sample evaporation can produce a large, time-dependent signal.[16] Calorimetric experiments on such small volumes without evaporation protection have been done by Neugebauer, *et al.*;[20] however, their method cannot be used to study biological

processes, which is a major goal of our system. In addition, a method for delivering reactant liquid must be included in the design of the system. For these reasons, we built an integrated system for thermal shielding, evaporation control and sample delivery, illustrated in **Figure 26**.

The outer shield (**Figure 26A**) incorporates the sensor's body and the microscope objective and consists of a lateral thermal shield made of copper on the side and a lid attached to the microscope objective. The thermal shield rests on the upper surface of the amplifier box, and the sensor is inserted into a socket mounted on top of the box. When the objective is lowered for observation, the lid firmly closes the open upper end of the lateral shield and thus seals the sensor compartment. The inner thermal shield is created by the cover over the S25 sensor, which together with the sensor well, forms the reaction chamber (**Figure 26B**). This cover is a thin Mylar sheet attached to a cover glass. The cover glass-Mylar combination must shield the sensor from external thermal noise and prevent evaporation, while still allowing access via the micropipette for reagent injection. These goals are accomplished by means of holes in the cover assembly (0.6-mm diameter in the cover glass and a concentric 100-µm hole in the Mylar), which are effectively sealed by a small drop of mineral oil on top of the assembly. Surface tension prevents the oil from leaking into the reaction chamber.

Sub-nanoliter Sample Delivery

Liquid reactant is delivered by electrically controlled pressure pulses from a commercial droplet injector (PicoSpritzer II, Parker Hannifin) in conjunction with

micropipettes pulled from 2-mm OD / 1.12-mm ID glass capillaries. **Figure 25** illustrates the injection process. The micropipette is controlled by a micromanipulator (5171, Eppendorf). Initially, the micropipette is away from the sensor membrane and is then pushed onto the surface of the membrane, where the injection is made. The micropipette is then retracted to its original position.

The calibration experiments employed ~50 nL droplets placed at the center of the membrane, with subsequent titration injections of 0.5-1.5 nL. The latter were done using micropipettes having a tip opening of 2-4 µm, together with appropriate pressure (~30 PSI) and pulse duration of the PicoSpritzer. Small-volume titrant injections were necessary to ensure that the heat of reaction remained constant for a series of 10 injections. The titrant injection volume was determined by measuring the total volume dispensed over a large number (~10^4) of such injections. This volume was calculated from the inner diameter of the glass capillary (measured under a microscope), and the length of liquid dispensed (measured with a caliper). The variation in droplet volume could not be determined directly, but has been demonstrated to be less than 3% under similar circumstances.[21]

Calibration Experiments

Most of the calibration experiments employed 0.01 M H_2SO_4 injected into 0.2 M pH 7.5 HEPES solution ($\Delta H°$ = –53.4 kJ/mol H_2SO_4 at 23°C)[17]. The acid solution was prepared by dilution of 98% acid (Fisher) and was standardized by titration. The HEPES buffer was made from powder (Sigma-Aldrich), and its pH was adjusted to 7.5 by adding KOH. The solution was stored at 4°C. Ten constant-volume injections

were made in a single experiment, with injection volumes in the range 0.64-1.54 nl. The total injected volume for each experiment was thus small enough to ensure that the heat generation was constant for all injections.[17]

Some experiments were also done with 0.01 M NaOH injected into 1M HCl solution. The NaOH solution was standardized by titration with KHP, and the HCl was prepared by diluting 37% acid (Fisher). For the neutralization of NaOH with HCl, the heat of reaction at 25° C is –55.84 kJ/mol at infinite dilution; correction for finite concentrations and conversion to 23°C give –58.2 kJ/mol.

Results and Discussion

Modeling the Calorimeter

The calorimeter was modeled using a finite element method treatment of the heat diffusion equation. The sensor and the sample were approximated as a cylindrically symmetric system and thus modeled in cylindrical coordinates. **Figure 30** provides details of the geometry for modeling. The heat diffusion equation in cylindrical coordinates is

$$\frac{\partial}{\partial r}\left(k\frac{\partial T}{\partial r}\right)+\frac{\partial}{\partial \theta}\left(\frac{k}{r^2}\frac{\partial T}{\partial \theta}\right)+\frac{\partial}{\partial z}\left(k\frac{\partial T}{\partial z}\right)+S=\rho C_p\frac{dT}{dt} \qquad (21)$$

where k is the thermal conductivity, S is the heat source power density, ρ is the density and C_P the heat capacity. All parameters are based on the specific materials and the geometry as explained in **Figure 30**. We do not know the exact composition of the membrane due to proprietary issues, so we treated it as a combination of 500 nm silicon dioxide and 1000 nm of silicon nitride, based on the common structure of

such sensors and the limited information provided by the Dexter Inc. The model was applied for two situations: for constant power supplied to the sensor and for an impulse of heat transferred onto the sensor.

The results of the constant power simulations for four different configurations are shown in **Figure 32**. The depicted sensor temperature at the sensing junctions is linearly related to the sensor's voltage response by the Seebeck coefficient. It is clear that the added sample reduces the sensor's response due to the additional thermal conductance it brings to the thin membrane. This is especially obvious when there is an oil cover, which shorts the thermal conducting path from the sensing junctions to the reference junctions. The time constant of the sensor was also increased by added sample due to the additional thermal mass. The modeled power sensitivity and time constant for the four configurations are listed in **Table 7**. The model for impulse heat input will be presented later in comparison with our calibration experimental data.

Calibrated Power Sensitivity

Figure 33 shows results obtained from one calibration experiment. Ten injections were made in the experiment, each with an estimated 0.651 nL injection volume and expected 0.355 μJ heat production. Using the titration experiment results, we could then integrate the signal and use the heat production per shot to calculate the power sensitivity of the nanocalorimeter. **Figure 33B** shows a calibrated sensitivity of 2.94 ± 0.37 V/W. Different volume of titrant injections were used in other

experiments using the same sensor and protocol. The results of such experiments are shown in **Table 8**. An average power sensitivity of 2.91 ± 0.26 V/W was obtained from those experiment results. Similar results were produced in the experiments using NaOH reacting with HCl. The major reason for the deviation in calculated power sensitivity is the uncertainty in integration of the signal caused by the noise of the calorimetric system. This is demonstrated by the fact that when the titrant injection volume is increased (which means the heat produced per shot is increased), the uncertainty in calibrated power sensitivity goes down. When our injection volume is 1.54 nL, the error is only 3.1%, compared to 12% error when the injection volume is 0.651 nL. Given the same amount of noise, it makes sense that when the total integration area is reduced, the uncertainty in integration caused by noise will increase accordingly.

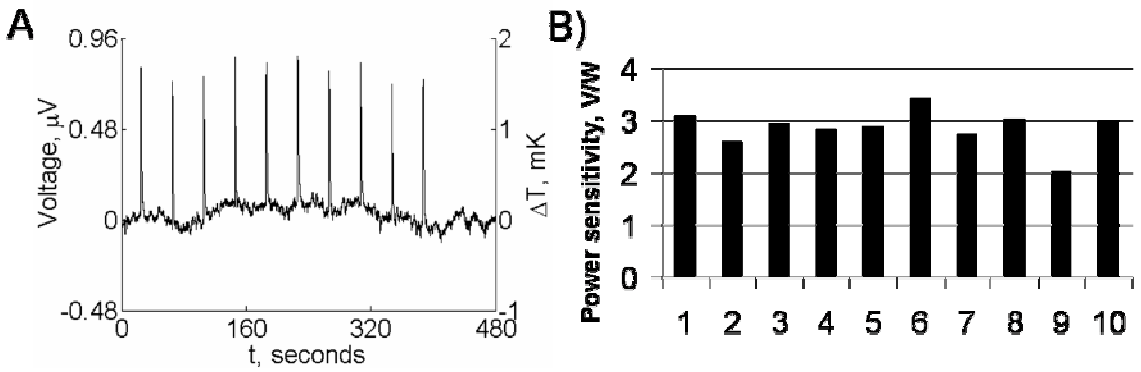

Figure 33. Calibrated power sensitivity. A) Thermal response of the nanocalorimeter from the injection of 0.01 M H_2SO_4 into 0.2 M 7.5 pH HEPES. The HEPES volume is 50 nl, and each injected droplet is estimated to be 0.651 nl, giving a heat production of 0.346 µJ. B) Power sensitivity (in V/W) calibrated from individual shots, assuming every shot produced 0.346 µJ of heat. The mean of the calibrated power sensitivity is 2.94 V/W, with a standard deviation of 0.37 V/W.

Table 8. Results of HEPES experiments with different titrant injection volumes

Titration volume (nL)	Heat per injection (μJ)	Calibrated power sensitivity (V/W)	Uncertainty of power sensitivity (V/W)
0.651	0.355	2.86	0.36
0.679	0.369	2.82	0.34
0.982	0.533	2.86	0.15
1.54	0.836	2.82	0.09

Modeled Impulse Response

In our experiments, the sensor's thermal response to a single injection could be deemed to be its response to an impulse of heat because the time required for diffusion and chemical reaction (~ns) is far less than the time constant of the nanocalorimeter, which is around 1 second when there is a 50 nL sample. The experimental result of the nanocalorimeter's response to a single injection is presented in **Figure 34A**. A time constant is not traditionally defined for an impulse response, but if we define a time constant τ here as the time it takes for the response to fall from its peak value to 36.8% of the peak value, we then have a time constant of 1.1 s from our experimental results. As introduced before, we could also model the impulse response by raising the temperature of the injected droplet to a certain temperature based on the heat produced by the reaction and the injected droplet's size. The response of the sensor will then be predicted based on that impulse of heat input. The result of the modeled impulse response of the nanocalorimeter is shown in **Figure 34B**, where the amount of heat introduced is the same as the experimental result in **Figure 34A**. With the same definition of the time constant as in the single injection experiment, the modeled impulse response has a time constant of 1.3 s, which is reasonably close to our experimental time constant

of 1.1 s. The comparison between our modeled impulse response and the experimental result of a single injection shows that the sensor's response to an impulse heat input nicely modeled its response to a single injection.

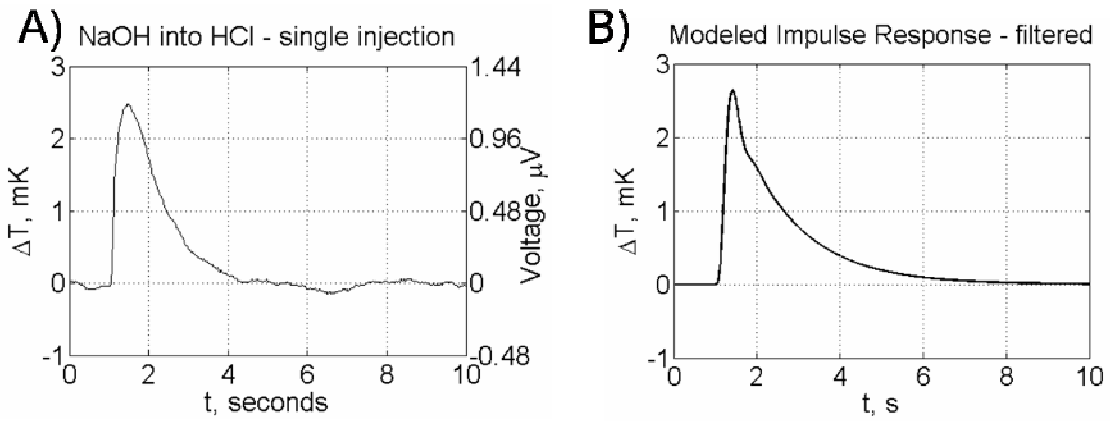

Figure 34. Nanocalorimeter response to a single shot in experiment compared to modeled impulse response. A) Experimental nanocalorimeter response when 1.18nL of 0.01 M NaOH is injected into 1 M HCl. B) Temperature response of nanocalorimeter to a 0.67 μJ impulse heat production computed by the finite element model, after filtered by a digital low-pass filter with 1 Hz cutoff frequency.

Conclusions

We have demonstrated the ability to calibrate a nanocalorimeter sensor using chemical methods. The calibrated power sensitivity is 2.91 ± 0.26 V/W, and the sensor demonstrated a power resolution of 22.1 nW, close to the previously reported 13 nW[8]. The experimental results are in agreement with the modeled result of 3.05 V/W, and the modeled impulse response for a single injection is consistent with our experimental results.

Our research has demonstrated a microfabricated sensor with power sensitivity and power resolution similar to the best existing nanocalorimeters used

for chemical and biological measurements. The calibration of the sensor using chemical reactions closely simulates the true experimental conditions when the sensor is being used for calorimetric measurements on chemical or biological processes. This calibration method has provided a more accurate way to calibrate such thin film sensors when bulk amount of samples are involved.

Acknowledgements

This work has been supported in part by NIH Grant U01AI061223 and by the Vanderbilt Institute for Integrative Biosystems Research and Education. We are especially indebted to Dr. Eduardo Lima's invaluable help in developing the instrument and methods.

References for Chapter V

1. Wadsö, I, Isothermal microcalorimetry in applied biology, Thermochim. Acta. 2002, 394, 305-311.

2. Wadsö, I, Isothermal microcalorimetry current problems and prospects, J. Therm. Anal. Calorim. 2001, 64, 75-84.

3. Murphy, KP, Freire, E, Thermodynamics of structural stability and cooperative folding behavior in proteins, Adv. Protein Chem. 1992, 43, 313-361.

4. Wadsö, I, Isothermal microcalorimetry for the characterization of interactions between drugs and biological materials, Thermochim. Acta. 1995, 267, 45-59.

5. Lai, SL, Guo, JY, Petrova, V, Ramanath, G, Allen, LH, Size-dependent melting properties of small tin particles: nanocalorimetric measurements, Phys. Rev. Lett. 1996, 77, 99-102.

6. Denlinger, DW, Abarra, EN, Allen, K, Rooney, PW, Messer, MT, Watson, SK, Hellman, F, Thin film microcalorimeter for heat capacity measurements from 1.5 to 800 K, Rev. Sci. Instrum. 1994, 65,946-959.

7. Johannessen, EA, Weaver, JMR, Cobbold, PH, Cooper, JM, Heat conduction calorimeter for pl-scale single cell measurements, Appl. Phys. Lett. 2002, 80, 2029-2031.

8. Johannessen, EA, Weaver, JMR, Cobbold, PH, Cooper, JM, A suspended membrane nanocalorimeter for ultralow volume bioanalysis, IEEE Trans. NanoBiosci. 2002, 1, 29-36.

9. Johannessen, EA, Weaver, JMR, Bourova, L, Svoboda, P, Cobbold, PH, Cooper, JM, Micromachined nanocalorimetric sensor for ultra-low-volume cell-based assays, Anal. Chem. 2002, 74, 2190-2197.

10. Wadsö, I, Goldberg, RN, Standards in isothermal microcalorimetry, Pure Appl. Chem. 2001, 73, 1625-1639.

11. Zhang, Y, Tadigadapa, S, Calorimetric biosensors with integrated microfluidic channels, Biosen. & Bioelectro. 2004, 19, 1733-1743.

12. Lerchner, J, Wolf, A, Wolf, G, Recent developments in integrated circuit calorimetry, J. of Therm. Anal. and Calorim. 1999, 57, 241-251.

13. Lerchner, J, Wolf, A, Huttl, R, Wolf, G, Direct monitoring of biochemical processes using micro-structured heat power detectors, Chem. Eng. J. 2004, 101, 187-194.

14. Baier, V, Fodisch, R, Ihring, A, Kessler, E, Lerchner, J, Wolf, G, Kohler, JM, Nietzsch, M, Krugel, M, Highly sensitive thermopile heat power sensor for micro-fluid calorimetry of biochemical processes, Sens. and Actu. A. 2005, 123, 354-359.

15. Maskow, T, Lerchner, J, Peitzsch, M, Harms, H, Wolf, G, Chip calorimetry for the monitoring of whole cell biotransformation, J. of Biotech. 2006, 122, 431-442.

16. Chancellor, EB, Wikswo, JP, Baudenbacher, F, Radparvar, M, Osterman, D, Heat conduction calorimeter for massively parallel high throughput measurements with picoliter sample volumes, Appl. Phys. Lett. 2004, 85, 2408-2410.

17. Briggner, LE, Wadsö, I, Test and calibration processes for microcalorimeters, with special reference to heat conduction instruments used with aqueous systems, J. of Biochem. And BioPhys. Meth. 1991, 22, 101-118.

18. Wadsö, I, Needs for standards in isothermal microcalorimetry, Thermochim. Acta. 2000, 347, 73-77.

19. Tellinghuisen, J, Calibration in isothermal titration calorimetry: Heat and cell volume from heat of dilution of NaCl(aq), Anal. Biochem. 2007, 360, 47-55.

20. Neugebauer, S, Evans, SR, Aguilar, ZP, Mosbach, M, Fritsch, I, Schuhmann, W, Analysis in ultrasmall volumes: microdispensing of picoliter droplets and analysis without protection from evaporation, Anal. Chem. 2004, 76, 458-463.

21. Palmer, MR, Wuerthele, SM, Hoffer, BJ, Physical and physiological characteristics of micropressure ejection of drugs from multibarreled pipettes, Neuropharm. 1980, 19, 931-938.

CHAPTER VI

BIOLOGICAL MEASUREMENTS USING CARDIAC CELLS

Abstract

Biological processes involving cellular heat production are usually studied with microcalorimeters that make thermal measurements on hundreds or thousands of cells. We present here a microfabricated nanocalorimeter with a power resolution of 22 nW. The excellent sensitivity of this nanocalorimeter enables us to measure the suddenly increased power generation (100-300 nW) of 10 to 30 mouse cardiomyocytes in response to exposure to a high concentration of potassium. A significant increase in power generation (200-600 nW) is observed for cells under the influence of isoproterenol, a derivative of noradrenaline. This heat production is believed to come largely from the mechanical activities of the myocytes after the injection of high-potassium solution, as it is reduced by 90-95% when an excitation-contraction decoupler (2,3-BDM) is added to the cells. Direct observation of the electrical and mechanical activity and intracellular calcium level of single myocytes under the same protocol supported our interpretation of the thermal measurements.

Introduction

Macroscale cell-based calorimetric experiments[1-5] have been conducted previously to study heat generation and consumption in living cells, including heat generation by muscle,[2] nerve,[3,4] and large populations of isolated mammalian cells.[5]

Such calorimetric measurements provided a generic method to study cell metabolism in response to agonists or antagonists without a specific knowledge of the drugs' functions. Using thermal imaging[6] or microcalorimetry, quantitative measurements on cellular heat production have studied microbial populations[1,7] and cultured or isolated mammalian cells[8-15] under the influence of various drugs and hormones. In such microcalorimetric measurements, the cellular thermal power ranges from 2 pW to 1.7 nW, depending upon the cells and conditions.

Much research has been done on the change of metabolism of muscle cells or tissues (including skeletal and cardiac muscle) under the influence of high-concentration extracellular potassium. Solandt found a sustained elevated metabolism rate for the frog's sartorius muscle when the extracellular potassium concentration is 8-10 times above normal.[16] Hill and Howarth further determined that this increased metabolism rate is not associated with any mechanical changes in the muscle.[17] While this long-term increase in metabolic rate seems to be most evident in the frog's skeletal muscle,[18] Even et al. found an elevated extracellular potassium concentration could produce a biophasic increase in the metabolism of mouse soleus muscle, with an initial peak followed by a plateau, where the increased metabolism is closely related to the sarcoplasmic reticulum Ca^{2+} and could be inhibited by 2,3-BDM.[19] As the metabolic heat and work must be interpreted in terms of the major ATPase that supports cardiac contraction,[20] including Ca^{2+} and Na^{+}-K^{+} transport ATPase and actomyosin ATPase, further studies were done on the specific mechanism of this increased metabolic rate under the influence of high extracellular potassium.[21-23] In those studies, isolated cardiomyocytes in suspension[23] containing

high K^+, or cardiac muscles perfused[21,22] with high K^+ solution, were measured for heat output. The results showed that the ionic exchange mechanisms, including both Na^+-K^+ and Na^+-Ca^{2+} pumps, contributed greatly to the increased heat rate. The detail of the mechanism for such increase in metabolic rate, however, is not clear yet.

Microfabrication techniques developed in recent years have enabled researchers to make smaller, micromachined calorimeters[24,25] that can achieve a sensitivity of nW or even higher[26-28] and are thus called nanocalorimeters. Given their high sensitivity, these sensors operate under essentially constant temperature and typically operate as isothermal calorimeters.[29] Some have microfluidic channels built in them,[30] and some are flow-through calorimeters fabricated on IC chips.[31-34]

We have modified a microfabricated silicon-based thin-film thermopile sensor (S25 sensor, Dexter Research, Dexter, MI) to create a nanocalorimeter with an exceedingly good power detection limit of 22 nW[35] (**Figure 11**). Thermal measurements on 10-30 isolated mouse cardiomyocytes were made using this nanocalorimeter, which is also described elsewhere[35]. This new technique allowed us to perform calorimetric experiments using a small number of cardiomyocytes instead of a piece of muscle tissue or a suspension of millions of cells. High-concentration potassium was injected to stimulate the cells' metabolism, and the thermal response to the injections was observed. Significant increases in power generation (100-300 nW) were observed immediately after the injection of the high-concentration potassium. Even greater increases were observed when 100 μM isoproterenol was present in the medium. We believe that this increase in cellular power is related to the mechanical activities of the cardiomyocytes, as 50 mM 2,3-

BDM diminished the total heat generation after the stimulation by 95%. In addition to our thermal measurements, we performed single cell measurement to record the intracellular calcium concentration and sacromere length, which indicated that a tremoring mechanism associated with local calcium waves contributed greatly to the increased metabolic rate.

Materials and Methods

Reagents

Glucose, HEPES, bovine serum albumin (BSA), KCl, and 2,3-butanedione monoxime were purchased from Sigma Aldrich. Isoproterenol was purchased from MP Biomedical. NaOH, NaCl, $NaH_2PO4{\cdot}H_2O$, $MgCl_2{\cdot}6H_2O$, glucose, $NaHCO_3$, and $CaCl_2$ were purchased from Fisher Scientific. 2 mm OD glass capillaries were purchased from World Precision Instruments. 300 mM KCl solution was prepared from KCl powder and DDI water.

Cardiomyocytes

Isolated cells were obtained from adult mouse left ventricles in accordance with a Vanderbilt-approved animal protocol. The cells were maintained in base Tyrode's solution containing 130 mM NaCl, 10 mM HEPES, 4.5 mM KCl, 0.4 mM $NaH_2PO_4{\cdot}H2O$, 0.5 mM $MgCl_2{\cdot}6H_2O$, 10 mM glucose, and 10 mM $NaHCO_3$ with a pH value of 7.4. 1 mM $CaCl_2$ and 1% BSA were added to the standard solution before experiments. Cellular heat production was stimulated with 30, 60, and 90 mM KCl,

for the first, second, and third injections, respectively. We used three cell solutions: the normal Tyrode's solution as described above, the Tyrode's solution with 100 μM isoproterenol, and the Tyrode's solution with 50 mM BDM.

Thermoelectric Sensor

The implementation of our nanocalorimeter is also described in detail in reference 35. It contains a 20-junction thermopile with a Seebeck coefficient of 24 μV/K per junction. The sensor has a 0.5 mm deep well, at the bottom of which are the silicon membrane and thermoelectric junctions. We modified this well into our reaction chamber by adding a double layer cover and using paraffin oil to seal the space between the cover and the sensor (**Figure 11**). In experiments, cell solution was injected onto the center of the membrane where the sensing junctions are located. The cells were then thermally coupled with the sensing junctions, while the reference junctions, located on the edge of the membrane, were closely coupled with the aluminum heat sink.

The voltage generated by the S25 sensor was amplified using a custom low-noise amplifier with 100K gain. The signal was then collected and recorded by the computer's PCI-6024E data acquisition board (National Instruments). A LabView interface is used to display the readings and control the parameters of the recording, such as the sampling rate or range of reading. By using the low noise instrumentation amplifier and a chopper-stabilized operational amplifier in our circuit, we were able to limit the noise to a total level at 20 nV/√Hz. The noise measurement of voltage output is shown in **Figure 13**. A cutoff frequency of 10 Hz provided an

accurate noise voltage density of our calorimetric system at 1 Hz; however, in the experiments we report here, we used a 1 Hz low pass filter instead to lower further the total noise of the calorimetric system. This is appropriate as the time scale of the biological signal we are measuring is on the order of seconds, as demonstrated in our optical measurements of single cardiomyocytes. Such a calorimetric system gives us a power resolution of 22 nW, as described elsewhere.[35]

Experimental Setup

The general experimental setup includes an integrated system for thermal shielding, evaporation prevention, and nanoliter sample delivery (**Figure 26**). The measurement methods are derived from those described previously.[35] In brief, a double-layer thermal shield blocks the thermal noise from the surrounding environment. The inner shield is the cover on the S25 sensor and is composed of a piece of cover glass with a thin Mylar sheet attached to it. Two holes in this inner shield allow the pipette tip to move in and out freely for injections. Paraffin oil was applied to the double holes and between the double layer cover and the sensor's top to seal the reaction chamber and stop evaporation. The 100 μm hole on the Mylar sheet is small enough for surface tension to hold the oil without leaking into the reaction chamber, while the cover glass serves as an infrared signal blocker.

Injection of Cells and KCl

Injections were made by a Picospritzer system (Parker Hannifin) and glass pipettes pulled from 2 mm OD capillaries. The highly automated Picospritzer is able

to generate pressure pulses as short as 3 ms. At constant pressure, the injection volume is highly linear with the duration of the pressure pulse.[36] Micropipettes with 40-60 μm tip openings were used to allow the cardiomyocytes (usually 10 μm X 100 μm) to be delivered freely into the reaction chamber. The delivery volume is precisely controlled at 50 nL by calibrating the micropipette with cell solutions before the actual injection. With a highly concentrated cell solution, this volume will usually yield 10-30 healthy cells, depending on their viability. Subsequent injections of KCl solutions were made by micropipettes with smaller openings, usually 2-5 μm at the tip, which are calibrated for injection of 300 mM KCl solution before the experiment. All injections were performed at 30 PSI, and we varied injection volumes by changing the pulse duration. This protocol guaranteed a precise control over the injection volume due to the high linearity of the injection volume versus the pulse duration at fixed pressure. During the experiment, 4.7, 6.8 and 8.8 nL of 300 mM KCl solutions were injected into the base cell solution for the first, second and third injections, respectively. The three injections elevated the cell solution's K^+ concentration to 30, 60, and 90 mM, respectively.

The pipette's position was controlled by a micromanipulator (Eppendorf Model 5171). We programmed automated control that allowed the pipette to travel between predetermined positions by pushing a single button. **Figure 25** demonstrates the delivery process of a 20 nL sample. During the experiment, the pipette for KCl solution injection was set to travel between a resting position and a position reaching into the cell solution. When injection was necessary, the pipette reached into the cell

solution to deliver the KCl and was retracted once the injection was finished, preventing any loss of sample due to capillary effect.

Cell Counting

For a 50 nL cell solution, the actual healthy cell numbers varied depending on cell viability and concentration. For each of our experiments, we estimated the number of healthy cells delivered by each injection by injecting ten droplets of cell solution onto a glass slide using the same injection method as in the actual experiment and then dying those ten droplets with Trypan Blue so we could determine how many cells were viable. We took the average number of viable cells in those ten droplets and use it as the estimated cell number in that experiment.

Results

Cardiomyocytes Stimulated by KCl

Using the method described above, we injected KCl solution into the cell solution on top of the sensor three times to elevate the K^+ concentration to 30 mM, 60 mM, and 90 mM, respectively. We conducted experiments with cells in three different types of media: normal Tyrode's solution; Tyrode's solution with 100 μM isoproterenol; and Tyrode's solution with 50 mM 2,3-BDM. In addition, we conducted control experiments using just Tyrode's solution without the cells. The typical results of all four types of experiments are shown in **Figure 35**.

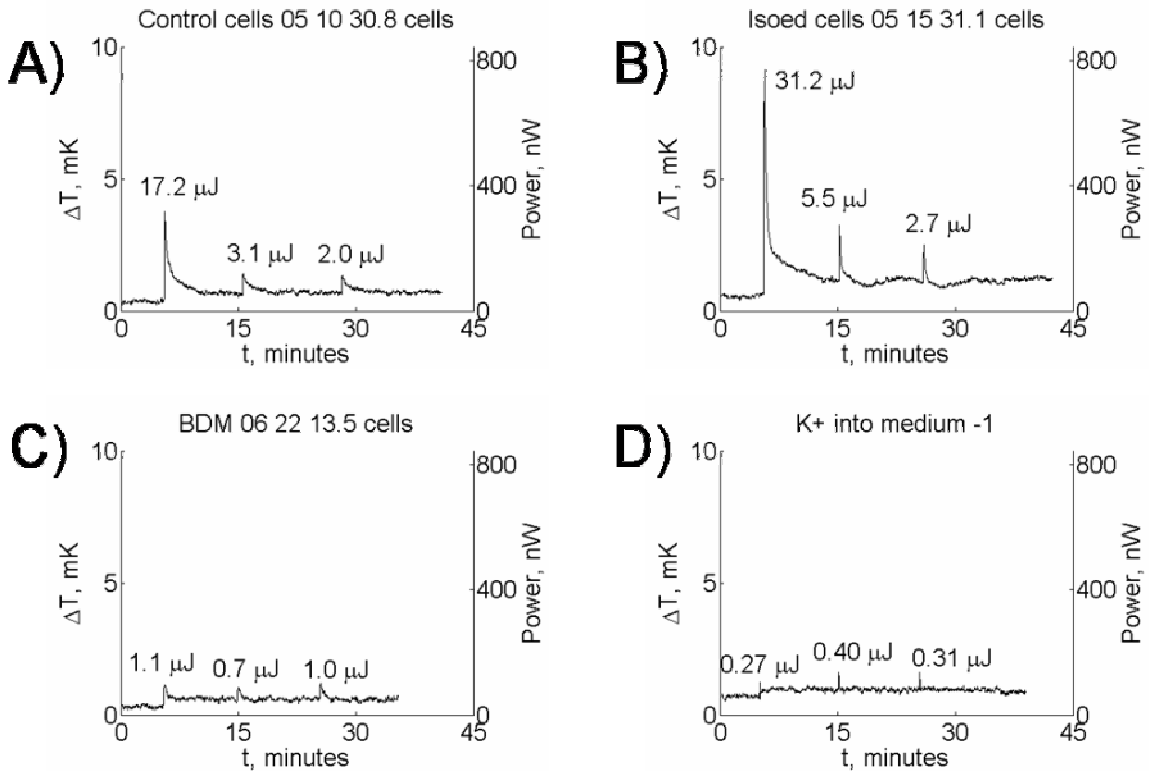

Figure 35. Thermal data recorded from cardiomyocytes. 300 mM K^+ droplets were injected three times at intervals of 10 minutes to raise the medium K^+ concentration to 30, 60, and 90 mM, respectively. Approximate heat productions following each injection are listed on the graph. A) Thermal response from myocytes with normal Tyrode's medium. B) Thermal response from myocytes with 100 μM isoproterenol in the Tyrode's medium. C) Thermal response from myocytes with 50 mM 2,4-BDM added to the medium. D) Thermal response from plain medium with no cells.

Following each injection of KCl, a certain amount of heat production was observed for each experiment. We calculated this heat production by integrating the power versus time curve for 10 minutes (which is the time between two injections) immediately after each injection. The magnitude of the associated heat generation is marked on the figures. Cells in normal Tyrode's solution responded vigorously to the first KCl injection, showing a 100-300 nW (~10 nW per cell) increase in power, while much less energy was produced for subsequent injections. The cells with

isoproterenol in the medium responded with even greater energy production than the cells in normal medium, showing a 200-600 nW (~20 nW per cell) increase in power following the first injection of KCl. With 2,3-BDM in the media, the energy production in response to KCl stimulation was very low (almost none), which we believe is due to the uncoupling of their electrical activity and mechanical contraction. The control experiment for medium without cells showed the minimal heat production that largely comes from the dilution of KCl solution.

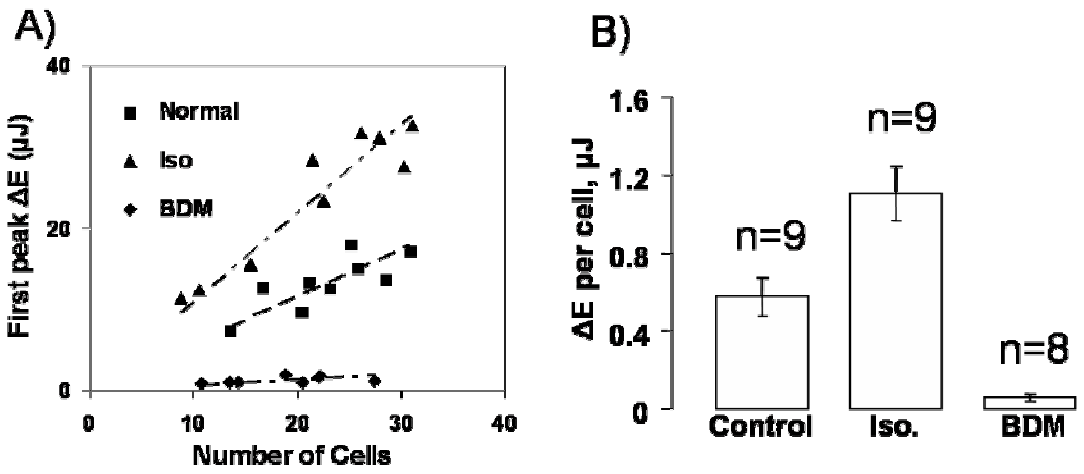

Figure 36. Heat production of cells under 30mM $[K^+]_e$ A) Heat production (μJ) following the first injection versus myocyte numbers for three types of experiments: myocytes exposed to 100 μM isoproterenol (triangles), myocytes in normal Tyrode's medium (squares), and myocytes exposed to 50 mM 2,3-BDM (diamond). B) Comparison of heat production per cell for three types of cell experiments.

Although our cell solution is 50 nL for all experiments, the actual healthy cell numbers could vary from 10-30 depending on viability and concentration. **Figure 36A** shows the heat production following the first injection for three types of cell experiments versus the estimated healthy cell number in individual experiments. The

heat generations following first injections were further processed to determine the cellular heat production for all three types of experiments, shown in **Figure 36B**. Normal cells produced 0.58 µJ of heat during the 10-minute period (with most of the heat actually generated in the first couple of minutes) following the first injection of KCl, while cells with isoproterenol produced 1.11 µJ and cells with 2,3-BDM produced 0.06 µJ.

Physiological Measurements on Single Cells

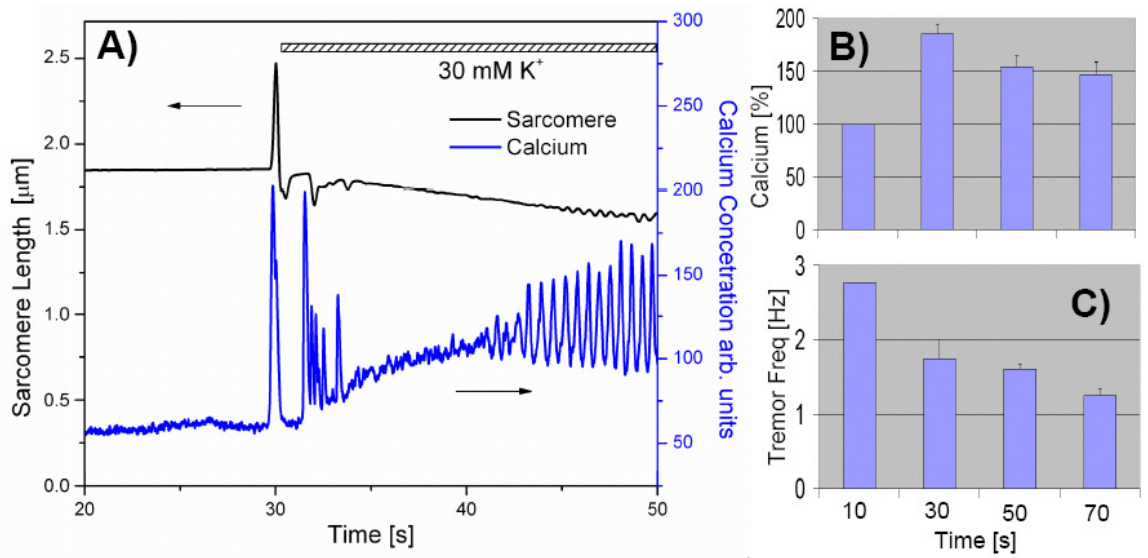

Figure 37. Data from optical measurements of $[Ca^{2+}]_i$ and sarcomere length for single cardiomyocytes under the influence of high $[K^+]_e$. A) A typical time trace that shows both variables before and after an increase of $[K^+]_e$ from 3 to 30 mM. B) The average calcium level versus time as a percentage of the calcium signal before the addition of potassium. C) The frequency of the myocyte tremor versus time.

We made optical measurements on single cardiomyocytes to record the intracellular level of calcium and the change in sacromere length (**Figure 37A**) when

we increased extracellular potassium concentration from 5 mM (the Tyrode's solution's potassium concentration) to 30 mM, which is the potassium concentration after the first injection in our thermal measurements. The intracellular calcium level was observed to increase by almost 100% after the increase of extracellular potassium level, and it slowly decreased and fluctuated at about 150% of the original level when the extracellular potassium concentration was normal (**Figure 37B**). The sacromere length was seen to decrease and oscillate after the increase of extracellular potassium level, which indicated a tremoring of the cardiomyocyte. However, the tremor frequency gradually decreased over time as it went from 2.8 Hz at 10 seconds after the increase of potassium concentration to 1.2 Hz at 70 seconds (**Figure 37C**).

The above results are consistent with our thermal measurements, where we saw a steep rise in power generation right after the increase of extracellular potassium concentration, and the gradual decline of the power back to somewhat above resting level in the time frame of minutes. This power generation is obviously related to the mechanical activity of the myocyte, though the cell may undergo localized tremors instead of full contraction. The increased extracellular potassium level triggered the release of calcium from the sarcoplasmic reticulum to the intracellular space. The local calcium waves then formed an oscillation of intracellular concentration of calcium, which caused the localized contracting of the myocyte, or the tremoring.

Conclusion and Discussion

Our experiments on cardiomyocytes have demonstrated a quantitative way to measure cellular heat production with nW sensitivity. Our nanocalorimeter was implemented in a microfabricated system with test assays using nanoliter volume samples. The different thermal responses of the cardiomyocytes in normal conditions and when various drugs are present showed a 10-20 nW increase in power per cell due to the cells' mechanical actions.

Our understanding of the thermal signals is also confirmed in our physiological measurements on single myocytes. Our optical measurements on single cardiomyocytes have shown a connection between the increased heat production and the tremoring of the cell and intracellular calcium level. We showed that the increased heat production may largely come from the mechanical activity of the myocytes. We found that combined sarcomere length measurements and cytosolic [Ca^{2+}] measurements during the exposure of single cardiac myocytes to a potassium concentration of 30 mM exhibit a rise in cystolic Ca^{2+} concentration accompanied by a reduction of the sarcomere length. Once a cystolic [Ca^{2+}] threshold has been reached, spontaneous slow Ca^{2+} waves and associated contractions occur, initially at a frequency of approximately 3 Hz. The frequency drops to about 1 Hz over the time course of 1 min. Patch clamp measurements recordings (not shown) indicate that the membrane potential depolarizes by 4.6 ± 1.6 mV during the exposure to 30 mM of K^{+}. If the cell is exposed to 50 mM BDM during the 30 mM of potassium exposure we did not find a rise in cytosolic [Ca^{2+}] levels and no spontaneous Ca^{2+} waves. Based on these measurements, we

hypothesize that the exposure to 30 mM of potassium leads to an influx of Na^+ that depolarizes the membrane, which in turns activates the NaCa exchanger, resulting in an influx of Ca^{2+}. The influx of Ca^{2+} is sequestered in the SR, leading to a Ca^{2+} overload and spontaneous local releases, which in turn trigger the observed slow Ca^{2+} waves. The increased heat generation in our calorimetric measurements can therefore be attributed to Ca^{2+} overload-induced energy consumption associated mainly with the contractile machinery and the SERCA. This in turn suggests the value of thermal measurements for separation of Ca^{2+} dynamics from other metabolic effects.

This thermal measurement, using a thin-membrane thermopile sensor of ultra-high sensitivity and with extremely low volume, has shown the potential for massively parallel measurements using integrated devices manufactured on a silicon chip. This instrumentation has clear potential for high-throughput drug screening or biological assays using high-sensitivity quantitative metabolic thermal measurements.

Acknowledgements

This research has been supported in part by NIH grant U01AI061223 and the Vanderbilt Institute for Integrative Biosystems Research and Education. We are indebted to Allison Price for her editorial assistance with this manuscript.

References for Chapter VI

1. Chowdhry, BZ, Beezer, AE, Greenhow, EJ, Analysis of drugs by microcalorimetry : Isothermal power-conduction calorimetry and thermometric titrimetry Talanta 1983, 30, 209-243

2. Hill, AV, The absolute efficiency of the contraction of an isolated muscle, J. Physiol. 1913, 46, 435-469

3. Hill, AV, The effect of veratrine on the heat production of ,medullated nerve, Proc. Roy. Soc. B 1933, 113, 345-356

4. Feng, TP, Hill, AV, The Relation between initial and recovery heat production in frog's nerve, Proc. Ro. Soc. B 1933, 113, 357-365

5. Abbot, BC, Hill, AV, Howarth, JV, The positive and negative heat production associated with a nerve impulse, Proc. Roy. Soc. B 1958, 148, 149-187

6. Paulik, MA, Buckholz, RG, Lancaster, ME, Dallas, WS, Hull-Ryde, FA, Weiel, JE, Lenhard, JM, Development of infrared imaging to measure thermogenesis in cell culture: thermogenic effects of uncoupling protein-2, troglitazone, and beta-adrenoceptor agonists, Pharm, Res 1998, 15, 944-949

7. Weppen, P, Ebens, J, Muller, BG, and Shuller, D, On-line estimation of biological oxygen demand using direct calorimetry on surface attached microbial cultures, Thermochimica Acta, 1991, 193, 135-143

8. Schon, A, and Wadso, I, Microcalorimetric measurements on tissue cells attached to microcarriers in stirred suspension, Journal of biochemical and biophysical methods, 1986,13, 135-143

9. Backman, P, Kimura, T, Schon, A, and Wadso, I, Effects of pH-variations on the kinetics of growth and energy metabolism in cultured T-lymphoma cells: a microcalorimetric study, Journal of cellular physiology, 1992, 150, 99-103

10. Gnaiger, E, Kemp, RB, Anaerobic metabolism in aerobic mammalian cells: information from the ratio of calorimetric heat flux and respirometric oxygen flux, Biochimica et biophysica acta. 1990, 1016, 328-332

11. Gebreselassie, D, Schon, A, Energy metabolism of non-transformed and benzypyrene-transformed 3T3 cells: a microcalorimetric study, Biochimica et biophysica acta, 1993, 1143, 211-214

12. Takahashi, K, Application of calorimetric methods to cellular processes: with special references to quantitative evaluation of drug action on living cells, Thermochimica Acta, 1990, 163, 71-80

13. Patel, M, Thermochimica Acta, Calorimetric screening test for dermatologically active drugs on human skin fibroblast-cultures, 1981, 49, 123-129

14. Nittinger, J , Furst, P, Effects of the cytostatic drug 1-(2-hydroxyethyl)-3-(2-chloroethyl)-3-nrtroso-urea (HECNU) on heat production and Intermediary metabolism of diploid hu, 1991, Thermochimica Acta, 187, 41-48

15. Nassberger, L, Jensen, E, Monti, M, and Floren, CH, Microcalorimetric investigation of metabolism in rat hepatocytes cultured on microplates and in cell suspensions, Biochimica et Biophysica Acta, 1986, 882, 353-358

16. Smith, CG, Solandt, DY, The relation of contracture to the increment in the resting heat production of muscle under the influence of potassium, J. of Physio., 1938, (1238) 93, 305-311

17. Hill, AV, Howarth, JV, The effect of potassium on the resting metabolism of the frog's sartorius, Proceedings of the Royal Society of London, Series B, Biological Sciences, 1957, Vol. 147, No. 926, 21-43

18. Whalen, WJ, Weddle, O, Effect of large variations in external potassium on the oxygen consumption of rat heart strips, 1962, Nature, Vol. 196, 274-275

19. Chinet, A, Decrouy, A, Even, PC, Ca(2+)-dependent heat production under basal and near-basal conditions in the mouse soleus muscle, 1992, J. of Physiol., 455, 663-678

20. Gibbs, CL, Chapman, JB, Cardiac heat production, Ann. Rev. Physiol. 1979, 41, 507-519

21. Hornos, JEP, Marquez, MT, Bonazzola, P, Influence of extracellular potassium on energetics of resting heart muscle, Am. J. Physiol.: Heart and circular Physiol., 1992, 262, 4, H1081-1087

22. Marquez, MT, Consolini, A, Bonazzola, P, JEP Hornos, The energetics of the quiescent heart muscle: high potassium cardioplegic solution and the influence of calcium and hypoxia on the rat heart, Acta. Physiol. Scand. 1997, 160, 229-233

23. Hornos, JEP, Parker, JM, Langer, GA, Heat production in isolated heart myocytes: differences among species, Am. J. Physiol.: Heart and circular Physiol., 1990, 258, H880-H886

24. Lai, SL, Guo, JY, Petrova, V, Ramanath, G, Allen, LH, Size-dependent melting properties of small tin particles: nanocalorimetric measurements, Phys. Rev. Lett. 1996, 77, 99-102

25. Denlinger, DW, Abarra, EN. Allen, K, Rooney, PW, Messer, MT, Watson, SK, Hellman, F, Thin film microcalorimeter for heat capacity measurements from 1.5 to 800 K, Rev. Sci. Instrum. 1994, 65,946-959

26. Johannessen, EA, Weaver, JMR, Cobbold, P.H, Cooper, JM, Heat conduction calorimeter for pl-scale single cell measurements, Appl. Phys. Lett. 2002, 80, 2029-2031

27. Johannessen, EA, Weaver, JMR, Cobbold, PH, Cooper, JM, A suspended membrane nanocalorimeter for ultralow volume bioanalysis, IEEE Trans. NanoBiosci. 2002, 1, 29-36

28. Johannessen, EA, Weaver, JMR, Bourova, L, Svoboda, P, Cobbold, PH, Cooper, JM, Micromachined nanocalorimetric sensor for ultra-low-volume cell-based assays, Anal. Chem. 2002, 74, 2190-2197

29. Wadso, I, Goldberg, RN, Standards in isothermal microcalorimetry, Pure Appl. Chem. 2001, 73, 1625-1639.

30. Zhang, Y, Tadigadapa, S, Calorimetric biosensors with integrated microfluidic channels, Biosen. & Bioelectro. 2004, 19, 1733-1743

31. Lerchner, J, Wolf, A, Wolf, G, Recent developments in integrated circuit calorimetry, J. of Therm. Anal. and Calorim. 1999, 57, 241-251

32. Lerchner, J, Wolf, A, Huttl, R, Wolf, G, Direct monitoring of biochemical processes using micro-structured heat power detectors, Chem. Eng. J. 2004, 101, 187-194

33. Baier, V, Fodisch, R, Ihring, A, Kessler, E, Lerchner, J, Wolf, G, Kohler, JM, Nietzsch, M, Krugel, M, Highly sensitive thermopile heat power sensor for micro-fluid calorimetry of biochemical processes, Sens. and Actu. A. 2005, 123, 354-359

34. Maskow, T, Lerchner, J, Peitzsch, M, Harms, H, Wolf, G, Chip calorimetry for the monitoring of whole cell biotransformation, J. of Biotech. 2006, 122, 431-442

35. Xu, J, Reiserer, R, Tellinghuisen, J, Wikswo, JP, Baudenbacher, FJ, Chemical Calibration of a microfabricated nanocalorimeter, Analytical Chemistry, 2007, in preparation

36. McCaman, RE, Mc Kenna, DG, Ono, JK, A pressure system for intracellular and extracellular ejections of picoliter volumes, Brain Research, 1977, 136, 141-147

CHAPTER VII

SUMMARY AND FUTURE WORK

Summary of the Work

We have modified a commercially available infrared sensor into a nanocalorimetric sensor that is suitable for chemical and biological thermal measurements. The nanocalorimeter was calibrated using chemical methods which demonstrated the nanocalorimeter's power sensitivity of 2.91 ± 0.27 V/W. The nanocalorimeter was used for measurements of the metabolic rate of 10-30 isolated cardiomyocytes. Elevated metabolic rates of 100-600 nW were observed when the cardiomyocytes were stimulated with KCl. This increased metabolic rate was confirmed and explained by our physiological experiments done using single cardiomyocytes. In general, we have presented a high-sensitivity nanocalorimeter that was calibrated using chemical methods and that can be used for biological thermal measurements on a small number of cells.

Future Work

Our nanocalorimeter's sensitivity and detection capability were limited because this sensor was not customized for biological measurements. Our evaporation prevention system and sample delivery system were built to accomplish biological measurements. However, these modifications of the sensor were not sufficient to provide enough precision to deliver a single cell and measure the signal

from it. To achieve the goal of measuring the thermal signal from a single cell, we propose here to make a customized thin-film thermopile sensor that has built-in microfluidics for cell and solution delivery. A schematic for such a sensor is shown in **Figure 38**. The built-in microfluidics will greatly enhance the precision of the delivery process and make it possible to deliver a single cell into the chamber. The differential setup could further reduce noise by rejecting the noise from the environment. A customized sensor with this design would be able to have higher sensitivity, a better detection limit, and a more convenient delivery protocol, which can improve the sensor's overall performance in measuring biological thermal signals and thus could better realize the goals of high-throughput screening (HTS) for drug discovery, metabolic screening using living cells, and multianalyte detection and identification of chemical and biological warfare (CBW) agents.

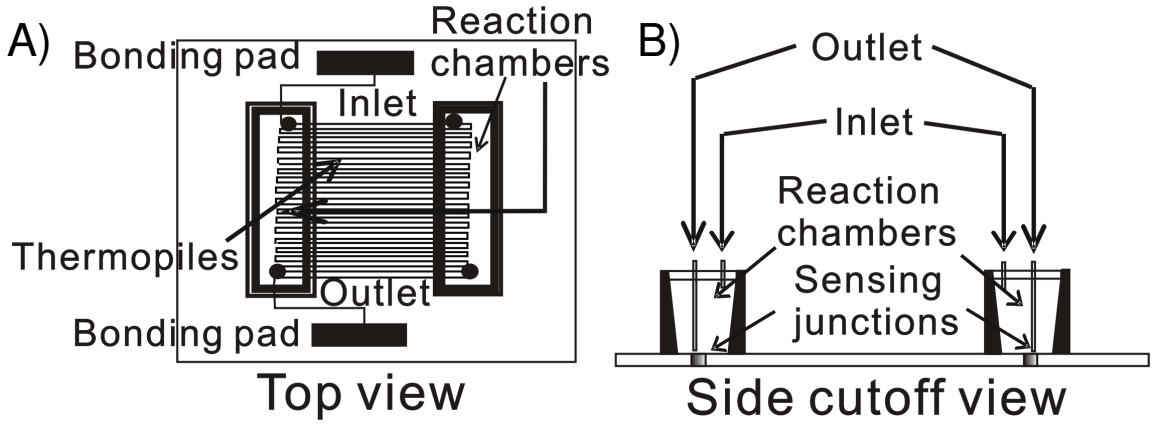

Figure 38 Schematic layout of differential picocalorimeter with integrated dual reaction chambers and microfluidics. Dual reaction chambers built on the two sides of the thermopile junctions enable simultaneous comparison of the cellular and control experiments. A) Top view. B) Side view.

APPENDIX A

S25 SPECIFICATIONS PROVIDED BY DEXTER

S25* TO-18
Silicon Based Thermopile Detector
• +1 734 426 3921
Features: A single-channel silicon-based thermopile that offers the smallest single element active area size at 0.25mm x 0.25mm in a small TO-18 package. Delivers a very fast 12ms time constant in Argon encapsulation gas and even faster with Neon gas at 9ms. Delivers a very low Temperature Coefficient of Responsivity of -0.04%/°C.
Applications: Excellent for non-contact temperature measurement when extremely small spot size is a design requirement.
Benefit: Small active area, fast time constant in a small package with lower output that has a higher cost
Technical Specifications S25 TO-18
Specifications apply at 23°C with KBr Window and Argon encapsulating gas

Parameter	Min	Typical	Max	Symbol	Units	Comments
Active Area size		.25 x .25		AA	mm	Hot junction size, per element.
Element Area		.0625		A	mm^2	
Number of Junctions		20				Per element.
Number of Channels		1				Per detector package.
Output Voltage		23		V_s	µV	DC, H=330µW/cm^2 (3)
Signal-to-Noise Ratio		1,186		SNR	$\sqrt{Hz}$	DC, SNR=V_s/V_n
Responsivity		111.5		$\mathcal{R}$	V/W	DC, $\mathcal{R}$=V_s/HA (2)
Resistance	18	23	28	R	kΩ	Detector element
Temperature Coefficient of $\mathcal{R}$		-.04			%/°C	Best linear fit, 0° to 85°C (1)
Temperature Coefficient of R		.11			%/°C	Best fit, 0° to 85°C (1)
Noise Voltage	17.2	19.4	21.4	V_n	$nV/\sqrt{Hz}$	V_n^2=4kTR
Noise Equivalent Power		.17		NEP	$nW/\sqrt{Hz}$	DC, NEP= V_n HA/V_s (2)
Detectivity		1.44		D*	$10^9 cm\sqrt{Hz}/W$	DC, $D^*=V_s/V_n H\sqrt{A}$ (2)
Time Constant		16		τ	ms	Chopped, -3dB point (1)
Field of View		88°/103°		FOV	Degrees	See Assembly Drawings for FOV Description.
Package Type		TO-18				Standard package hole size: ∅.080"
Operating Temperature	-50		100	T_a	°C	

General Specifications: Flat spectral response from 100nm to > 100µm. Linear signal output from 10^{-6} to 0.1W/cm^2. Maximum incident radiance 0.1W/cm^2, damage threshold ≥ .5W/cm^2

Notes: (1) Parameter is not 100% tested. 90% of all units meet these specifications. (2) A is detector area in cm^2. (3) Test Conditions: 500K Blackbody source; Detector active surface 10cm from 0.6513cm Diameter Blackbody Aperture.

*Protected by U.S. Patent No. 5,059,543 and U.S. Patent No. 5,100,479

APPENDIX B

CRITICAL EQUIPMENT AND MATERIALS CHECKLIST

1. **PCI-6024E DAQ board**
   Manufactured by: National Instruments
   Purchasing website: www.ni.com
   Part number: PCI-6024E
   Accessories to be purchased together: SH6868 shielded cable assembly

2. **BNC 2120 connector box**
   Manufactured by: National Instruments
   Purchasing website: www.ni.com
   Part number: BNC 2120

3. **ICL7652 chopper stabilized OpAmp**
   Manufactured by: Maxim
   Purchasing website: www.maxim-ic.com
   Part number: ICL7652

4. **INA128 instrumentation amplifier**
   Manufactured by: Burr-Brown
   Purchasing website: www.digikey.com
   Part number: INA128

5. **Micromanipulator 5171**
   Manufactured by: Eppendorf

6. **Picospritzer II**
   Manufactured by: Parker Hannifin
   Purchasing info: www.parker.com
   Part number: 052-0302-900 (0-100PSI regulator)
   Accessories to be purchased with:
   Upgrade kit: 052-0100-010-1 (includes second valve box and tubing assemblies to convert a single channel to a two channel)
   Valve box and cable assembly: 051-0009-401-1
   Teflon tubing assemblies: 035-0125-062-72 (1/8 inch OD tubing, 6 feet long, nut & ferrule on both ends)
   Pipette holder: 50-0020-130-1 (Standard straight holder with a .186 inch diameter by 3.5 inch long mounting rod)
   Replacement gaskets for pipette holders: 50-0020-GSK-001

7. **Glass Capillary, 2mm OD, 1.12mm ID**
   Manufactured by: WPI
   Purchasing website: www.wpiinc.com
   Part number: 1B200F-4

8. **Micro Core Drills, 0.023”OD, ¼” long, 3/8”-24 female connector**
   Manufactured by: Technodiamant
   Purchasing website: www.technodiamant.com
   Part number: 0.023”

9. **Dispensing Needles, 0.012”OD, 0.006”ID, 2” long**
   Manufactured by: McMaster-Carr
   Purchasing website: www.mcmaster.com
   Part number: 6710A38

APPENDIX C

CIRCUIT SCHEMATICS AND PCB LAYOUT

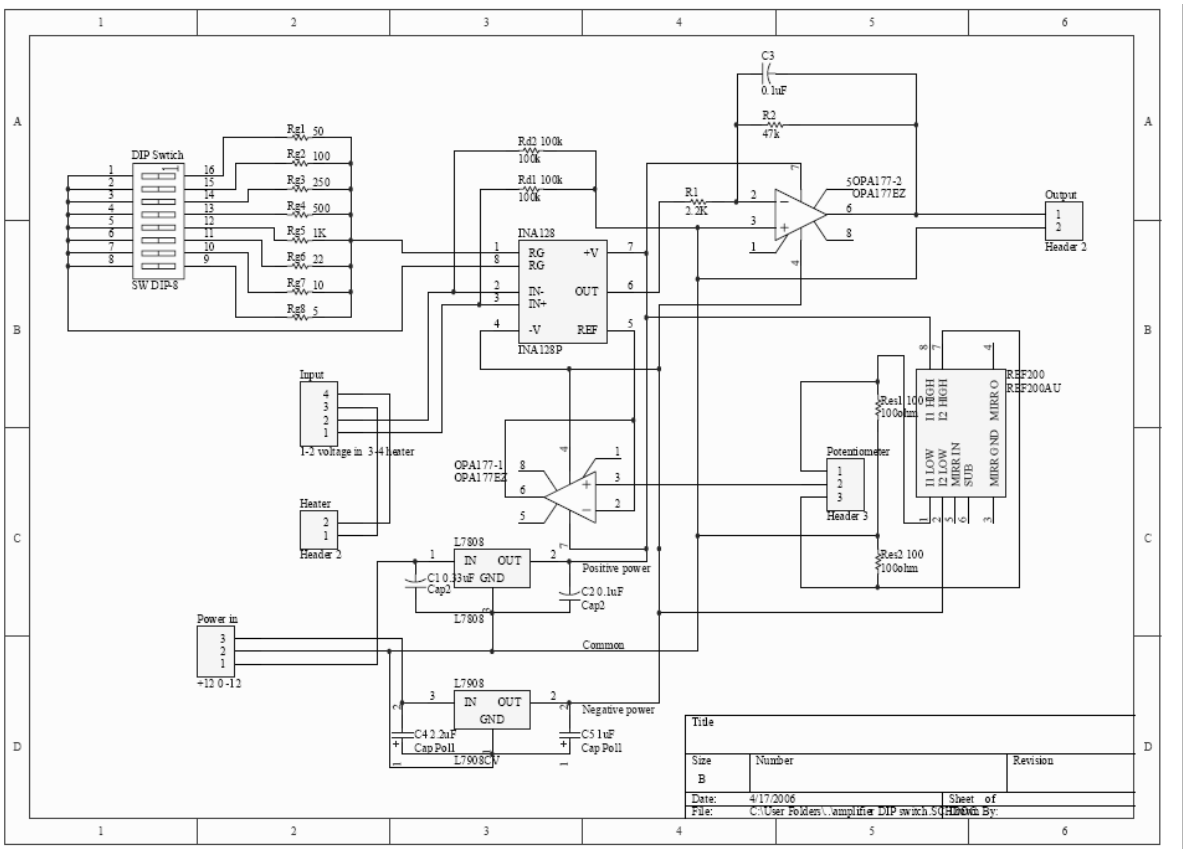

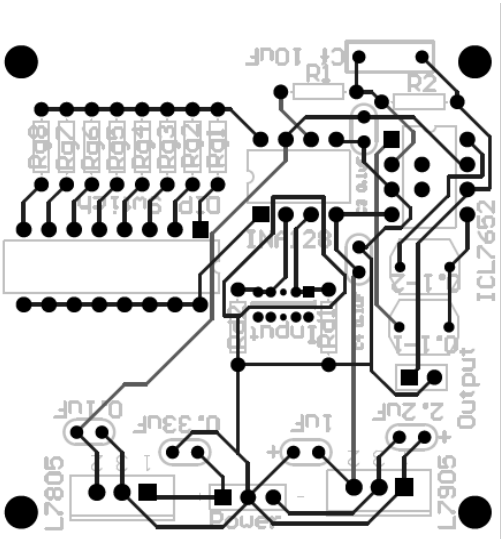

APPENDIX D

MATLAB SCRIPT OF CHEMICAL DIFFUSION MODEL

```
% units: all lengths in um, time in second
% a 50nL droplet has a radius of 288 um, our step lenght is 1um

% initiation of volume and surface area for individual elements
volume = zeros(288,1);
surface = zeros(287,1);

for i=1:288
    volume(i)=2*pi/3*(i^3-(i-1)^3);
    if i<=277
        surface(i)=2*pi*i^2;
    end
end

N=300000; % time step numbers
step=1e-14; % time step in seconds
d=1e13; % diffusion constant in um^2/s
flux = zeros(287,1); % the flux rate at a certain time
concentration = zeros(288,1); % the concentration matrix

%initializing the initial concentration
for i=1:78
    concentration(i) = 1e-17; % unit in mol/um^3, 1e-15 is 1mol/l
end

% begin time loop
for i=1:N
    for j=1:287
        flux(j)=d*(concentration(j)-concentration(j+1));
    end
    for j=1:288
        if j==1
            concentration(j)=concentration(j)+(-flux(j)*surface(j))*step/volume(j);
        elseif j==288
            concentration(j)=concentration(j)+(flux(j-1)*surface(j-1))*step/volume(j);
        else
            concentration(j)=concentration(j)+(flux(j-1)*surface(j-1)-
flux(j)*surface(j))*step/volume(j);
        end
    end
```

```
    if mod(i,1000)==0
        plot(concentration*1e15);axis([0 288 0 1e-2]);
        xlabel('Radius in \mum');ylabel('concentration in mol/l');text(100,0.008,['Time =
        ',num2str(i/100000), 'ns']);
        diffusion_frame(i/1000)=getframe();
        i
    end
end
```

APPENDIX E

MATLAB SCRIPT OF HEAT CONDUCTION MODEL

```
% This program computes the sensor's response for cylindrical symmetry

% Boundary conditions: All elements in contact with heat sink -- 0 k

% The whole sensor is divided into three parts:
% air/oil -- solution above membrane, Membrane, and air below membrane
% which are denoted in the program as 1, 2, 3
% Every element is 10um*10um except for the membrane, which is 1.5um*10um
% Upper part is 50*100, lower part is 100*150
% Membrane is modeled as a homogeneous piece
% Suppose membrane's composition is 0.5um SiO2 with 1um Si3N4
% Thermal characteristics calculated as 1/3 of SiO2 and 2/3 of Si3N4

% ************************************************************************
% The first part create eight matrixs for above/membrane/below
% to represent their vertical/horizontal heat conductivity and capacity
% Those elements next to boundaries don't have these values

Profile_1_con_vertical=ones(50,99);Profile_3_con_vertical=ones(100,149); % on vertical
direction the membrane's conductance is combined into the upper and lower part
Profile_1_con_horizontal=ones(49,99);Profile_2_con=ones(1,84);Profile_3_con_horizontal=one
s(99,149);
Profile_1_cap=ones(49,99);Profile_2_cap=ones(1,84);Profile_3_cap=ones(99,149);
% Definition of the physical properties of different materials
% Heat conductivity in uW/um/K, Heat capacity in uJ/uL/K
Con_air=0.025;Con_membrane=60.4;Con_oil=0.13;Con_water=0.61;
Cap_membrane=2581;Cap_air=1.33;Cap_oil=1579;Cap_water=4184;

% Below solve the "big" radius of the droplet
Contact_Angle=77; % define the contact angle
C_A=Contact_Angle/180*pi; % change contact angle into radian expression
V=0.05 % volume given in unit of microliter
R0=(V/(cos(C_A)^3-3*cos(C_A)+2)*3/pi)^(1/3)*100; % the "big" radius is calculated in units
of 10um
radius=R0*sin(C_A) % showing the radius of droplet in 10um
H0=R0*cos(C_A); % the distance from center of the "big" circle to the membrane is
calculated in units of 10um

% The all-ones profile matrices are then multiplied by angular factors
```

```
% Calculate the conductance in vertical direction for Part 1
for i=1:50
    if i==1
        for j=1:99
            if j^2+(i+H0)^2>R0^2
               Profile_1_con_vertical(i,j)=Con_air*10*pi*(2*j-1)*2; % the unit of thermal
conductance ends up to be uW/K
            else
                Profile_1_con_vertical(i,j)=Con_water*10*pi*(2*j-1)*2; % the thermal
conductance adjacent to membrane is doubled
            end
        end
    else
        for j=1:99
            if j^2+(i+H0)^2>R0^2
                Profile_1_con_vertical(i,j)=Con_air*10*pi*(2*j-1); % the unit of thermal
conductance ends up to be uW/K
            else
                Profile_1_con_vertical(i,j)=Con_water*10*pi*(2*j-1);
            end
        end
    end
end

% Calculate the conductance in horizontal direction for Part 1
for i=1:49
    for j=1:99
       if j^2+(i+H0)^2>R0^2
           Profile_1_con_horizontal(i,j)=Con_air*2*pi*j*10; % unit of thermal conductance
ends up to be uW/K
       else
           Profile_1_con_horizontal(i,j)=Con_water*2*pi*j*10;
       end
    end
end

% Calculate the heat capacity for Part 1
for i=1:49
    for j=1:99
        if j^2+(i+H0)^2>R0^2
            Profile_1_cap(i,j)=Cap_air*1e-3*pi*(2*j-1); % unit of thermal capacity in nJ/k
        else
            Profile_1_cap(i,j)=Cap_water*1e-3*pi*(2*j-1);
        end
    end
end

% Calculate the horizontal (only) conductance for Part 2
for j=1:84
```

```
    Profile_2_con(1,j)=Con_membrane*2*pi*j*1.5; % unit of thermal conductance in uW/K,
thickness of membrane 1.5um is used here
end

% Calculate the heat capacity for Part 2
for j=1:84
    Profile_2_cap(1,j)=Cap_membrane*1.5e-4*pi*(2*j-1); % unit of thermal capacity in nJ/K
end

% Calculate the vertical conductance for Part 3
for j=1:99
    Profile_3_con_vertical(1,j)=Con_air*10*pi*(2*j-1)*2; % unit of thermal conductance in
uW/K
    Profile_3_con_vertical(2:100,j)=Con_air*10*pi*(2*j-1); % conductance adjacent to
membrane is doubled
end

% Calculate the horizontal conductance for Part 3
for j=1:149
    Profile_3_con_horizontal(:,j)=Con_air*2*pi*j*10; % unit of thermal conductance in uW/K
end

% Calculate the heat capacity for Part 3
for j=1:149
    Profile_3_cap(:,j)=Cap_air*1e-3*pi*(2*j-1); % unit of thermal capacity in nJ/K
end

% ************************************************************************
% The part below starts calculate the time-dependent temperature change

% Initiate the Temp array to store the temperature data
Temp_1=zeros(50,100,2); % All temperatures are in units of Kelvin
Temp_2=zeros(1,85,2);
Temp_3=zeros(100,150,2);

N=2.5e7; % Total number of steps
dt=2e-4; % Time step in ms
%total time is 5s now

% Create power source in a vector, power will be put on the first layer of
% above the membrane
L=10; % L is the total length over which power is supplied
Power_line=zeros(L,1);
Power_line_intime=zeros(L,1);
%for i=1:L
%    Power_line(i)=0.01*(2*i-1); % unit of power is in uW, the first index denoting the
span of power, the second index denoting the time frame
%end
```

```
%total_power=sum(Power_line(1:L)) % calculation of total power applied on the sensor
frame_number=5e3; % this number tells how many time steps do we make a frame
Response_temp=zeros(N/frame_number,6);% Temp01 stores the temperature of the center of the
sensor, and the temperature at 03,04,08,09,14 elements (these elements' temperature will
be used to calculate the sensor's reposne)
Response=zeros(N/frame_number,1); % this is the overall temperature response of the sensor

figure(1);
plot(0,0,'*'); %plot the starting point
hold on
getframe();



% Time-progressing calculation begins
for k=1:N

    %define Power_line_intime's value
    %if k<=N
    %    Power_line_intime=Power_line;
    %else
    %    Power_line_intime=0;
    %end

    if k==5e6
        Temp_1(10,1,1)=10; %initialization of the droplet temperature (right after
injection/heat production)
    end

    % First Calculate the upper part
    i=1;
    j=1;
    Temp_1(i,j,2)=Temp_1(i,j,1)+((Temp_2(1,j,1)-
Temp_1(i,j,1))*Profile_1_con_vertical(i,j)+(Temp_1(i+1,j,1)-
Temp_1(i,j,1))*Profile_1_con_vertical(i+1,j)+(Temp_1(i,j+1,1)-
Temp_1(i,j,1))*Profile_1_con_horizontal(i,j)+Power_line_intime(1))*dt/Profile_1_cap(i,j);
    for j=2:L
        Temp_1(i,j,2)=Temp_1(i,j,1)+((Temp_2(1,j,1)-
Temp_1(i,j,1))*Profile_1_con_vertical(i,j)+(Temp_1(i+1,j,1)-
Temp_1(i,j,1))*Profile_1_con_vertical(i+1,j)+(Temp_1(i,j-1,1)-
Temp_1(i,j,1))*Profile_1_con_horizontal(i,j-1)+(Temp_1(i,j+1,1)-
Temp_1(i,j,1))*Profile_1_con_horizontal(i,j)+Power_line_intime(j))*dt/Profile_1_cap(i,j);
    end
    for j=L+1:85
        Temp_1(i,j,2)=Temp_1(i,j,1)+((Temp_2(1,j,1)-
Temp_1(i,j,1))*Profile_1_con_vertical(i,j)+(Temp_1(i+1,j,1)-
Temp_1(i,j,1))*Profile_1_con_vertical(i+1,j)+(Temp_1(i,j-1,1)-
```

```
Temp_1(i,j,1))*Profile_1_con_horizontal(i,j-1)+(Temp_1(i,j+1,1)-
Temp_1(i,j,1))*Profile_1_con_horizontal(i,j))*dt/Profile_1_cap(i,j);
    end
    j=1;
    for i=2:49
        Temp_1(i,j,2)=Temp_1(i,j,1)+((Temp_1(i-1,j,1)-
Temp_1(i,j,1))*Profile_1_con_vertical(i,j)+(Temp_1(i+1,j,1)-
Temp_1(i,j,1))*Profile_1_con_vertical(i+1,j)+(Temp_1(i,j+1,1)-
Temp_1(i,j,1))*Profile_1_con_horizontal(i,j))*dt/Profile_1_cap(i,j);
    end
    for i=2:49
        for j=2:99
            Temp_1(i,j,2)=Temp_1(i,j,1)+((Temp_1(i-1,j,1)-
Temp_1(i,j,1))*Profile_1_con_vertical(i,j)+(Temp_1(i+1,j,1)-
Temp_1(i,j,1))*Profile_1_con_vertical(i+1,j)+(Temp_1(i,j-1,1)-
Temp_1(i,j,1))*Profile_1_con_horizontal(i,j-1)+(Temp_1(i,j+1,1)-
Temp_1(i,j,1))*Profile_1_con_horizontal(i,j))*dt/Profile_1_cap(i,j);
        end
    end

    % Second Calculate the lower part
    i=1;
    j=1;
    Temp_3(i,j,2)=Temp_3(i,j,1)+((Temp_2(1,j,1)-
Temp_3(i,j,1))*Profile_3_con_vertical(i,j)+(Temp_3(i+1,j,1)-
Temp_3(i,j,1))*Profile_3_con_vertical(i+1,j)+(Temp_3(i,j+1,1)-
Temp_3(i,j,1))*Profile_3_con_horizontal(i,j))*dt/Profile_3_cap(i,j);
    for j=2:85
        Temp_3(i,j,2)=Temp_3(i,j,1)+((Temp_2(1,j,1)-
Temp_3(i,j,1))*Profile_3_con_vertical(i,j)+(Temp_3(i+1,j,1)-
Temp_3(i,j,1))*Profile_3_con_vertical(i+1,j)+(Temp_3(i,j-1,1)-
Temp_3(i,j,1))*Profile_3_con_horizontal(i,j-1)+(Temp_3(i,j+1,1)-
Temp_3(i,j,1))*Profile_3_con_horizontal(i,j))*dt/Profile_3_cap(i,j);
    end
    j=1;
    for i=2:99
        Temp_3(i,j,2)=Temp_3(i,j,1)+((Temp_3(i-1,j,1)-
Temp_3(i,j,1))*Profile_3_con_vertical(i,j)+(Temp_3(i+1,j,1)-
Temp_3(i,j,1))*Profile_3_con_vertical(i+1,j)+(Temp_3(i,j+1,1)-
Temp_3(i,j,1))*Profile_3_con_horizontal(i,j))*dt/Profile_3_cap(i,j);
    end
    for i=2:99
        for j=2:149
            Temp_3(i,j,2)=Temp_3(i,j,1)+((Temp_3(i-1,j,1)-
Temp_3(i,j,1))*Profile_3_con_vertical(i,j)+(Temp_3(i+1,j,1)-
Temp_3(i,j,1))*Profile_3_con_vertical(i+1,j)+(Temp_3(i,j-1,1)-
Temp_3(i,j,1))*Profile_3_con_horizontal(i,j-1)+(Temp_3(i,j+1,1)-
Temp_3(i,j,1))*Profile_3_con_horizontal(i,j))*dt/Profile_3_cap(i,j);
        end
```

```
    end

    % Third Calculate the membrane part
    j=1;
    Temp_2(1,j,2)=Temp_2(1,j,1)+((Temp_1(1,j,1)-
Temp_2(1,j,1))*Profile_1_con_vertical(1,j)+(Temp_3(1,j,1)-
Temp_2(1,j,1))*Profile_3_con_vertical(1,j)+(Temp_2(1,j+1,1)-
Temp_2(1,j,1))*Profile_2_con(1,j))*dt/Profile_2_cap(1,j);
    for j=2:84
        Temp_2(1,j,2)=Temp_2(1,j,1)+((Temp_1(1,j,1)-
Temp_2(1,j,1))*Profile_1_con_vertical(1,j)+(Temp_3(1,j,1)-
Temp_2(1,j,1))*Profile_3_con_vertical(1,j)+(Temp_2(1,j+1,1)-
Temp_2(1,j,1))*Profile_2_con(1,j)+(Temp_2(1,j-1,1)-Temp_2(1,j,1))*Profile_2_con(1,j-
1))*dt/Profile_2_cap(1,j);
    end

    % Finally reset all temperary values to new values
    Temp_1(:,:,1)=Temp_1(:,:,2);
    Temp_2(:,:,1)=Temp_2(:,:,2);
    Temp_3(:,:,1)=Temp_3(:,:,2);

    if mod(k,frame_number)==0

        Response_temp(k/frame_number,1)=Temp_2(1,1,1);
        Response_temp(k/frame_number,2)=Temp_2(1,3,1);
        Response_temp(k/frame_number,3)=Temp_2(1,4,1);
        Response_temp(k/frame_number,4)=Temp_2(1,8,1);
        Response_temp(k/frame_number,5)=Temp_2(1,9,1);
        Response_temp(k/frame_number,6)=Temp_2(1,14,1);
        Response(k/frame_number)=mean(Response_temp(k/frame_number,:));
        plot(k*dt/1e3,Response(k/frame_number)*1000,'*');
        getframe();
        %axis([0 85 0 1e-2]);
        %text(60,7e-3,['Time = ',num2str(k/5000),' ms']);
        %frame(k/frame_number)=getframe();
        hold on;
        k
    end

end
```

REFERENCES

1. Wadso, I, Isothermal Microcalorimetry for the Characterization of Interactions Between Drugs and Biological Materials. Thermochim.Acta, 267, 45-59, 1995

2. Bottcher, H and Furst, P. Direct Microcalorimetry As a Technique in Cell Cultures. Bailliere's Clinical Endocrinology and Metabolism, 11, 739-752, 1997

3. Sturtevant, JM. Biochemical Applications of Differential Scanning Calorimetry, Annu.Rev.Phys.Chem.,38, 463-488, 1987

4. McGlashan, ML, *Chemical Thermodynamics*. Academic Press, London, 1979, Chapter 4.

5. Wadso. I and Goldberg RN, Standards in isothermal microcalorimetry, Pure and Applied Chemistry 73, 1625-1639, 2001 IUPAC

6. Johannessen, EA, Weaver, JM, Cobbold, PH, and Cooper, JM, A Suspended Membrane Nanocalorimeter for Ultralow Volume Bioanalysis, IEEE transactions on Nanoscience, Vol.1, No.1, March, 2002

7. Johannessen, EA, Weaver, JMR, Bourova, L, Svoboda, P, Cobbold, PH, Cooper,JM. Micromachined Nanocalorimetric Sensor for Ultra-Low-Volume Cell-Based Assays. Anal.Chem., 74, 2190-2197, 2002

8. Johannessen, EA, Weaver, JMR, Cobbold, PH, Cooper, JM. Heat Conduction Nanocalorimeter for Pl-Scale Single Cell Measurements. Appl. Phys. Lett., 80, 2029-2031, 2002

9. Chancellor, EB, Wikswo, JP, Baudenbacher, F, Radparvar, M and Osterman, D, Heat conduction calorimeter for massively parallel high throughput measurements with picoliter sample volumes, Applied Physics Letter, 85,12, September 2004

10. Ladbury, JE and Chowdhry, BZ, *Biocalorimetry, applications of calorimetry in the biological sciences,* chapter 1, John Wiley & Sons, West Sussex, England, 1998

11. Sturtevant, JM, *Physical Methods of Organic Chemistry*, Vol. 1, Part V, Weissberger, A and Rossiter, BW (Eds.), pp. 347-425, Wiley, New York, 1971

12. Calvet, E and Prat, H. *Recent Progress in Microcalorimetry*, Pergamon, London 1963

13. Randzio, ST and Suurkuusk, J, *Biological Microcalorimetry*, Beezer, AE (Ed.), pp. 311-341, Academic, London 1980

14. Backman, P, Bastos, M, Hallen, D, Lonnbro, P, Wadso, I, J. Biochem. Biophys. Methods, 28, 85-100, 1994

15. Wiseman, T, Williston, S, Brandts, JF and Lin, LN, Rapid measurement of binding constants and heats of binding using a new titration calorimeter, Anal. Biochem, 179, 131-137,1989

16. Straume, M and Freire, E, Two-dimensional differential scanning calorimetry: Simultaneous resolution of intrinsic protein structural energetics and ligand binding interactions by global linkage analysis, Anal. Biochem, 203, 259-268, 1992

17. Wadso, I, Trends in isothermal calorimetry, Chem. Soc. Rev. 79-86, 1997

18. Willson, RJ, Beezer AE and Mithcell, JC, Determination of thermodynamic and kinetic parameters from isothermal heat conduction calorimetry: application to Long-term-reaction studies, J. Phy. Chem. 99, 7108-7113, 1995

19. Hansen, LD, Calorimetric Measurement of the Kinetics of Slow Reactions Ind. Eng. Chem. Res. 39, 3541-3549, 2000

20. Verhaegen,K, Baert,K, Simaels,J, Van Driessche,W. A High-Throughput Silicon Microphysiometer. Sens. Act.A, 82, 186-190, 2000

21. Lerchner,J, Wolf,A, Wolf,G. Recent Developments in Integrated Circuit Calorimetry. Journal of Thermal Analysis and Calorimetry, 57, 241-251, 1999

22. Caspary,D, Schropfer,M, Lerchner,J, Wolf,G. A High Resolution IC-Calorimeter for the Determination of Heats of Absorption Onto Thin Coatings. Thermochim.Acta, 337, 19-26, 1999

23. Torra,V, Auguet,C, Lerchner,J, Marinelli,P, Tachoire,H. Identification of Micro-Scale Calorimetric Devices. I. Establishing the Experimental Rules for Accurate Measurements. Journal of Thermal Analysis and Calorimetry, 66, 255-264, 2001

24. Lerchner, J, Wolf, A, Huttl, R, and Wolf, G, Direct monitoring of biochemical processes using micro-structured heat power detectors, Chemical Enginnering Journal, 101, 187-194, 2004

25. Baier, V, Fodisch, R, Ihring, A, Kessler, E. Lerchner, J, Wolf, G, Kohler, JM, Nietzsch, M, and Krugel, M, Highly sensitive thermopile heat power sensor for micro-fluid calorimetry of biochemical processes, Sensors and Actuators A, 123-124, 354-359, 2005

26. Maskow, T, Lerchner, J, Peitzsch, M, Harms, H, and Wolf, G, Chip calorimetry for the monitoring of whole cell biotransformation, Journal of biotechnology 122, 431-442, 2006

27. Johannessen, EA, Weaver, JMR, Bourova, L, Svoboda, P, Cobbold, PH, Cooper,JM. Micromachined Nanocalorimetric Sensor for Ultra-Low-Volume Cell-Based Assays. Anal.Chem., 74, 2190-2197, 2002

28. Johannessen, EA, Weaver, JMR, Cobbold, PH, Cooper, JM, Heat Conduction Nanocalorimeter for Pl-Scale Single Cell Measurements. Appl.Phys.Lett., 80, 2029-2031, 2002

29. Johannessen, EA, Weaver, JMR, Cobbold, PH, Cooper, JM, A suspended membrane nanocalorimeter for ultralow volume bioassays, IEEE transactions on Nanobiosciences, 1, 29-36, March 2002

30. Spink, C and Wadso, I, in Click, D (ED.), Methods of Biochemical Analysis, 23, 1, 1976

31. Schon, A. and Wadso, I, Microcalorimetric measurements on tissue cells attached to microcarriers in stirred suspension, Journal of biochemical and biophysical methods, 13, 135-143, 1986

32. Backman, P, Kimura, T, Schon, A, and Wadso, I, Effects of pH-variations on the kinetics of growth and energy metabolis in cultured T-Lymphomna cells: a microcalorimetric study, Journal of cellular physiology, 150, 99-103, 1992

33. Backman, P and Wadso, I, Cell growth experiments using a microcalorimetric vessel equipped with oxygen and pH electrodes, Journal of biochemical and biophysical methods, 23, 283-293, 1991

34. Gnaiger, E and Kemp, RB, Anaerobic metabolism in aerobic mammalian cells: information from the ratio of calorimetric heat flux and respirometric oxygen flux, Biochimica et biophysica acta. 1016, 328-332, 1990

35. Gebreselassie, D and Schon, A, Energy metabolism of non-transformed and benzpyrene-transformed 3T3 cells: a microcalorimetric study, Biochimica et biophysica acta, 1143, 211-214, 1993

36. Nordmark, MG, Laynez, J, Schon, A, Suurkuusk, J, and Wadso, I, Design and testing of a new microcalorimetric vessel for use with living cellular systems and in titration experiments, Journal of biochemical and biophysical methods, 10, 187-202, 1984

37. Weppen, P, Ebens, J, Muller, BG, and Shuller, D, On-line estimation of biological oxygen demand using direct calorimetry on surface attached microbial cultures, Thermochimica Acta, 193, 135-143, 1991

38. Buckton, G, Russel, SJ and Beezer, AE, Pharmaceutical calorimetry: a selective review, Thermochimica Acta, 193, 195-214, 1991

39. Takahashi, K, Application of calorimetric methods to cellular processes: with special references to quantitative evaluation of drug action on living cells, Thermochimica Acta, 163, 71-80, 1990

40. Patel, M, Calorimetric screening test for dermatologically active drugs on human skin fibroblast-cultures, Thermochimica Acta, 49, 123-129, 1981

41. Nittinger, J and Furst, P, Effects of the cytostatic drug 1-(2-hydroxyethyl)-3-(2-chloroethyl)-3-nitroso-urea (HECNU) on heat production and intermediary metabolism of diploid human fibroblasts IMR 90, Thermochimica Acta, 187, 41-48, 1991

42. Schaarschmidt, B and Reichert, U, Heat evolution by human skin fibroblasts in monolayer culture, Experimental Cell research 131, 480-483, 1981

43. Nassberger, L, Jensen, E, Monti, M, and Floren, CH, Microcalorimetric investigation of metabolism in rat hepatocytes cultured on microplates and in cell suspensions, biochimica et biophysica acta, 882, 353-358, 1986

44. Liu, Z, Cui, C, and Zhang, Y, Studies of the effect on tumor and normal cells in vitro with bioactive materials isolated from algae by a microcalorimetric method, Journal of biochemical and biophysical methods, 23, 163-167, 1991

45. Nicholls, DG and Locke, RM, Thermogenic mechanisms in brown fat, Physiological Reviews, 64, 1, 1984

46. Lonnbro, P, and Wadso, I, Journal of biochemical and biophysical methods, 22, 331, 1991

47. Bryzek, J, Petersen, K, Mcculley, W. Micromachines on the March. IEEE spectrum, 31,20-31,1994

48. Osterman, DP, Patt, R, Hunt, R, Lane, K, Gaalema,S. Uncooled micromachined thermopile arrays and read-out circuits, Infrared Technology and Applications, SPIE, 376-387, 1999

49. Motchenbacher, CD and Fitchen FC, *Low-Noise Electronic Design*, John Wiley & Sons, New York 1973

50. Princeton applied research corporation, How to use noise figure, 1969

51. Letzter, Sand Webster, N, Noise in amplifiers, IEEE spectrum, 67-75, August 1970

52. Carter, B The PCB is a component of op amp design, 42-47, Analog Applications Journal, August 2000

53. McCaman RE, McKenna, GD and Ono, JK, A pressure system for intracellular and extracellular ejections of picoliter volumes, Brain Res., 1977, 136, 141-147

54. Palmer, MR, Wuerthele, SM and Hoffer, BJ, Physical and physiological characteristics of micropressure injection of drugs from multibarreled pipettes, Neuropharm. 1980, 19, 931-938

55. Parsons, R, Handbook of electrochemical constants, Butterworths Scientific Publications, London, 1959

56. Phipps, DW, Ishida, KP, Leddy, M, Safarik, J, Rodrigues, G, Knoell, T, Bold, R, Contact angle measurement, http://www.micromemanalytical.com/CAngle/ConAngl.htm#Fig%204, 2007

57. Skloudowska, A, Wozniak, M, Matlakowska, R, The method of contact angle measurements and estimation of work of adhesion in bioleaching of metals, Biol. Proc. Online 1(3), 114-121, April 1999

58. *CRC Handbook of Physics and Chemistry,* CRC press, Boca Raton, FL, 2004

59. Godgrey, D, Herguth, WR, Physical and chemical properties of mineral oils that affect lubrication, Herguth Laboratories, Inc. 1995